MODELING AND SIMULATION OF BRITTLE ARMORS UNDER IMPACT AND BLAST EFFECTS

By

Nikolas Andrew Nordendale

Dissertation

Submitted to the Faculty of the

Graduate School of Vanderbilt University

in partial fulfillment of the requirements

for the degree of

DOCTOR OF PHILOSOPHY

in

Civil Engineering

December, 2013

Nashville, Tennessee

Approved:

Professor Prodyot K. Basu

Professor Sankaran Mahadevan

Professor Caglar Oskay

Professor James Wittig

To my Mother and Father,

Whose unshakable love and confidence kept me going,

You made this possible.

ACKNOWLEDGEMENTS

This work would not have been possible without the financial support of the Engineering Research and Development Center of the U.S. Army Corps of Engineers and the Vanderbilt University Provost Graduate Fellowship. I am especially indebted to William F. Heard who has been with me since the beginning of graduate school, through the courses, long meetings, conferences, and has provided me with the experimental data needed to complete my research.

Each of the members of my Dissertation Committee has provided me with extensive personal and professional guidance and taught me a great deal about scientific research. I would especially like to thank Dr. P.K. Basu, the chairman of my committee. As my teacher, adviser, and mentor, he has taught me more than I could ever hope to credit him for here. He has shown me, through his example, what a good scientist and researcher should be.

I would also like to express my gratitude to the undergraduate students who assisted me during their summers and made incredible contributions to my research.

I would like to thank my friends for supporting me during this program. To my classmates who turned into such amazing friends, Ghina, Lesa, Paul, and Catie, your help in classwork, programming, and other random research conversations were instrumental in my work. To my best friend in the world, Kaylen, you’ve been with me from the beginning and I couldn’t have made it this far without your friendship and love.

Nobody has been more important to me in the pursuit of my doctorate than the members of my family. My siblings, grandparents, aunts and uncles, cousins, you have all been amazing. Above all, I would like to thank my parents, Kelly and Keli, whose love and guidance are always with me in whatever I pursue. You have taught me the most important lesson in life: how to be a good person.

LIST OF TABLES

Table Page

LIST OF FIGURES

TABLE OF CONTENTS

Page

Chapter 1

Introduction

1.1 Motivation

In recent years, the U.S. Army has embarked upon developing a rapidly deployable protective armor system made of a high-strength, cementitious material for the soldiers combating asymmetric terrorist threats. Recent shifts towards combating nontraditional threats and tactics from terrorists have presented new challenges to providing protection for U.S. troops in foreign theaters of operation. In typical operations, a significant threat to the U.S. warfighter was direct and indirect fire weapons such as mortars, artillery, shoulder-fired rockets, suicide bombings, and small-arms fire. Physical protection for the warfighter was traditionally provided by hardened structures, large soil-filled revetment walls, or concrete barriers. These protective measurements offered protection, simply put, through mass. Figure 1.1 shows some examples of these types of protective structures.

Although this has been a proven protective solution, the typical approach is often not practical or desirable, as it requires significant time, manpower, equipment, and other valuable resources. Furthermore, constructing massive concrete structures with limited, or at best, poor quality, in situ construction materials often results in having to transport better quality raw material from neighboring countries or from the U.S. This presents many logistical challenges and is often not cost effective. Accessibility of required heavy construction equipment in remote terrains is questionable. In addition, U.S. troops operating in close-engagement conditions such as contingency outposts and outside-the-wire construction or repair operations are often left vulnerable to terrorist attacks. In this typical scenario, the warfighter may occupy an area for very short periods of time—typically hours or days, rather than months or years—until the task is completed. Hardened structures and massive walls or barriers are not practical for such conditions [15].

Given this scenario, recent Army research programs are focused on developing ultra-high strength concrete (UHSC) mixtures and lightweight, rapidly deployable protective structures. A goal of these research programs is to develop protective options that depend more on system ductility or enhanced material properties to provide protection from blast and weapon fragmentation, rather than mass alone [15]. Examples of such research programs include the “Modular Protective System for Future Force Assets” (MPS) and “Defeat of Emerging Adaptive Threats” (DEFEAT). For the MPS program, a primary objective was to develop a lightweight structure that could be rapidly constructed and positioned without heavy equipment or significant manpower while providing the required level of protection from specific threats [34]. The lightweight structure was clad with multiple layers of thin UHSC panels that were prefabricated at a U.S. manufacturing facility and shipped to the war site. A typical MPS structure after construction and during a small mortar test can be seen in Figure 1.2. The panels were developed to provide protection from blast and weapon fragmentation at a considerably reduced thickness than that required by a more traditional concrete mixture, thus reducing mass. Full-scale field experiments validated the prototype and showed initial success of the approach. To build on this success, further development of a similar UHSC mixture has been initiated at the Geotechnical and Structures Laboratory (GSL) of the DOD’s Engineering Research and Development Center (ERDC) at Vicksburg, Mississippi. As part of this effort, a thorough multi-scale material property characterization effort to better understand and improve similar cementitious composites is being undertaken [15].

The armor panels used in the MPS system is required to be lightweight, inexpensive to manufacture, easily and rapidly deployable, and capable of providing effective protection against bomb blast, shock, and high-velocity impact. The nature of high-velocity impact is a problem of high complexity. The applications for such studies, particularly concerning brittle cementitious materials, have been researched extensively by both civil and military organizations. In the experimental research effort being currently undertaken at the ERDC as part of the effort, requires many concrete panels to be cast and tested against numerous projectile types and sizes at various impact velocities, as well as shock tube tests to simulate air blast. This is time consuming, expensive, and often will leave many warfare situations unchecked. To be able to predict the behavior of the myriad possibilities, modeling and simulation by some discrete numerical method like finite element method (FEM) and smoothed particle hydrodynamics (SPH) may be the sensible alternative provided the material model can be properly defined and associated parameters can be accurately characterized.

Figure 1.1 Soil-filled barrier construction (left) and precast concrete barrier construction (right)

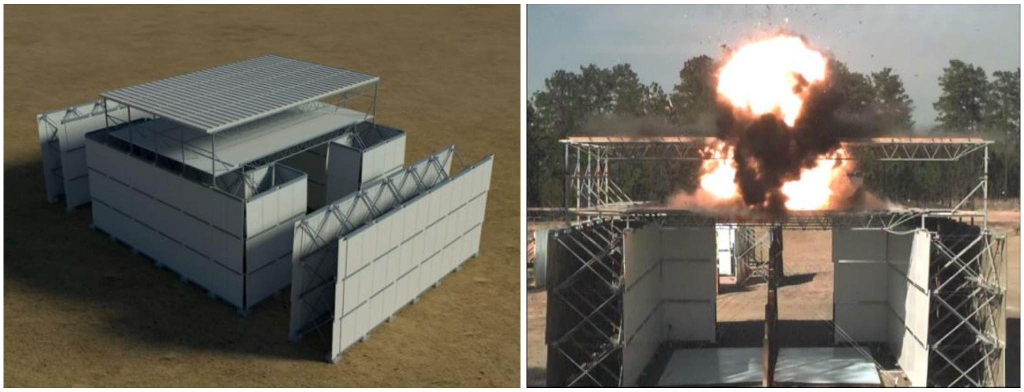

Figure 1.2 Rendering of a typical MPS system (left) and small mortar test of MPS system (right)

The primary purpose of this research is to ultimately simulate high-rate ballistic impact events of small, deformable projectiles on thin, UHSC panel structures as well as uniform blast loads on similar panel structures reinforced with randomly distributed and oriented reinforcing short fibers. This must be accomplished with a high degree of accuracy when compared to ballistic experiments. To do this, the physics of these scenarios are described in greater detail in Chapter 2. Here, dynamic loads are characterized and their effects on cementitious materials are described. A literature survey of the most prominent material models used to simulate concrete under high-rate, high-strain, high-pressure loading is described in Chapter 3. A superior model for the applications in this work is described in Chapter 4 along with implementation details. The parametric identification of the material model constants for two high-strength cementitious materials is given in Chapter 5. An introduction to the modeling and simulation strategies used in this work is presented in Chapter 6, where traditional finite element analysis is compared to the smoothed particle hydrodynamics method. Chapter 7 gives a number of ballistic impact applications of the aforementioned model and material parameters with validating experimental results. Here, the two modeling methods are compared against each other, merits and demerits are identified, and ultimately compared against the experimental results. Finally Chapter 8 introduces the complexities of modeling UHSC reinforced with randomly dispersed and oriented short-fibers. A multi-scale approach is proposed and validated analytically in a one-dimensional case, and validated experimentally in a three-dimensional case. This approach is used to create a homogenized model of a reinforced UHSC panel that is subjected to a blast load and the model is validated experimentally.

Chapter 2

Impact & Blast Effects on Cementitious Materials

2.1 Introduction

The response of a target under high-rate loading, like blast or impact, will depend on numerous variables. Target geometry, structural support system, material, and energy of the impact (or blast) all drastically change the behavior of the system. A clear understanding of the response characteristics of concrete to blast and ballistic impact is crucial in order to effectively protect the defenses. Significant advancements in phenomenological and experimental characterization of complex materials, numerical modeling and simulation techniques, and computational speed capabilities of modern computers, are enabling analysts to more accurately study the dynamic response of different structures subjected to blast and high-velocity impact. Reliable simulation of structural response to these dynamic loads is an incredibly useful way to reduce the required number of experiments and, hence, the overall research costs.

2.2 Characterization of Dynamic Loads

2.2.1 Impact

The inclusion of high-velocity impact dynamics in engineering practice allows analysts to account for the effects of penetrating fragments, accidental loads, and collisions. Moreover, it allows for a more thorough design of lightweight protective structures for civil and military use. Depending upon the type and velocity of the impacting bodies, the structural response of a target can vary from recoverable elastic deformation to material rupture with local material state transitions. If a material is stressed by ballistic impact, shock waves are generated, and such waves are capable of creating pressures of a magnitude which can far exceed the material’s peak strength. In these circumstances, a solid material at the early stages of the impact event can be considered as a compressible fluid, with strength effects appearing later [56].

The response of a structure to an intense, impulsive loading is very complex. Over the years, sophisticated mathematical solutions have been put forward for various loading conditions, but most are for semi-infinite bodies. When a projectile or blast wave impacts a solid target (normal to the surface), the governing equations for both bodies are: (1) conservation of mass, (2) conservation of momentum, and (3) conservation of energy. These equations are commonly summarized as Rankine-Hugoniot relations and are commonly known as "jump" equations, which do not describe a property of a specific material, but instead relate the change in response variables across a shock front. The final pressure and relative volume reached depend on the initial conditions present when the shock arrives [13].

This situation can be summarized by a uniform pressure P_1 suddenly applied to one face of a plate of compressible material which is initially at pressure P_0. This pulse propagates as a wave of velocity U_s. Application of P_1 compresses the material to a new density ρ_1 and at the same time accelerates the compressed material to a velocity U_p. A segment of the material (of unit cross sectional area) normal to the direction of wave travel is considered in Figure 2.1. The position of the shock front at some instant of time is indicated by the line *AA*. An elemental time *dt* later, the shock front has advanced to *BB* while the matter initially at *AA* has moved to *CC*. Across the shock front, mass, momentum, and energy is conserved [57].

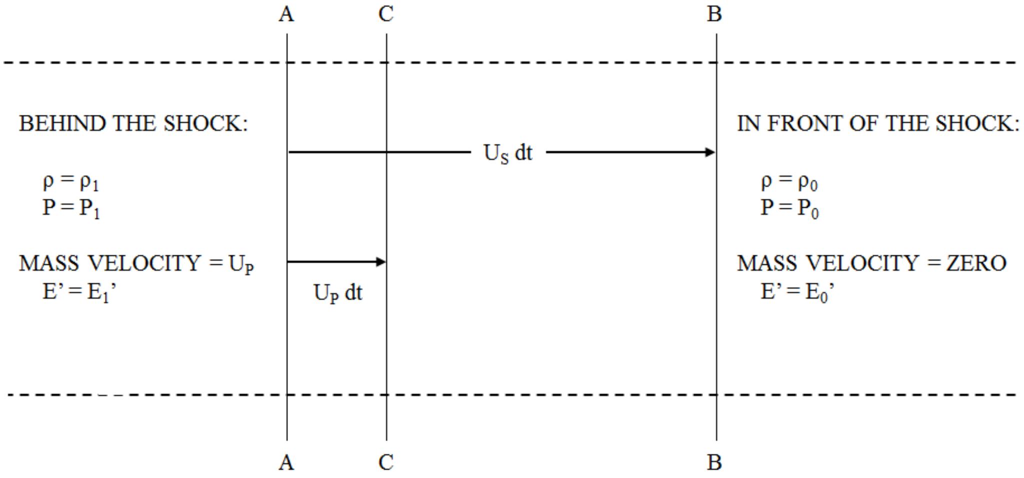

Figure 2.1 Progress of a plane shock wave

Using the assumption of steady-state flow, the basis of Rankine-Hugoniot conditions is determined by the one-dimensional Euler equations of mass, momentum, and energy, as depicted by Eqs. (2.1)-(2.3) [2].

$$\frac{\delta\rho}{\delta t}+\rho\frac{\delta v}{\delta x}=0 \tag{2.1}$$

$$\frac{\delta\rho v}{\delta t}+\rho v\frac{\delta v}{\delta x}+\frac{\delta p}{\delta x}=0 \tag{2.2}$$

$$\frac{\delta e}{\delta t}+\rho v\frac{\delta e}{\delta x}+\rho v\frac{\delta v^2}{\delta^2 x}+v\frac{\delta p}{\delta x}=0 \tag{2.3}$$

By balancing the mass in front (state of the material on the right side of line *BB* in Figure 2.1) and behind (state of the material on the left side of line *AA* in Figure 2.1), the shock wave gives

$$\rho_0 v_0=\rho_1 v_1 . \tag{2.4}$$

From Figure 2.1 it can be concluded that $v_0 = U_s$ (line *BB*) and $v_1 = U_s – U_p$ (line *CC*). Substituting the terms in Eq. (2.4) gives the first Rankine-Hugoniot condition. Essentially, conservation of mass across the shock front is being expressed by ensuring that the mass of material encompassed by the shock wave ($\rho_0 U_s dt$) ends up occupying the volume ($U_s – U_p$)dt at density ρ_1. Therefore,

$$\rho_0 U_s=\rho_1\left(U_s-U_p\right). \tag{2.5}$$

The steady-state equation for the conservation of momentum can be defined in one-dimension as

$$\frac{\delta p}{\delta x}+\rho v\frac{\delta v}{\delta x}=0 . \tag{2.6}$$

On balancing Eq. (2.6) on both sides yields

$$p_0 + \rho_0 U_s^2 = p_1 + \rho_1 \left(U_s - U_p\right)^2 . \tag{2.7}$$

Rewriting of Eq. (2.7) leads to

$$p_1 - p_0 = \rho_0 U_s^2 - \rho_1 \left(U_s - U_p\right)^2 . \tag{2.8}$$

By substituting Eq. (2.5) into Eq. (2.8) and by noting that the rate of change of momentum of a mass of material $\rho_0 U_s dt$ in time dt is accelerated to a velocity U_p by a net force $p_1 - p_0$, the conservation of momentum can be expressed as

$$p_1 - p_0 = \rho_0 U_s U_p . \tag{2.9}$$

The steady-state equation for conservation of energy can be defined in one-dimension as

$$\rho v \frac{\delta e}{\delta x} + \rho v \frac{\delta v^2}{\delta^2 x} + v \frac{\delta p}{\delta x} = 0 . \tag{2.10}$$

On balancing the energy on two sides of the shock gives

$$\left(U_s - U_p\right)\left[p_1 + \rho_1 E_1 + \frac{\rho_1 \left(U_s - U_p\right)^2}{2}\right] = U_s \left(p_0 + \rho_0 E_0 + \frac{\rho_0 U_s^2}{2}\right). \tag{2.11}$$

Reordering and substituting Eqs. (2.5) and (2.9) into Eq. (2.11) shows that the expression for conservation of energy across the shock front is obtained by equating the work done by the shock wave with the sum of the increase of both kinetic and internal energy of the system, given by

$$P_1 U_p = \tfrac{1}{2}\rho_0 U_s U_p^2 + \rho_0 U_s \left(E_1^{'} - E_0^{'}\right), \tag{2.12}$$

where $E^{'}_0$ and $E^{'}_1$ are the specific internal energy in front and behind the shock front, respectively [2]. If it is assumed that ρ_0, P_0, and $E_0^{'}$ are known, then three equations with five unknowns remain. By eliminating U_s and U_p from the energy equation, Eq. (2.11) can be rewritten as

$$\frac{p_1}{\rho_1} + E_1^{'} + \tfrac{1}{2}\left(U_s - U_p\right)^2 = \frac{p_0}{\rho_0} + E_0^{'} + \tfrac{1}{2}U_s^2 \,. \tag{2.13}$$

By eliminating U_s and U_p and using Eqs. (2.5) and (2.9), the resulting equation is known as the Rankine-Hugoniot relation:

$$E_1^{'} - E_0^{'} = \tfrac{1}{2}\left(V_0 - V_1\right)\left(P_1 + P_0\right) = \frac{1}{2}\left(\frac{1}{\rho_0} - \frac{1}{\rho_1}\right)\left(P_1 + P_0\right). \tag{2.14}$$

As a projectile impacts a target at a high strain-rate, there is no time for heat to be conducted away from the impact region. Therefore the impact process becomes adiabatic and no entropy is generated so that $pV^{\gamma} = c$ applies. The Rankine-Hugoniot relation can therefore be reduced to:

$$E_1^{'} - E_0^{'} = \frac{1}{2}\left(p_1 - p_0\right)\left(\frac{1}{\rho_0} + \frac{1}{\rho_1}\right). \tag{2.15}$$

2.2.2 Blast Scenarios

A very simplistic definition of a blast load is a violent burst of wind, or the effect or accompaniment of such a burst. This violent effect consists of a shock front accompanied by an instantaneous increase in ambient atmospheric pressure followed by a monotonic decrease in pressure below the ambient atmospheric pressure.

This creates a loading profile similar to that shown in Figure 2. Along with the drastic changes in pressure that are associated with shock waves are the similarly dramatic changes in temperature and density. A blast is usually a result of a sudden expansion of some energy source. The key parts of this definition are the words “sudden expansion”. It is therefore not only the large amount of pressure build-up that makes an explosion dangerous, but also the presence of a large impulse (the area under the pressure-time curve). So whether the contributory energy source is the mundane popping of a balloon or a bare charge of TNT, the common feature in all explosions is that a very sudden expansion occurs [5].

Explosions can be characterized on the basis of their nature as physical, chemical, or nuclear events. In a physical explosion, energy may be released from the catastrophic failure of a container of compressed gas or the ignition of explosive material. Explosive materials can be classified by their physical state as solids, liquids, or gases. Solid explosives are primarily high explosives for which blast effects are best known. They can also be classified on the basis of their sensitivity to ignition as secondary or primary explosive. Examples of primary explosives are materials like mercury fulminate and lead azide. Secondary explosives when detonated create a shock wave which can result in widespread, catastrophic damage to the surroundings. Examples of secondary explosives are trinitrotoluene (TNT) and ammonium nitrate/fuel oil (ANFO).

The detonation of a condensed high explosive generates hot gases under pressure up to 30 GPa and a temperature up to 3000-4000^{o}C. The hot gas expands forcing out the volume it occupies. As a result, a layer of compressed air (the blast wave) forms in front of this expanding gas volume containing most of the energy released in the explosion. This blast wave instantaneously increases to a value of pressure above the ambient atmospheric pressure. This is referred to as the “side-on overpressure” that decays as the shock wave expands outward from the explosion source. After a short time, the pressure behind the front may drop below the ambient pressure as shown in Figure 2.2. During such a negative phase of pressure, a partial vacuum is created and the air is sucked inward. This is also accompanied by high suction winds that carry the debris for long distances away from the explosion source [35]. Typically when discussing air blasts, the speed of the shock front is approximately equivalent to the speed of sound (~340 m/s).

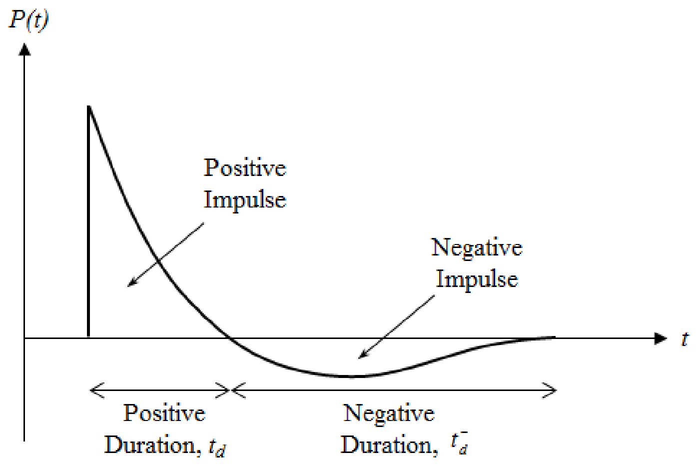

Figure 2.2 Typical blast wave pressure-time history

The incident peak overpressures are also amplified by a reflection factor as the shock wave encounters an object or structure in its path. These reflection factors are typically greatest for normal incidence and diminish with the angle of obliquity or angular position relative to the source. Reflection factors are variable and depend on the intensity of the shock wave. Figure 2.3 illustrates the phenomenon of incident and reflected shock waves in the case of an aboveground explosion with epicenter, *W*, reflected shock, *R*, incident shock, *I*, and the Mach stem measured from the triple point of the leading waves.

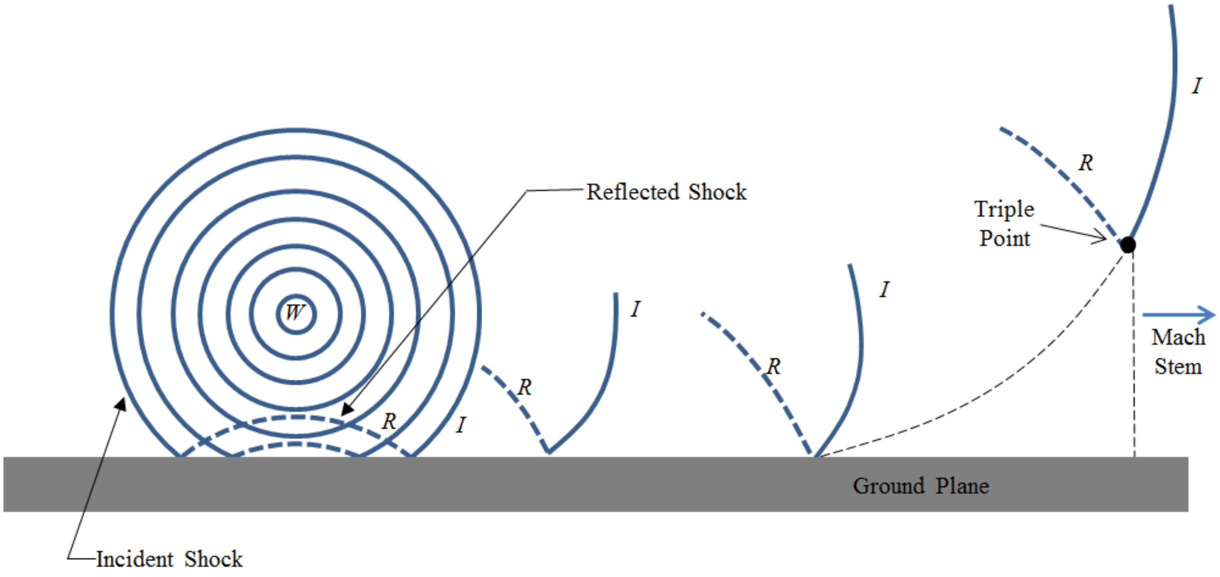

Figure 2.3 Illustration of incident and reflected shock waves through time

Throughout the pressure-time history, two main phases are observed; the portion above ambient pressure is the positive phase of duration t_d, while the portion below ambient pressure is the negative phase of duration t_d^-. The negative phase is longer and of a lower magnitude of pressure than the positive phase. As the range (or stand-off distance) increases, the duration of the positive phase increases, which results in lower peak amplitude and longer duration shock pulse. Therefore, explosive charges situated extremely close to a target impose a highly impulsive, high intensity pressure load over a localized region of the target structure; charges situated farther away produce a lower-intensity, longer-duration uniform pressure distribution over the entire structure. Eventually, the entire structure is immersed within the shock wave, with reflection and diffraction effects creating focusing and shadow zones in a complex pattern around the structure. During the negative phase, the already weakened structure may be subjected to impact by debris that may cause additional damage [35]. An illustration of the relationship between peak reflected pressure and the standoff distance of the target is shown in Figure 2.4. Note that in both cases, the relationship is shown in a logarithmic scale.

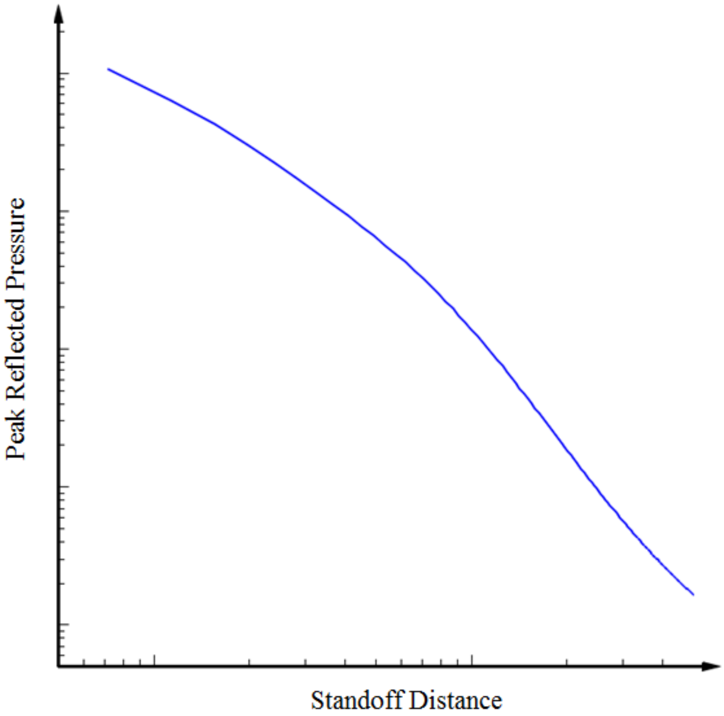

Figure 2.4 Blast wave attenuation away from explosion

2.3 Nature of Cementitious Materials under Dynamic Effects

Analytical and theoretical studies of the nonlinear response of reinforced concrete structures have been, for the most part, focused on the behavior of isolated, simple structural elements like columns and beams. As quantitative data on the failure processes of concrete developed and the number crunching power of computers increased, the scope of nonlinear analysis has expanded. Although finite-element software packages now have a wide range of application in many areas of mechanical stress analysis, inadequate material models is a major stumbling block in limiting structural analysis. This is increasingly true for problems involving brittle, geologic materials like concrete and ceramics. There are general material models available that can reasonably describe the elastic-plastic behavior of reinforced or unreinforced concrete in simple, quasi-static loading conditions. However as advances in concrete and ceramic mixes are made and new materials are developed to improve performance, the generally accepted constitutive equations that describe the basic characteristics of concrete no longer apply [9].

In the idealized case of a target which tends to be elastic/semi-infinite, and the projectile is relatively of small size, the impact energy is primarily propagated as compression (P-waves), shear (S-waves) and Rayleigh waves through the body, emanating from the location of impact. The P- and S-waves will have spherical fronts and Rayleigh wave will have components parallel and normal to the surface dying off exponentially away from the free surface. The P-wave carries least amount of energy; whereas Rayleigh waves carry almost two-third of the impact energy. As P-waves are faster than S-waves, compressive effects will dominate at early times. In the few micro-seconds after impact, the tensile relief waves from the reflected free surface as well as S-waves will become active causing failure in a material which is weak in tension, creating a crater surrounding the impact region. In the meantime the P-wave continues to travel radially, dissipating its energy as heat energy. The velocities of propagation for these two types of disturbances are given as

$$c_{L,U}^2 = \frac{\lambda + 2\mu}{\rho} = \frac{E(1-\nu)}{\rho(1+\nu)(1-2\nu)}, \tag{2.16}$$

$$c_{L,B}^2 = \frac{E}{\rho}, \tag{2.17}$$

$$c_{S,U}^2 = \frac{\mu}{\rho} = \frac{G}{\rho} = \frac{E}{2\rho(1+\rho)}, \tag{2.18}$$

$$c_{S,B}^2 = \frac{G}{\rho}, \tag{2.19}$$

where E is the elastic modulus, ν is Poisson's ratio, ρ is material density, λ and μ are Lamé parameters, G is the shear modulus, the subscripts L and S represent longitudinal and shear and U and B represent unbounded and bounded. Compression waves can be generated in liquids as well as solids because the energy travels through the atomic structure by a series of compressions and expansion (rarefaction) phenomena. Shear waves require an acoustically solid material for effective propagation, and therefore, are not effectively propagated in liquids or gases. Shear waves are relatively weak when compared to longitudinal waves. In fact, shear waves are usually generated in materials using some of the energy from longitudinal waves.

More to the relevance of the present research is the topic of shock waves. Traditionally, work on shock waves has been done with plate-like geometries. Plate impact situations generate a state of local uniaxial strain but three-dimensional stress. A traditional, uniaxial stress-strain curve, as determined from one-dimensional material testing (in tension or compression), does not sufficiently represent the state of stress and strain to which a material is subjected under shock loading. Therefore the material constants associated with such curves (i.e. elastic modulus, yield strength, ultimate strength, and elongation) are not by themselves sufficient in characterizing the relative behavior of materials. If we were to visualize a situation where deformation was restricted to one dimension, as in the case of plane waves propagating through a material (lateral strains are zero), the characteristic stress strain curve takes on the form shown in Figure 2.5.

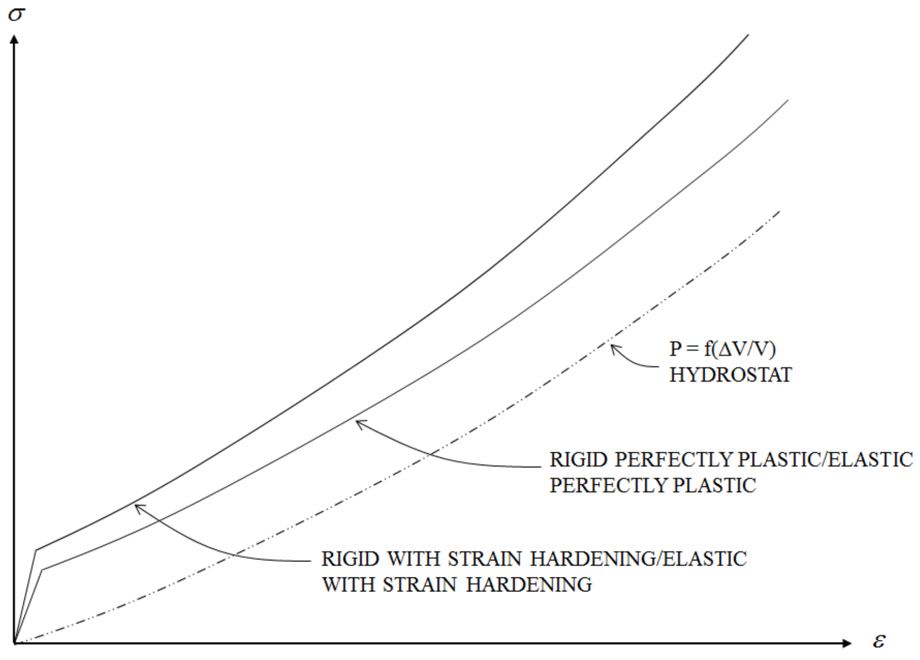

Figure 2.5 Typical stress-strain curve for uniaxial strain

With very high pressures, the pressure-compressibility curve of the above figure, also known as the Hugoniot curve, is the only one that is considered to describe the behavior of a material. At lower pressures, such as those generated by conventional impacts, substantial deviation from the Hugoniot curves occur.

The uniaxial strain curve corresponding to the uniaxial stress condition for an elastic, perfectly plastic material is shown in Figure 2.6 with the following characteristic features: (1) increase in the modulus by a factor of $(1-\nu)/[(1-2\nu)(1+\nu)]$, (2) the Hugoniot elastic limit is σ_{HEL} (the maximum stress for one-dimensional elastic wave propagation in uniaxial strain), and (3) a constant deviation of the stress from the Hugoniot by $2Y_o/3$, where Y_o is the static yield strength. If the yield strength were to change in a strain hardening material, so will the difference between the σ_1 and P curves [57].

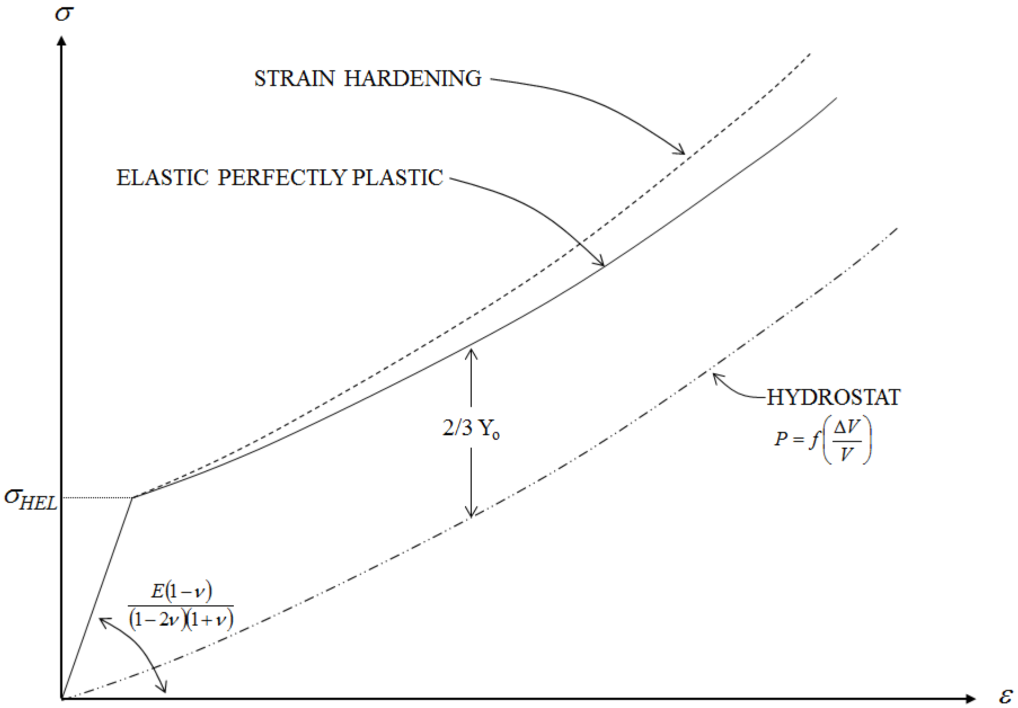

Figure 2.6 Uniaxial strain curve for elastic, perfectly plastic material

If the magnitude of the applied stress pulse is above σ_{HEL}, two waves will propagate through the medium, the elastic wave moving with speed

$$c_E^2 = \frac{E(1-\nu)}{\rho_0(1-2\nu)(1-\nu)} \quad , \tag{2.20}$$

followed by a plastic wave moving with speed

$$c_P^2 = \frac{\sigma_B - \sigma_{HEL}}{\rho_{HEL}(\varepsilon_B - \varepsilon_A)} . \tag{2.21}$$

As previously described, the scenarios encountered by a structure due to blast are innumerable. To simplify this phenomenon, only cases where the stand-off distance of the structure is sufficiently large so that the blast wave can be treated as uniform over the exposed area will need to be considered. In this case, the loading mechanism is simple and an appropriate material model needs only be able to handle high-rate and high-pressure effects. Theoretically any constitutive model that can successfully simulate high-rate impact and penetration events can handle aforementioned types of blast simulations. For the present work, problems of material failure near a free surface some distance from the localized area of application of an impulsive load have been studied extensively. In the case of ceramics or cementitious materials that have high compressive strengths but relatively weak tensile strengths, spalling at the free surfaces is a phenomenon to be expected due to reflection of incident-compressive impulses generated by high-velocity ballistic impact. Figure 2.7 illustrates the progressive effects that take place during an impact and penetration event of a thin panel during high velocities. In the first few microseconds of impact, local material cratering takes place. Directly in front of the projectile, the material then undergoes local material compaction and, due to the high rate of loading, Poisson effects do not have time to take place, which would normally allow for some of the material in front of the projectile to expand outward radially. Therefore, this effect is reminiscent of radially confined compression. As described later, this is the motivation for applying a material model that has been calibrated using the results of triaxial compression experiments. As all these events are in progress, the strong compressive shock wave has already weakened as it traversed through the plate thickness and is reflected off the back surface. This shock wave reflection in turn generates a tensile shock wave, which when interacting with the compressive waves, will lead to cracking on the rear face of the panel and cause fragmentation (or spalling) of the material [48].

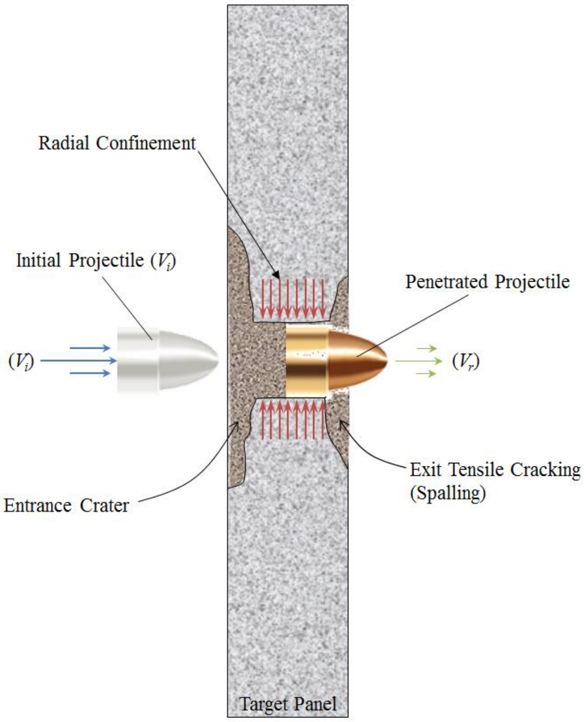

Figure 2.7 Physical characteristics of high-velocity penetration of a brittle target

2.4 Fiber Reinforcement of Concrete for Improved Blast Performance

Concrete and other cementitious materials have always been partnered well with reinforcement. Reinforcement can come in the form of rebar, prestressed strands, general long fibers, woven fibers, and short fibers. In discussing reinforcement of a cementitious or concrete composite, the brittle material is typically referred to as the matrix and the reinforcement as the fiber. These reinforcing fibers have typically been made of metals like steel, but new research into alternatives has shown the efficacy of polymeric fibers like polypropylene. The main purpose of reinforcement is to improve the composite's ductility—an important material property for protection against the stresses caused by blast and impact effects. Generally, the increase in a material's ductility will increase the material's toughness, or the potential for energy dissipation. This material property has been found experimentally to be much more important in blast resistance than impact. The phenomena associated with impact are highly localized and so reinforcing fibers have little to no effect in improving the impact resistance of a structure.

In a UHSC material with a brittle matrix, maximum ductility is achieved through an optimized selection of fiber reinforcement. For thin panels as described in section 2.3, the preferred method for UHSC reinforcement is randomly distributed short fibers, because conventional continuous reinforcement is not practical for thin panels. Due to the extremely low tensile strength of the brittle matrix, appropriate fibers must be selected carefully to optimally bridge matrix cracks [15]. When the cementitious composite is designed properly, additional loading energy is absorbed as a fiber partially pulls out of the matrix before arresting crack growth, causing another crack to form and propagate, and this process repeats. But in order for this progressive cracking condition to exist, a balanced design between the fiber, matrix, and bond (interface) is required [28].

When modeling short-fiber reinforced UHSC, there are several mechanics-based issues that must be overcome. The first is that since the manufacturing process of this composite, whether in the lab or in the field, will lead to a random distribution of fibers at similarly random orientations. This randomness is somewhat affected by the shape of the structure since concrete uses molds in order to take shape during curing and fibers cannot exceed a mold boundary. These fibers can also touch but cannot physically intersect one another (i.e. occupy the same three-dimensional space). Both of these issues require a statistical approach when creating a model that can accurately replicate the seemingly random distribution and orientation of fibers.

Another difficulty arises from the simple fact that fibers create material discontinuities within the matrix material and, therefore, cause crack-like stress concentrations in the stress fields of the matrix itself. This causes internal cracking to occur in a composite that makes modeling challenging, especially since a model of this type of composite requires certain finesse in the finite element meshing.

The final complication is related to the bond between fiber and matrix. Many modeling efforts over the past 50 years regularly assume a perfect bond between geometric inclusions and matrix material (i.e. share nodes at the interface boundary). It wasn’t until the earliest publication on the application of the finite element method to the analysis of reinforced concrete structures was presented by Ngo and Scordelis in 1967 [36]. In their initial study, simple beam structures were analyzed using a special “bond-link” element that connected steel to concrete to describe the bond-slip effect. This bond-link element essentially consisted of two orthogonal (imaginary) springs with no physical dimensions that can connect and transmit shear and normal forces between a reinforcing steel node and an adjacent concrete node [27]. Similar techniques are used today to transmit these bond forces, but additional complexities are added when the degradation of bond stiffness is considered due to fiber-pullout. It is complex at a modeling level, but even more so experimentally. All the difficulties just outlined are described and solved in much greater detail in Chapter 8.

Chapter 3

Significant Constitutive Models for Cementitious Materials under High-Rate Loading

3.1 Introduction

Over the past few years, a number of material models have been put forward by Johnson, Holmquist, and their coworkers to describe the behavior of concrete and other brittle geologic materials under large strain, high-strain rate, and high-pressure impacting conditions. Three of these models, the HJC model [18], the JHB/JH-1 model [17], and the JH-2 model [23], are particularly noteworthy. It has also been found that a similar material behavior can be customized using a combination of the Drucker-Prager plasticity model and an equation of state [46]. Each of these models contain the same three basic elements: (1) an equation of state (EOS) for the pressure-volume relation that includes the nonlinear effects of compaction, (2) a representation of the deviatoric strength of the intact and fractured material in the form of a pressure-dependent yield surface, and (3) a damage model that transitions the material from the intact state to the fractured state. These basic elements will now be outlined and discussed in detail

3.2 Holmquist-Johnson-Cook (HJC) Model

3.2.1 Pressure

The pressure-volume response of this model is shown schematically in Figure 3.1. The pressure is given as a function of the measure of volumetric strain

$$\mu = \frac{\rho}{\rho_0} - 1 \tag{3.1}$$

where ρ is the current density and ρ_0 is the reference density. In compression the response is divided into three regions. In the first region the pressure increases linearly with μ from zero to P_{crush}, which corresponds to the onset of crushing (compaction) when $\mu = \mu_{crush}$. The second region, or the transition region, is associated with the crushing behavior of concrete. Unloading in this region occurs along a modified path that is interpolated from the adjacent regions. In this region the material accumulates plastic volumetric strain, μ^{pl}, until the air voids are fully compressed, corresponding to the point $\left(\mu_{lock}, P_{lock}\right)$. Beyond this point, in the third region, the material is assumed to be fully dense (i.e. all air voids have been completely removed) with the pressure given by the nonlinear elastic relation

$$P = K_1\overline{\mu} + K_2\overline{\mu}^2 + K_3\overline{\mu}^3 \tag{3.2}$$

where K_1, K_2, and K_3 are material constants, and the modified volumetric strain $\overline{\mu}$ is defined as

$$\overline{\mu} = \frac{\mu - \mu_{lock}}{1 + \mu_{lock}}. \tag{3.3}$$

The modified volumetric strain is used so that K_1, K_2, and K_3 are equivalent to those used in material with no voids [18].

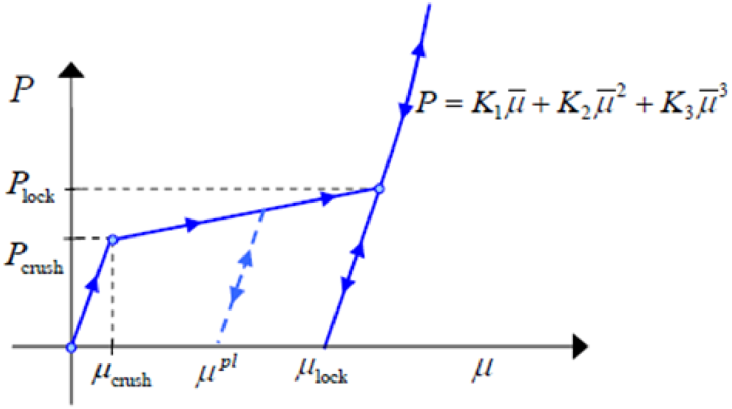

Figure 3.1 Pressure-volume response for the HJC concrete model [18]

3.2.2 Strength

The HJC model assumed that the normalized strength of the material can be expressed as functions of the pressure and strain rate as

$$\sigma^* = \left(A(1-D) + BP^{*N}\right)\left(1 + C\ln\dot{\varepsilon}^*\right). \tag{3.4}$$

The normalized strength of the material is defined as $\sigma^* = \sigma / f_c^{'}$ where σ is the von Mises equivalent stress and $f_c^{'}$ is the uniaxial compressive strength under quasi-static loading. In Eq. (3.4), *A*, *B*, *N*, and *C* are material constants; *D* is the scalar damage variable (defined in the next section), where $0 \le D \le 1$ ($D = 0$ corresponding to fully intact material and $D = 1$ corresponding to fractured material); $P^* = P / f_c^{'}$ is the normalized pressure, and $\dot{\varepsilon}^* = \dot{\bar{\varepsilon}}^{pl} / \dot{\varepsilon}_0$ is the dimensionless strain rate, where $\dot{\bar{\varepsilon}}^{pl}$ is the equivalent plastic strain rate and $\dot{\varepsilon}_0$ is the reference strain rate. Plastic flow is assumed to be isochoric following a Mises flow surface. The evolution of the plastic strain tensor is given as $\dot{\varepsilon}^{pl} = \dot{\bar{\varepsilon}}^{pl}$ **n**, where **n** is the normal to the Mises flow surface [18].

3.2.3 Damage

The scalar damage variable accumulates both with equivalent plastic strain and volumetric plastic (or compaction) strain according to

$$D = \sum \frac{\Delta\bar{\varepsilon}^{pl} + \Delta\mu^{pl}}{\Delta\bar{\varepsilon}^{pl}\left(P^*\right)} \tag{3.5}$$

$$\text{with } \bar{\varepsilon}^{pl} = D_1\left(P^* + T^*\right)^{D_2}; \qquad \bar{\varepsilon}^{pl}_{f,\min} \le \bar{\varepsilon}^{pl}_{f} \le \bar{\varepsilon}^{pl}_{f,\max}$$

Here $\Delta\bar{\varepsilon}^{pl}$ is the increment in equivalent plastic strain; $\Delta\mu^{pl}$ is the increment in the volumetric compaction strain; $\Delta\bar{\varepsilon}^{pl}\left(P^*\right)$ is the equivalent plastic strain to fracture under constant pressure; $T^* = T / f_c^{'}$ is the normalized maximum tensile hydrostatic stress; and D_1 and D_2 are material constants. The model also offers the optional parameters $\bar{\varepsilon}^{pl}_{f,\min}$ and $\bar{\varepsilon}^{pl}_{f,\max}$, which are provided for additional flexibility to limit the minimum and maximum values of the fracture strain [18].

3.3 Johnson-Holmquist-Beissel (JHB/JH-1) Model

The JHB model is similar to the JH-1 model except that it has an analytic description for the strength of the intact and fractured material, an analytic function for the failure strain, and has the capability to include a pressure-driven phase change. Therefore these models are presented here together.

3.3.1 Pressure

In the absence of a phase change, the pressure-volume relationship is assumed to be given by an equation of state of the form

$$P = \begin{cases} K_1\mu + K_2\mu^2 + K_3\mu^3 & if \;\; \mu \geq 0 \;\; (compression) \\ K_1\mu & if \;\; \mu < 0 \;\; (tension) \end{cases} \tag{3.6}$$

where μ is as in Eq. (3.1) and K_1, K_2, and K_3 are material constants. The model also includes the effects of dilation (or bulking) that occurs when brittle materials fail by including an additional pressure increment, ΔP, such that

$$\Delta P = -K_1\mu_f + \sqrt{\left(K_1\mu_f\right)^2 + 2\beta K_1\Delta U} \tag{3.7}$$

where μ_f is the current value of μ at the time of failure and β is the fraction of the elastic energy loss converted to potential hydrostatic energy ($0 \leq \beta \leq 1$). The bulking pressure is computed only for failure under compression (μ_f>0) [17].

The pressure-volume relationships become more complex during unloading, especially in the presence of hysteresis. A hysteresis parameter *h* is provided to specify the amount of hysteresis. Different unloading behaviors are illustrated in Figure 3.2 for the cases with no hysteresis (*h* = 0), maximum hysteresis (*h* = 1), and partial hysteresis (*h* = 0.5) [17].

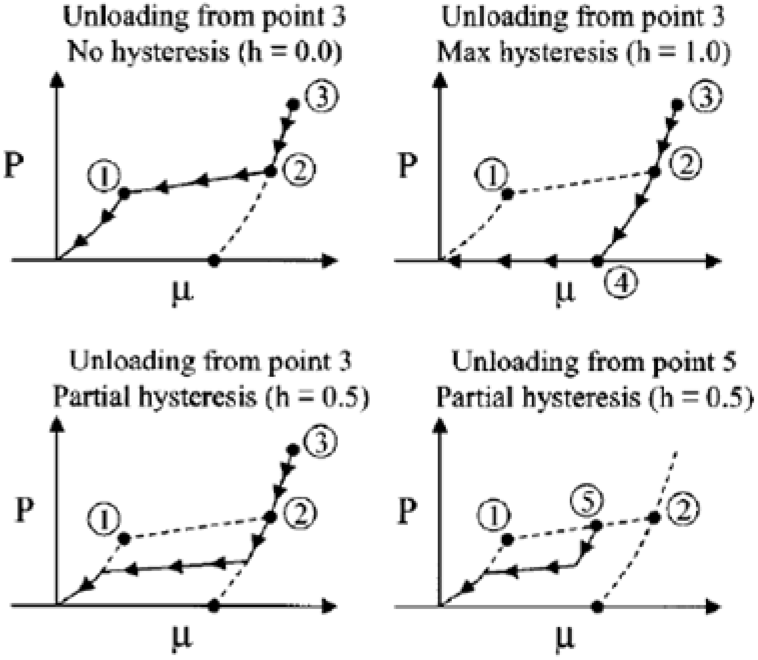

Figure 3.2 Hysteresis model for JHB/JH-1 model [17]

3.3.2 Strength

The strength of the material is expressed in terms of the von Mises equivalent stress, σ, and is a function of the pressure, *P*, the dimensionless equivalent strain rate, $\dot{\varepsilon} = \dot{\bar{\varepsilon}}^{pl} / \dot{\varepsilon}_0$ (where $\dot{\bar{\varepsilon}}^{pl}$ is the equivalent plastic strain rate and $\dot{\varepsilon}_0$ is the reference strain rate), and the scalar damage variable *D* (0 ≤ *D* ≤ 1). For the intact (undamaged) material, *D* = 0, whereas for the fully damaged material, *D* = 1. For a dimensionless strain rate of $\dot{\varepsilon}^* = 1.0$, the strength of the intact material (*D* = 0) takes the form

$$\sigma = \begin{cases} \sigma_i (P+T)/(P_i+T) & if\, P \le P_i \\ \sigma_i + \left(\sigma_i^{\max} - \sigma_i\right)\{1 - \exp[-\alpha_i (P - P_i)]\} & if\, P \ge P_i \end{cases} \tag{3.8}$$

where $\alpha_i = \sigma_i / \left[\left(\sigma_i^{\max} - \sigma_i\right)\left(P_i + T\right)\right]$. In the equations above, P_i, T, σ_i, and σ_i^{max} are material parameters. The strength of the fractured material (D = 1) is given by

$$\sigma = \begin{cases} \sigma_f P / P_f & if\ P \leq P_f \\ \sigma_f + \left(\sigma_f^{\max} - \sigma_f\right)\left\{1 - \exp\left[-\alpha_f \left(P - P_f\right)\right]\right\} & if\ P \geq P_f \end{cases} \tag{3.9}$$

where $\alpha_f = \sigma_f / \left[\left(\sigma_f^{\max} - \sigma_f\right) P_f\right]$. In the equations above, P_f, σ_f, and σ_f^{max} are material parameters. The intact and fractured strengths shown above are for a dimensionless strain rate of $\dot{\varepsilon}^* = 1.0$. The strength at other strain rates is computed using a Johnson-Cook strain-rate dependence law of the form

$$\sigma = \sigma_0 \left(1 + C \ln \dot{\varepsilon}^*\right) \tag{3.10}$$

where σ_0 is the strength for $\dot{\varepsilon}^* = 1.0$, and C is a material parameter (strain rate constant). Plastic flow is assumed to be isochoric using a Mises flow surface. The evolution of the plastic strain tensor is again given as $\dot{\varepsilon}^{pl} = \dot{\bar{\varepsilon}}^{pl}$ **n**, where **n** is the normal to the Mises flow surface [17].

3.3.3 Damage

The model uses a damage accumulation criterion that is similar to that in the Johnson-Cook fracture model. The damage initiation parameter, ω, accumulates with plastic strain according to

$$\omega = \sum \frac{\Delta \bar{\varepsilon}^{pl}}{\bar{\varepsilon}_f^{pl}(P)}. \tag{3.11}$$

Here $\Delta\bar{\varepsilon}^{pl}$ is the increment in equivalent plastic strain and $\bar{\varepsilon}_f^{pl}(P)$ is the equivalent plastic strain to fracture under constant pressure, defined as

$$\bar{\varepsilon}_f^{pl} = D_1 \left(P^* + T^*\right)^{D_2}; \qquad \bar{\varepsilon}_{f,\min}^{pl} \le \bar{\varepsilon}_f^{pl} \le \bar{\varepsilon}_{f,\max}^{pl} \tag{3.12}$$

where D_1 and D_2 are material constants and $P^* = P/\sigma_i^{max}$ and $T^* = T/\sigma_i^{max}$. The model also offers the optional parameters $\bar{\varepsilon}_{f,min}^{pl}$ and $\bar{\varepsilon}_{f,max}^{pl}$ which are provided for additional flexibility to limit the minimum and maximum values of the fracture strain. The JHB model assumes that the material fails instantateously, $D = 1$, when $\omega = 1$. For other values of $\omega < 1$, there is no damage ($D = 0$) and the material preserves its intact strength [17].

3.4 Johnson-Holmquist (JH-2) Model

3.4.1 Pressure

The pressure-volume relationship is assumed to be given by an equation of state of the form

$$P = \begin{cases} K_1\mu + K_2\mu^2 + K_3\mu^3 & if \;\; \mu \ge 0 \;\; (compression) \\ K_1\mu & if \;\; \mu < 0 \;\; (tension) \end{cases} \tag{3.13}$$

where μ is defined as in Eq. (3.1) and K_1, K_2, and K_3 are material constants (K_1 is the initial bulk modulus). The model includes the effects of dilation (or bulking) that occur when brittle materials fail by including an additional pressure increment, ΔP, such that

$$P = K_1\mu + K_2\mu^2 + K_3\mu^3 + \Delta P \tag{3.14}$$

The pressure increment is determined from energy considerations. The decrease in strength when the material undergoes damage (as it goes from an intact state to a failed state) produces a decrease in the deviatoric elastic energy, ΔU. This loss of elastic energy is converted into potential hydrostatic energy by incrementally increasing ΔP according to

$$\Delta P_{t+\Delta t} = -K_1 \mu_{t+\Delta t} + \sqrt{\left(K_1 \mu_{t+\Delta t} + \Delta P_t\right)^2 + 2\beta K_1 \Delta U} \tag{3.15}$$

where β is the fraction of the elastic energy loss converted to potential hydrostatic energy ($0 \leq \beta \leq 1$).

An important experimental data point commonly used for determining the intact strength is the Hugoniot Elastic limit, or *HEL*. The *HEL* is the net compressive stress (containing both pressure and deviatoric stress components) at which a one-dimensional (uniaxial strain) shock wave exceeds the elastic limit of the material. Thus

$$HEL = P_{HEL} + \tfrac{2}{3}\sigma_{HEL} \tag{3.16}$$

This expression can be expanded using the above pressure-density relation and the elastic relations for uniaxial strain conditions to obtain

$$HEL = K_1 \mu_{HEL} + K_2 \mu_{HEL}^2 + K_3 \mu_{HEL}^3 + \tfrac{4}{3} G \frac{\mu_{HEL}}{1 + \mu_{HEL}} \tag{3.17}$$

where μ_{HEL} is the volumetric strain at the *HEL*. This expression can be used to compute μ_{HEL} from *HEL* and then substitute back in the pressure-density relation to obtain P_{HEL} [23].

3.4.2 Strength

The strength of the material is expressed in terms of the normalized von Mises equivalent stress as

$$\sigma^* = \sigma_i^* - D\left(\sigma_i^* - \sigma_f^*\right) \tag{3.18}$$

where σ_i^* is the normalized intact equivalent stress, σ_f^* is the normalized fractured equivalent stress, and *D* is the damage variable (defined in the next section). The normalized equivalent stresses σ^*, σ_i^*, and σ_f^* have the general form $\sigma^* = \sigma/\sigma_{HEL}$, where σ is the actual von Mises equivalent stress and σ_{HEL} is the equivalent stress at the Hugoniot elastic limit (HEL), at which a one-dimensional (uniaxial strain) shock wave exceeds the elastic limit of the material. The model assumes that the normalized intact and fractured stresses can be expressed as functions of the pressure and strain rate as

$$\sigma_i^* = A\left(P^* + T^*\right)^N \left(1 + C \ln \dot{\varepsilon}^*\right) \leq \sigma_i^{\max} \tag{3.19}$$

$$\sigma_f^* = B\left(P^*\right)^M \left(1 + C \ln \dot{\varepsilon}^*\right) \leq \sigma_f^{\max} \tag{3.20}$$

The material parameters are *A*, *B*, *C*, *M*, and *N*, and the optional limits for the strengths σ_i^{max} and σ_f^{max}. The normalized pressure is defined as $P^* = P/P_{HEL}$, where P is the actual pressure and P_{HEL} is the pressure at the HEL. Similarly, the normalized maximum tensile hydrostatic pressure $T^* = T/P_{HEL}$, where T is the maximum tensile pressure that the material can withstand. Rate effects are included using the Johnson-Cook strain-rate dependence criterion. The dimensionless strain rate is given as $\dot{\varepsilon}^{pl} = \dot{\bar{\varepsilon}}^{pl}/\dot{\varepsilon}_0$, where $\dot{\bar{\varepsilon}}^{pl}$ is the equivalent plastic strain rate and is the reference (or threshold) strain rate. Plastic flow is again assumed to be isochoric (volume preserving) using a von Mises flow surface. The evolution of the plastic strain tensor is given as $\dot{\varepsilon}^{pl} = \dot{\bar{\varepsilon}}^{pl}$ **n** where **n** is the normal to the von Mises flow surface [23].

3.4.3 Damage

The model uses a damage accumulation criterion that is similar to that in the Johnson-Cook fracture model. The damage initiation parameter, ω, accumulates with plastic strain according to

$$\omega = \sum \frac{\Delta\bar{\varepsilon}^{pl}}{\bar{\varepsilon}_f^{pl}(p)} \tag{3.21}$$

$$\text{where } \bar{\varepsilon}^{pl} = D_1\left(P^* + T^*\right)^{D_2};\ \bar{\varepsilon}_{f,\min}^{pl} \leq \bar{\varepsilon}_f^{pl} \leq \bar{\varepsilon}_{f,\max}^{pl}$$

Here $\Delta\bar{\varepsilon}^{pl}$ is the increment in equivalent plastic strain and $\bar{\varepsilon}_f^{pl}(P)$ is the equivalent plastic strain to fracture under constant pressure, and D_1 and D_2 are material constants. The optional parameters $\bar{\varepsilon}_{f,min}^{pl}$ and $\bar{\varepsilon}_{f,max}^{pl}$ are provided for additional flexibility to limit the minimum and maximum values of the fracture strain. The JH-2 model assumes that the damage variable increases progressively with plastic deformation by setting $D = \omega$. In an earlier version of the model (the JH-1 model), the material was assumed to fail instantaneously by setting $D = 1$ when $\omega = 1$. The different damage models are summarized in the table below [23].

Table 3.1 Damage evolution laws for two JH models

Damage Evolution	
JHB/JH-1	JH-2
$D = 0$ if $\omega < 1$ $D = 1$ if $\omega = 1$	$D = \omega$

3.5 Drucker-Prager Model

The Drucker-Prager (DP) plasticity model is a yield criterion that is traditionally used to deal with the plastic deformation of soils, rock, concrete, polymers, foams, and other pressure-dependent materials. By using a combination of the DP plasticity model and an equation of state, a model can be created that somewhat replicates the behavior of the JH-2 model. In this way, a model is not confined to follow the specific expressions outlined in the JH-2 model and subsequently those material parameters. This allows for the advantage of “generality” of the DP plasticity model and the different available equations of state. To conform with the above JH models, also it is possible to cast the description with three components for the DP plasticity model as well.

3.5.1 Equation of State

The Mie-Grüneisen equation of state (MG-EOS) describes the relation between the pressure and the volume of a solid at a given temperature. It is often used to determine the pressure in a shock-compressed solid. The MG-EOS is linear in energy and the most common form is

$$p - p_H = \Gamma\rho\left(E_m - E_H\right), \tag{3.22}$$

where p_H and E_H are the Hugoniot pressure and specific energy (per unit mass) and are functions of density only, and Γ is the Grüneisen ratio defined as

$$\Gamma = \Gamma_0 \frac{\rho_0}{\rho}, \tag{3.23}$$

where Γ_0 is a material constant and ρ_0 is the reference density. The Hugoniot energy, E_H, is related to the Hugoniot pressure by

$$E_H = \frac{p_H \eta}{2\rho_0}, \tag{3.24}$$

where $\eta = 1 - \rho_0 / \rho$ is the nominal volumetric compressive strain. Elimination of Γ and E_H from the above equations yields

$$p = p_H\left(1 - \frac{\Gamma_0 \eta}{2}\right) + \Gamma_0 \rho_0 E_m \tag{3.25}$$

The equation of state and the energy equation represent coupled equations for pressure and internal energy. The material model solves these equations simultaneously at each material point. A common fit to the Hugoniot data is given by the linear $U_s - U_p$ Hugoniot form

$$p_H = \frac{\rho_0 c_0^2 \eta}{\left(1 - s\eta\right)^2}, \tag{3.26}$$

where c_0 and *s* define the linear relationship between the linear shock velocity, U_s, and the particle velocity, U_p (variables also seen in Eq. (2.5)), given by

$$U_s = c_0 + sU_p \ . \tag{3.27}$$

So by taking Eq. (3.27) and rewriting Eq. (3.25) it follows

$$p = \frac{\rho_0 c_0^2 \eta}{(1 - s\eta)^2}\left(1 - \frac{\Gamma_0 \eta}{2}\right) + \Gamma_0 \rho_0 E_m , \tag{3.28}$$

where $\rho_0 c_0^2$ is equivalent to the elastic bulk modulus at small nominal strains [54]. Without the energy contribution ($\Gamma_0 = 0.0$), the pressure from Eq. (3.28) can now be expressed as

$$p = \frac{\rho_0 c_0^2 \eta}{(1 - s\eta)^2} \ . \tag{3.29}$$

This means that based on the curve fit for a uniaxial strain compressive test (used to determine the K_1, K_2, and K_3 in the JHB, and JH-2 models above), we can determine the parameters c_0 and *s*. This is done by fitting a curve through the experimental data based on Eqs. (3.2) and (3.6) to find K_1 and K_2. Using a Taylor expansion with respect to μ, the linear and quadratic coefficients of the polynomial can be identified as K_1 and K_2 in the pressure density relation for Eqs. (3.2) and (3.6) [46]. This gives

$$K_1 = \rho_0 {c_0}^2 \text{, and} \tag{3.30}$$

$$K_2 = \rho_0 c_0^2 (2s - 1). \tag{3.31}$$

3.5.2 Strength

The yield criteria for this class of models are based on the shape of the yield surface in the meridional plane. The yield surface for D-P models can have a linear form, a hyperbolic form, or a general exponent form. These surfaces are illustrated below in Figure 3.3. The equations for the linear, hyperbolic, and general exponent forms of the D-P models, respectively, are as follows:

Linear: $$F = t - p\tan\beta - d = 0, \tag{3.32}$$

Hyperbolic: $$F = \sqrt{\left(d'|_0 - p_t\,|_0\,\tan\beta\right)^2 + q^2} - p\tan\beta - d' = 0, \tag{3.33}$$

General Exponent: $$F = aq^b - p - p_t = 0, \tag{3.34}$$

where $$t = \frac{1}{2}q\left[1 + \frac{1}{K} - \left(1 - \frac{1}{K}\right)\left(\frac{r}{q}\right)^3\right],$$

β is the slope of the linear yield surface in the *p-t* stress plane and is commonly referred to as the friction angle of the material, *d* is the cohesion of the material, and *K* is the ratio of the yield stress in triaxial tension to the yield stress in triaxial compression (therefore controlling the dependence of the yield surface on the value of the intermediate principal stress).

The yield stress surface uses two invariants, defined as the equivalent pressure stress, p = -(1/3)trace(σ), and the Mises equivalent stress, $q = \sqrt{(3/2)(S:S)}$, where S is the stress deviator defined as $S = \sigma + pI$. In addition, only the linear model also uses the third invariant of the deviatoric stress, defined as $r = \left(\tfrac{9}{2} S \cdot S : S\right)^{1/3}$.

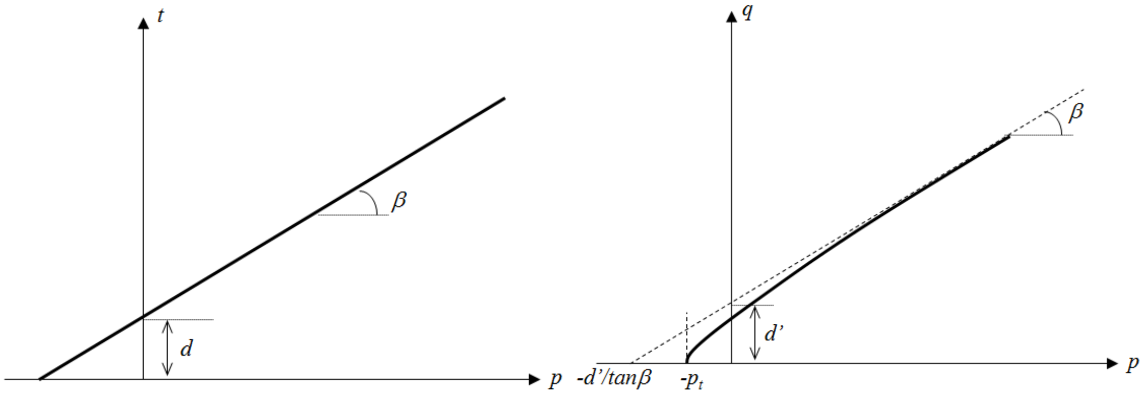

(a) Linear

(b) Hyperbolic

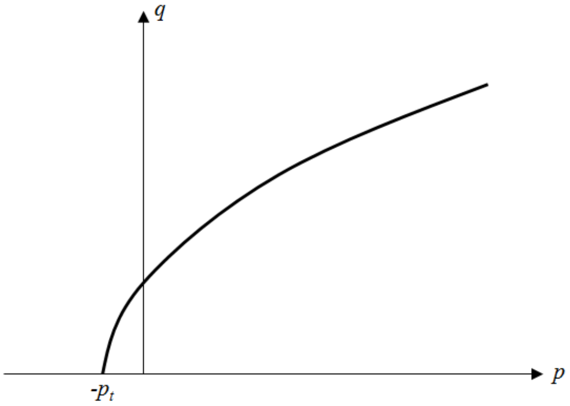

(c) General Exponent

Figure 3.3 Yield surface forms for D-P model

Due to the common shapes of the failure surfaces of cementitious materials, the general exponent model is chosen to be the best-fit representation for most material models. To fit a general exponent curve to experimental data, the following procedure must be completed. A cylindrical test specimen is subjected to some constant confining pressure, $\sigma_1 = \sigma_2$, and an increasing axial load, σ_3, as shown in Figure 3.4 (negative signs shown are to denote compressive pressures whereas positive would imply tensile pressures.

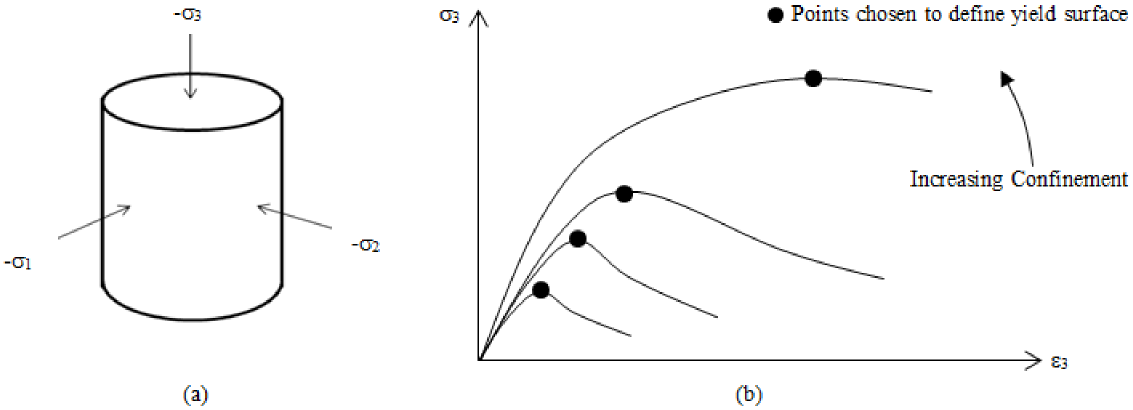

Figure 3.4 (a) Triaxial test schematic (b) Axial stress vs. axial strain plots at various confining pressures

To determine the failure surface data, the following system of equations must be solved

$$p = -\tfrac{1}{3}\left(2\sigma_1 + \sigma_3\right) \tag{3.35}$$

$$q = \sigma_1 - \sigma_3 \tag{3.36}$$

One stress data point from each stress-strain curve at different levels of confinement is plotted in the meridional plane (*p*-*q* plane for the general exponent model). This technique calibrates the shape and position of the yield surface, as shown in Figure 3.3(c) and is adequate to define a model if it is to be used as a failure surface (perfect plasticity). So using Eq. (3.34) and rewriting to be in the form of a failure surface, it follows

$$\sigma = \frac{1}{a^{1/b}}\left(P + P_t\right)^{1/b}, \tag{3.37}$$

where *a*, *b*, and P_t are the only material constants required to define the failure surface. A least-squares fit which minimizes the relative error in stress should be used to obtain the "best fit" values for these constants.

3.5.3 Damage

To define damage initiation and evolution in conjunction with a D-P model the "ductile damage" model is calibrated to reproduce the damage criterion in one of the JH models. The ductile criterion requires the specification of the equivalent plastic strain at the onset of damage, $\bar{\varepsilon}_D^{pl}$, as a function of stress triaxiality, $\eta = -p/q$ and effective plastic strain rate. The criterion for damage initiation is met when the following condition is satisfied:

$$\omega_D = \sum \frac{\Delta \bar{\varepsilon}^{pl}}{\varepsilon_D^{pl}\left(\eta, \dot{\bar{\varepsilon}}^{pl}\right)} = 1, \tag{3.38}$$

where ω_D is a state variable that increases monotonically with plastic deformation. To define this behavior, the uniaxial strain values for the yield surface points in Figure 3.4(b) are translated into values of equivalent plastic strain at the onset of damage, $\bar{\varepsilon}_D^{pl}$, and the corresponding values of *p* and *q* are found for those points based on Eqs. (3.35) and (3.36) in order to determine stress triaxiality, η.

Chapter 4

Development of Improved Constitutive Model

4.1 Introduction

The proposed constitutive model makes use of certain aspects of the previously mentioned models, but improves upon them in certain respects. Outlined below are the same three principal components of our material model and the equations that they use. This model is based on the initial pioneering efforts of the Advanced Fundamental Concrete (AFC) model proposed by Adley and coworkers [3] and was first implemented into Abaqus by Sherburn [48]. The model simulates irreversible hydrostatic crushing, material yielding, plastic flow, and damage evolution. The model has a non-linear pressure-volume relationship, a linear shear relationship (constant shear modulus, *G*), and includes a failure surface that is strain-rate dependent. As with most of the simplistic models for geomaterials, the present model separates the hydrostatic and deviatoric responses; they are uncoupled, so that no volumetric strain due to purely deviatoric loading may develop.

For the HJC, JHB/JH-1, and JH-2 models, the hydrostatic and deviatoric behaviors are decoupled and therefore independent from each other. As a result, the hydrostatic (pressure-volume relation) part of the model is a function of the first invariant of the stress tensor. The shear behavior is a function of the second invariant of the stress tensor. Therefore, a failure surface can be completely defined for a material by these two invariants only. However, it can be argued that the failure surface for rock-like materials (concrete) should be dependent on the third invariant of the stress tensor as well. To illustrate this point, Figure 4.1 shows that the ultimate compressive strength for a given pressure can be greater than the ultimate extension (tensile strength) at the same pressure. As can be seen, the failure surface is not symmetric in the octahedral plane (triaxial extension strength is less than the triaxial compression strength) and thus shows a dependence on the third invariant. This failure surface has a hydrostatic axis, $\xi = (\sigma_1 + \sigma_2 + \sigma_3)/\sqrt{3}$, θ is the Lode angle which is a function of the second and third invariants of the deviatoric stress tensor, and ρ_c and ρ_t are the maximum values of deviatoric stress components in compression and tension, respectively. This asymmetry has been ignored in the HJC-type models, which assume a circular failure surface in the octahedral plane, and therefore no dependence on the third invariant of the stress tensor. This difference is very elusive, and HJC-type models are traditionally satisfactory for simulating many projectile penetration events. However, when the cementitious targets are panels and are relatively thin (enough so that tensile spalling should occur prior to the projectile exiting the panel), or impact velocities become higher and therefore the expected exit velocities are also higher, this dependence on the third invariant becomes more pronounced. Any non-dependence on the third invariant would suggest that the material is just as strong in tension as it would be in compression at high confining pressures. This leads impact simulations to predict a stronger material in tension than it would be in practice, and therefore projectile exit velocities (in the case of thin panels) are consistently under predicted [12].

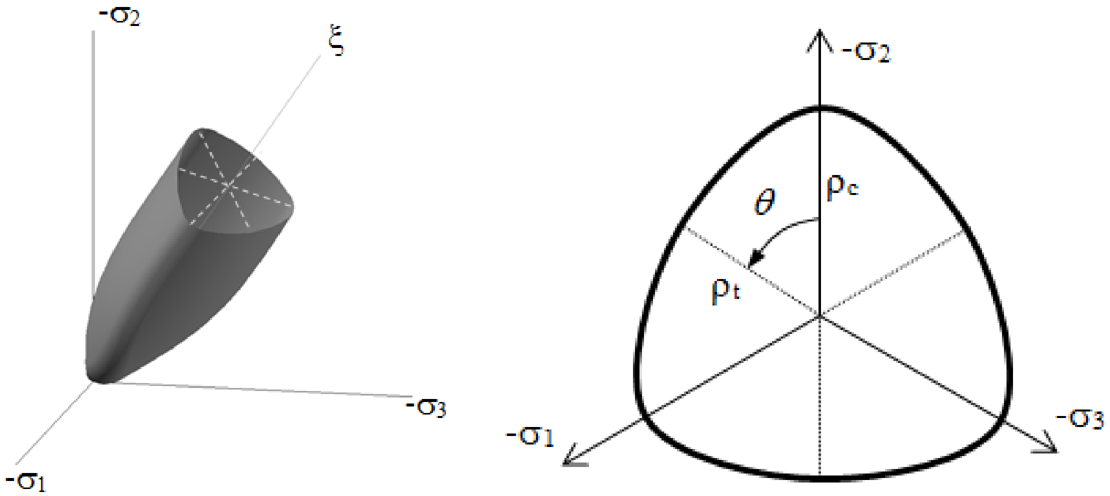

Figure 4.1 Hypothetical failure surface shape for constitutive model: (a) isometric view in 3D stress space (b) view in Π-plane

Outlined in the following sections are the same three principal components of the failure surface utilized in the previous models: (1) an equation of state (EOS) for the pressure-volume relation that includes the nonlinear effects of compaction, (2) a representation of the deviatoric strength of the intact and fractured material in the form of a pressure- and strain-rate-dependent yield surface, and (3) a damage model that transitions the material from the intact state to the fractured state.

4.2 Pressure – Equation of State

First the pressure-volume behavior of the model is described, which includes a non-linear bulk modulus and irreversible volumetric crushing that contributes to material damage. Specifically, the compressive behavior can be separated into three distinct regions: (1) an initial elastic zone, followed by (2) an irreversible crushing response where air voids begin to be collapsed, and finally (3) an elastic locking region corresponding to a fully dense material where all of the air voids have been crushed out. In this model initial loading, unloading, and reloading are treated differently. An illustration of the resulting pressure-volume behavior can be seen in Figure 4.2.

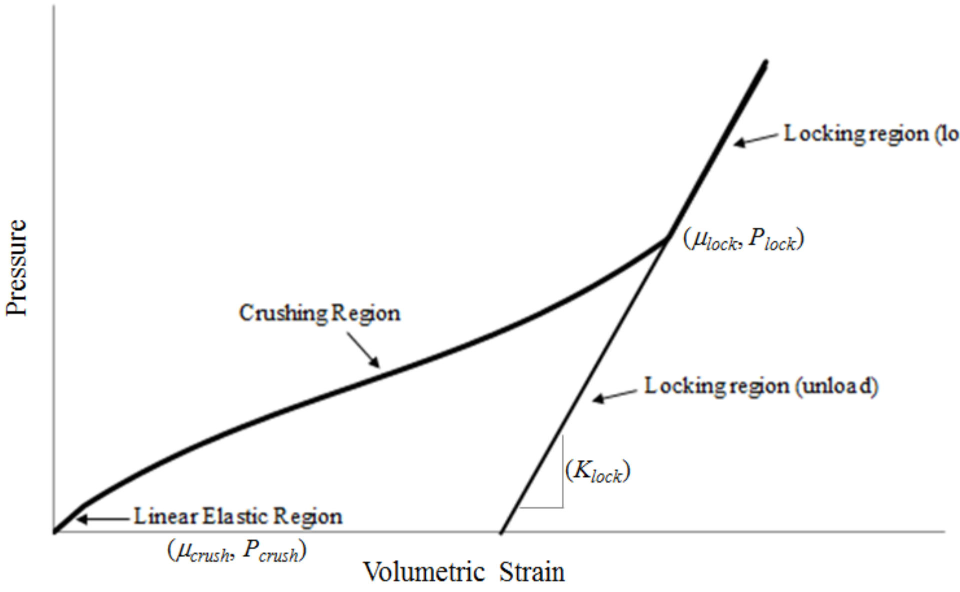

Figure 4.2 Pressure-volume relation model

The initial elastic zone for the model can only occur for volumetric strains below the crushing volumetric strain, μ_{crush}. Initial loading, unloading, and reloading in the elastic zone all follow a linear-elastic behavior defined by the elastic bulk modulus, $K_e = P_{crush} / \mu_{crush}$, where P_{crush} is the maximum attainable pressure for the initial elastic zone.

The irreversible crushing response occurs when the volumetric strain exceeds the crushing volumetric strain, μ_{crush}, but has not yet exceeded the locking volumetric strain value, μ_{lock}. The crushing region is defined by letting the origin of the crushing response coincide with the point in pressure-volume space that is the end of the initial elastic zone $\left(\mu_{crush}, P_{crush}\right)$. The crushing region is characterized by permanent volumetric compaction and follows the third-order polynomial equation

$$P = K_1\mu + K_2\mu^2 + K_3\mu^3 \tag{4.1}$$

where K_1, K_2, and K_3 are material constants, *P* is the mean normal stress (pressure), and μ is the measure of volumetric strain that is equal to the ratio of the difference of the initial and current volume to the current volume. In this equation, soil mechanics sign convention is used (compression > 0, tension < 0), which means that *P* as computed by Eq. (4.1) is equal to the first invariant of the stress tensor, I_1, multiplied by -1 $\left(I_1 = -P\right)$ In the crushing region, unloading and reloading are non-linear with the bulk modulus varying linearly between K_e and K_{lock} as μ varies between μ_{crush} and μ_{lock}. However, it should be noted that since the change in μ during a typical unload-reload cycle in the crush zone is generally only a small percentage of the value of $\mu_{lock} - \mu_{crush}$, the response is nearly linear in most cases.

Finally the linear elastic locking region in the model is defined by a locking bulk modulus, K_{lock}, and occurs for volumetric strain above the locking value of volumetric strain, μ_{lock}. Unloading and reloading in the locking region are purely linear elastic and also follow the locking bulk modulus, K_{lock}.

4.3 Strength – Failure Surface

Now the shear behavior of the model is described, which includes plastic flow, material yielding, and damage initiation and evolution. Engineering mechanics sign convention is used here, where the mean normal stress values less than zero denote compression. The yield surface is represented by two equations, depending on whether the state of stress is in compression (Eq. (4.2)) or tension (Eq. (4.3))

$$\sigma_{\max} = \left(C_1 - \left(C_2 + \left(C_1 - C_2\right)D\right)e^{A_n I_1} - C_4 I_1\right) \tag{4.2}$$

$$\sigma_{\max} = \left(C_1 - \left(C_2 + \left(C_1 - C_2\right)D\right)\right)\left(T_{\max} - I_1\right)/T_{\max}, \tag{4.3}$$

where C_1, C_2, C_4, and A_n are constants that are greater than or equal to zero, *D* is the scalar damage parameter that varies between 0 (intact) and 1 (damaged), $\dot{\varepsilon}$ is the strain rate, $T_{\max}$ is the maximum allowable tensile pressure, and the value of $\sigma_{\max}$ is restricted to values that are greater than or equal to zero.

The third invariant dependence of the failure surface is computed using the Lode angle, θ [8]. If the state of stress is tensile, then the failure surface value is computed using Eq. (4.3). In that case, the Lode factor, which is a function of the third invariant of the deviatoric stress tensor, is computed independently. More specifically, the Lode angle, θ, is first computed and subsequently the Lode angle factor is computed by evaluating the William-Warnke Lode function [11]. Using the cylindrical coordinate system of the Haigh-Westergaard representation of the William-Warnke yield criterion, the failure surface is a function $f\left(\xi, \rho, \theta\right)$, where ξ is the hydrostatic axis, $I_1/\sqrt{3}$, ρ is the cylindrical radius, $\sqrt{2J_2}$, and θ is the Lode angle, which is dependent on second and third invariants of the deviatoric stress tensor as

$$\theta = \frac{1}{3}\cos^{-1}\left(\frac{3\sqrt{3}}{2}\frac{J_3}{J_2^{3/2}}\right) \tag{4.4}$$

where J_2 and J_3 are the second and third invariants of the deviatoric part of the stress tensor, respectively, and they are defined as

$$J_2 = \tfrac{1}{2}\left(S_x^2 + S_y^2 + S_z^2 + 2S_{xy}^2 + 2S_{yz}^2 + 2S_{xz}^2\right) \tag{4.5}$$

$$J_3 = \tfrac{1}{3}\left(S_x^3 + S_y^3 + S_z^3 + 3S_xS_{xy}^2 + 3S_xS_{xz}^2 + 3S_yS_{xy}^2 + 3S_yS_{yz}^2 + 3S_zS_{xz}^2 + 3S_zS_{yz}^2 + 6S_{xy}S_{yz}S_{xz}\right) \tag{4.6}$$

where S_x, S_y, S_z, S_{xy}, S_{yz}, and S_{xz} are the components of the deviatoric stress tensor [12]. Once the Lode angle is calculated, the Lode angle factor is used to calculate a new reduced failure surface. The William-Warnke Lode function is defined as

$$\sigma_{reduced} = \sigma\left(\frac{4\left(1-\beta^2\right)\cos^2\left(\frac{\pi}{6}+\theta\right)+\left(2\beta-1\right)^2}{2\left(1-\beta^2\right)\cos\left(\frac{\pi}{6}+\theta\right)+\left(2\beta-1\right)\sqrt{4\left(1-\beta^2\right)\cos^2\left(\frac{\pi}{6}+\theta\right)+5\beta^2-4\beta}}\right) \tag{4.7}$$

where σ is the strength or failure surface in compression, and β is a material property that describes the strength ratio between triaxial tension and triaxial compression. Figure 4.3 shows the William-Warnke Lode function in the octahedral plane for different values of β. For β equal to 1.0, the function is symmetric and circular in the octahedral plane, and the value of the Lode angle as determined by J_2 and J_3 is not important. However, when β is 0.7, the function takes a form that becomes asymmetric in the octahedral plane and is 70% less along the tension axis as compared with the compression axis. Therefore, Eq. (4.7) explicitly determines the reduced strength that will be seen in the modified material behavior [12].

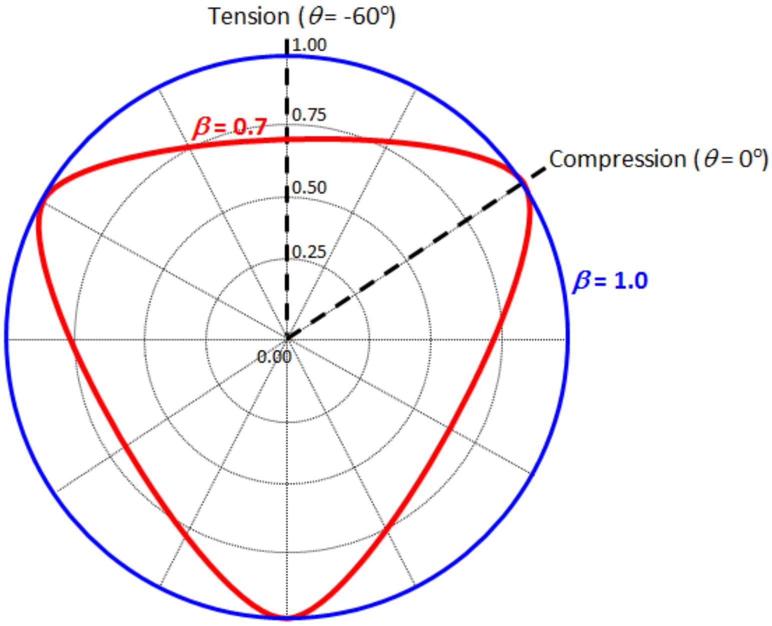

Figure 4.3 William-Warnke Lode function for two different values of β as defined by Eq. (4.7)

4.4 Damage Criterion

This model also accounts for material damage that develops incrementally during the course of stress loading histories. This characterization of material damage effectively leads to a reduced failure surface resulting from excessive plastic shear strain as well as hydrostatic crushing (plastic volumetric strain). Damage due to plastic volumetric strain is included because concrete tends to be depleted of its cohesive strength during the progressive collapse of air voids, though under most circumstances, majority of damage results from equivalent plastic strain [17]. Though there are several modes of fracture and failure of concrete under quasi-static loads, it is recognized that the primary cause of damage in high-velocity impact is dues to pressures (both compressive and tensile) that are orders of magnitude higher than the inherent strength of the material. These pressures result from localized direct impact of the fast-moving projectile or from the faster-moving shock front undergoing expansion, reflection, and magnification as it traverses the target. It is for this very reason that the value of material damage is quantified by a scalar damage parameter, *D*, which is essentially defined as

$$D = \sum \left(\frac{\Delta \varepsilon_p}{\varepsilon^f} + \frac{\Delta \mu_p}{\mu^f} \right) \tag{4.8}$$

where $\Delta\varepsilon_p$ is an increment in the effective deviatoric plastic strain, $\Delta\mu_p$ is an increment of volumetric plastic strain, ε^f is the equivalent deviatoric strain to fracture, and μ^f is the equivalent volumetric strain to fracture (under the current conditions of strain rate, temperature, pressure and equivalent stress). Fracture is then allowed to propagate when *D* = 1. By plotting ε^f as a function of mean normal stress, a linear trend was observed. This led to the relationship $\varepsilon^f = I_1 D_1$, where D_1 is a constant greater than zero. Since, as per standard notations, compressive stress is negative, the relationship becomes $\varepsilon^f = -I_1 D_1$. Again, the majority of damage is accrued from effective deviatoric plastic strain, but some damage will also accumulate from plastic volumetric strain. Radial strain measurements made from UXC tests showed that noticeable plastic volumetric strain can accumulate up to 50% above the locking volumetric strain, μ_{lock}. Therefore the scalar damage parameter can be re-expressed as

$$D = \sum\left(\frac{\Delta\varepsilon_p}{-I_1 D_1} + \frac{\Delta\mu_p}{1.5\mu_{lock}}\right). \tag{4.9}$$

Here, values of $\left(-I_1 D_1\right)$ are restricted to values greater than 0.01 and μ_{lock} is the locking volumetric strain described in section 4.2. The damage parameter, *D*, is also included in the failure surfaces for Eqs. (4.2) and (4.3), and is specifically needed at low pressures with the material showing brittle behavior. At extremely high pressures, however, the material behaves in a more ductile fashion and, as expected, inclusion of the effects of damage is practically unnoticeable [12]. Since damage values that are greater than or equal to one are assumed to correspond to a fully damaged material, and Eqs. (4.2) and (4.3) require that damage values be less than or equal to one, the computed values of *D* are simply reset to a value of one if this value is exceeded. Eq. (4.9) suggests a linear transition from undamaged (*D* = 0) to damaged (*D* = 1) material. Previous material models have had a nonlinear dependence, usually by means of an exponent constant. The experimental results for the materials discussed here do not show a distinctly nonlinear trend, so this relationship between effective plastic strain and mean normal stress should be sufficient.

4.5 Strain-Rate Law

The original AFC model proposed a generic Johnson-Cook strain-rate law in the failure surface, but it has been shown that many materials, including brittle materials like concrete and ceramics, show nonlinear behavior in the logarithmic scale of the strain rate [44], [45]. For this reason, the adaption of the Huh-Kang strain-rate law in the equation below provides a significant improvement with no significant decrease in computational efficiency [19]

$$\left(1 + C_3 Ln(\dot{\varepsilon}) + C_{11} Ln(\dot{\varepsilon})^2\right) \tag{4.10}$$

where C_3 and C_{11} are non-zero constants and $\dot{\varepsilon}$ is the strain rate. This strain rate law is used as a dynamic increase factor, multiplied by the failure surface (both compressive and tensile).

Chapter 5

Parametric Identification

5.1 Introduction

The constitutive model proposed in Chapter 4 was implemented within the commercial finite element software program Abaqus, specifically as a dynamic user-defined material model (VUMAT). The relationships outlined in Sections 4.2, 4.3, 4.4, and 4.5 were programmed as a FORTRAN code to be called upon by Abaqus during a simulation of an UHSC material under high-rate, high-pressure loading. This chapter deals with the problem of characterization of the material constants in these equations. In many studies that use the HJC, JHB/JH-1, and JH-2 type material models, the investigators would always use material constants from the original publications by Holmquist, Johnson, and coauthors, irrespective of the material used. This was done because high-fidelity material characterization experiments are difficult, extremely costly and time consuming. Even some of the experimental data used in the original papers proposing these models was previously used by other authors [17]. It has also been observed that in cases where simulations did not match experiments exactly, iterative adjustments to the material constants were purposely made to achieve the desired accuracy in the , supposedly, predicted results. In the present study, raw data of high-fidelity material characterization experiments was used exclusively to determine the appropriate material constants for the model described previously and no further adjustments were made to modify the predictions. A flow diagram of the VUMAT processes used is given in Figure 5.1 below.

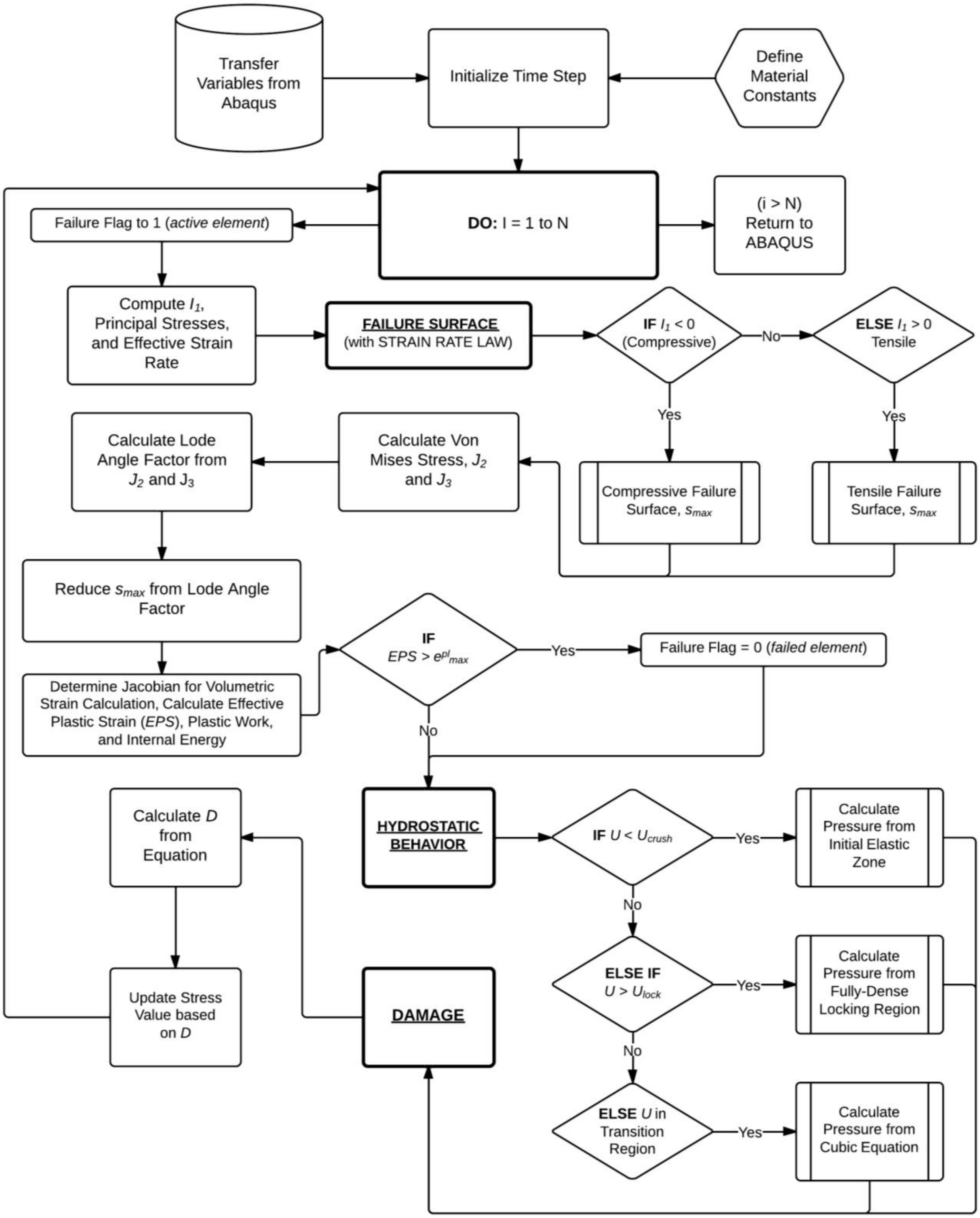

Figure 5.1 Flow chart of VUMAT used for impact and blast simulations

5.2 Optimization of Model Material Parameters

This problem can be cast in the form of a constrained optimization problem. Explicitly, a fitting algorithm was developed that was used to minimize the sum of the deviations squared from a given set of experimental data, taking the form

$$\Pi = d_1^2 + d_2^2 + \ldots + d_n^2 = \sum_{i=1}^{n} d_i^2 = \sum_{i=1}^{n} \left[y_i - f\left(x_i\right) \right]^2 \tag{5.1}$$

where d_i is the deviation (or error) from each data point, (*x*,*y*), *x* is the independent variable, *y* is the dependent variable, and *f(x)* is the fitting curve. The constitutive material model equations were fitted using actual laboratory material property data for two baseline UHSC's. These materials will be referred to as UHSC-1 and Ashcrete, representing two rapid-set, high-strength cementitious composites. The mechanical property tests included hydrostatic compression (HC), unconfined compression (UC), triaxial compression (TXC), unconfined direct tension (DT), uniaxial compressive strain (UXC), Kolsky Bar (KB), and uniaxial strain load/constant volume strain loading tests [52] These difficult tests were specifically undertaken by a researcher colleague and fellow doctoral student (William F. Heard) for use in the simulations like the ones presented herein.

The first part of the VUMAT deals with defining the failure meridian in both compression and tension, as outlined in Eqs. (4.2) and (4.3). To find these constants, the experimental data for TXC, UC, and KB must be fitted by these equations. TXC experimental results for UHSC-1 are shown in Figure 5.2. Each curve shown represents a different confining pressure, from 10-300 MPa. For the failure surfaces, the peak value of each curve in Figure 5.2 corresponds to a data point on the failure surface. The relationships between mean normal stress (*p*), principal stress difference (*q*), axial stress (σ_1) and radial stress (σ_3) are given in Eqs. (3.35) and (3.36). The parameters $C_1, C_2, C_3, C_4, C_{11}$, and A_n are optimized to fit this data using the relationship of Eq. (5.1). TXC experimental results for Ashcrete are shown in Figure 5.3. Each curve shown represents a different confining pressure, from 25-300 MPa. Figure 5.4 shows the experimental and the simulation data for the UHSC-1 failure surface. Figure 5.5 shows the experimental and the simulation data for the Ashcrete failure surface. The experimental data in Figure 5.4 and Figure 5.5 show two data point clusters because two experiments were conducted for each confining pressure. Only one curve is shown for each confining pressure in Figure 5.4 and Figure 5.5 to make it easier to comprehend the changes in behavior. There is also one additional set of data points in both figures. These are the first set of data points nearest to the origin representing the UC test data when no confinement was used. The DT test must also be done to determine $T_{\max}$, which is used in the tensile part of the failure surface described in Eq. (4.3).

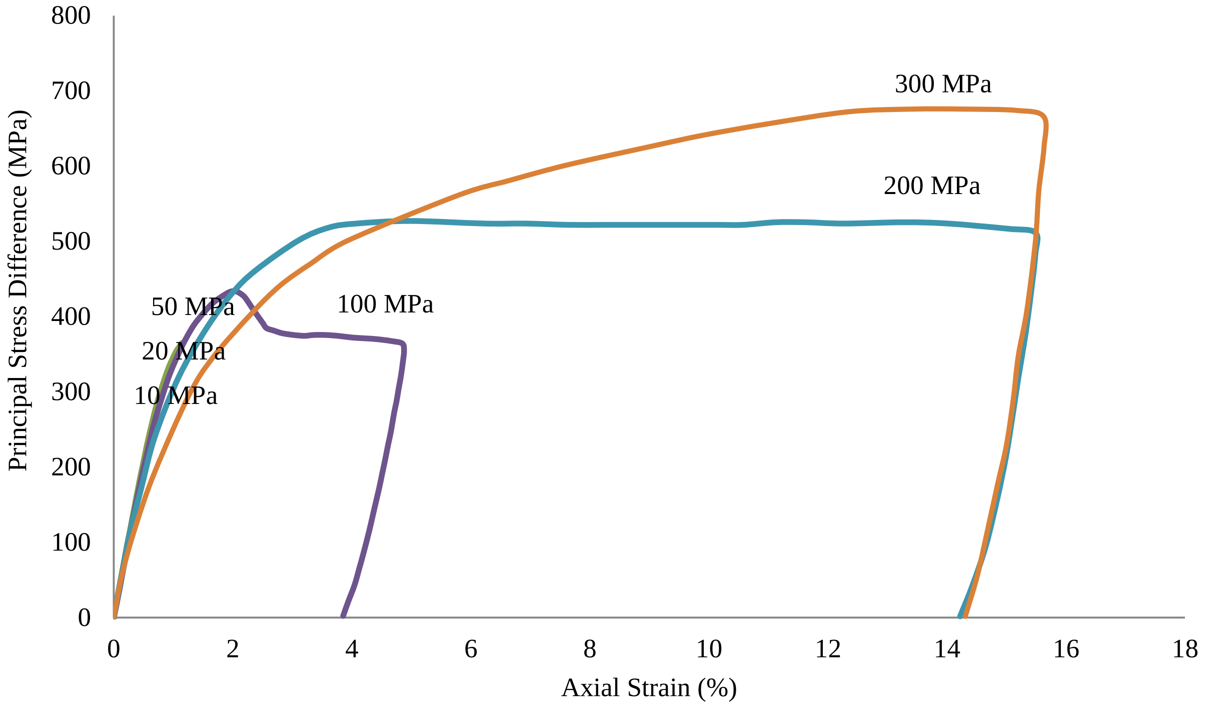

Figure 5.2 TXC Experimental Data for UHSC-1

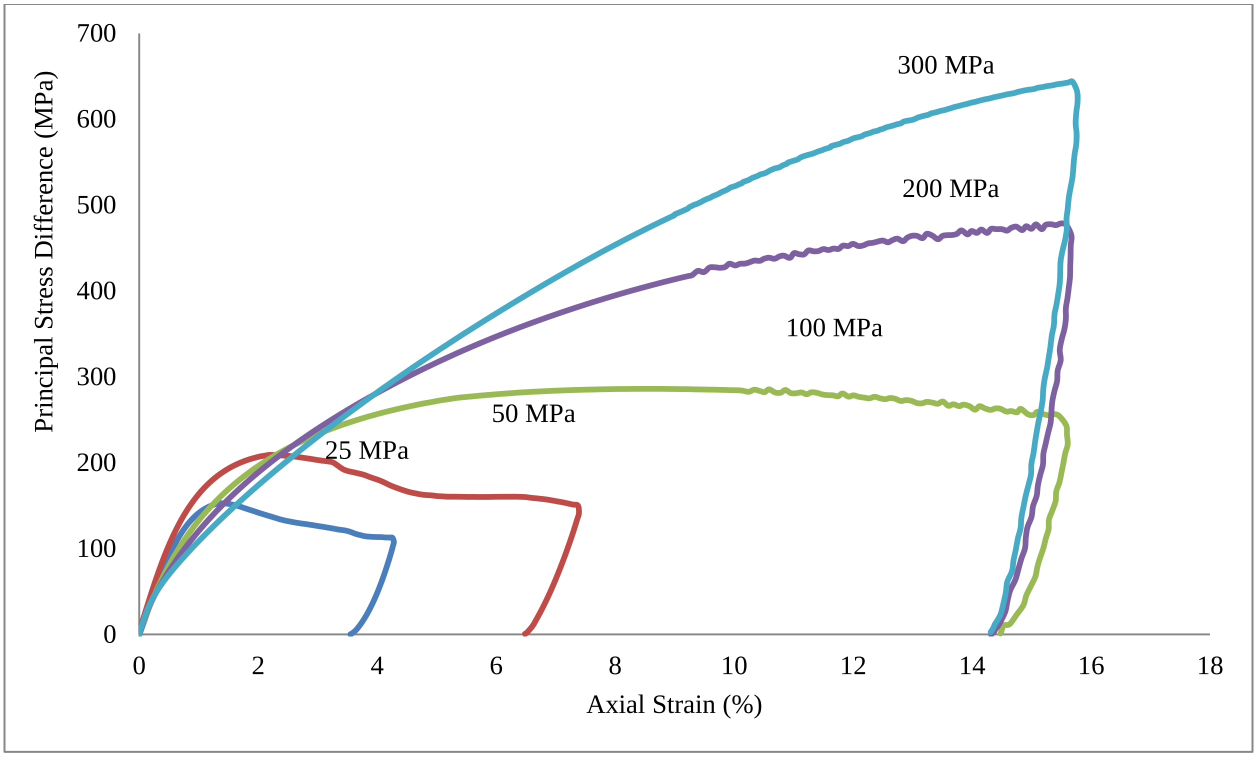

Figure 5.3 TXC Experimental Data for Ashcrete

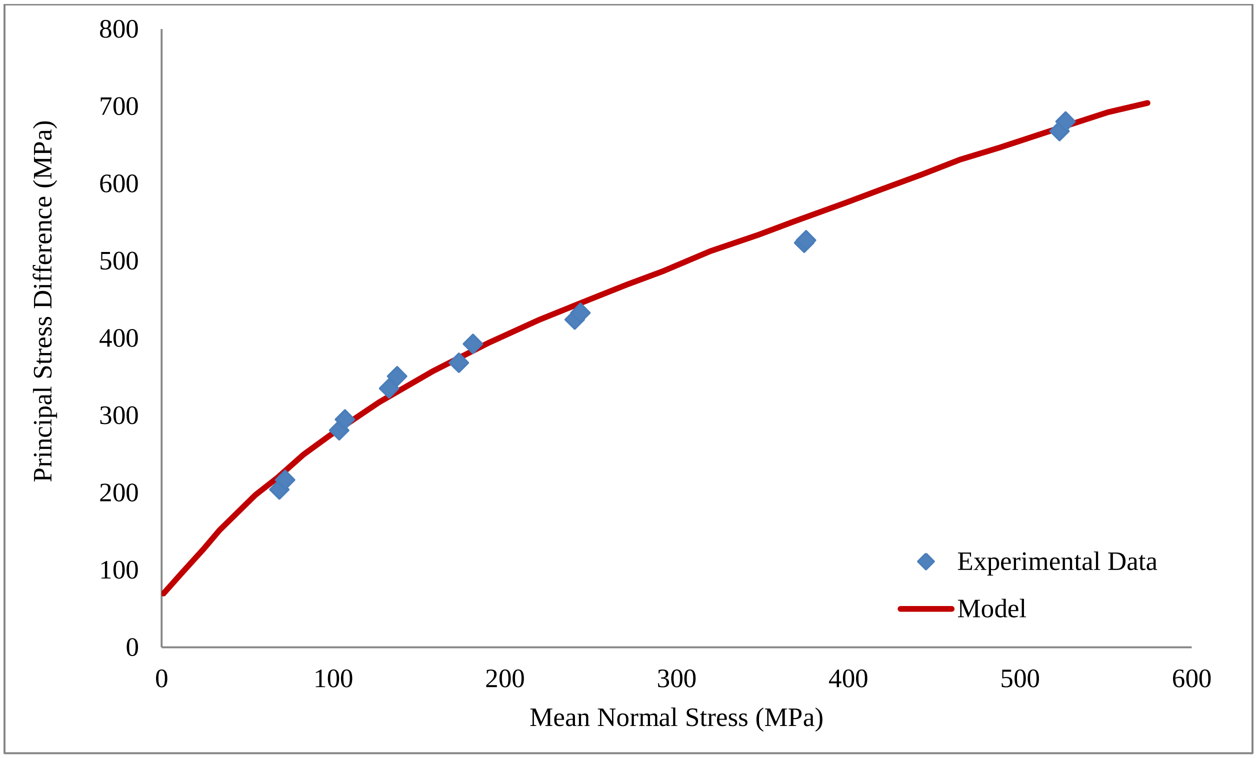

Figure 5.4 Failure Surface for UHSC-1

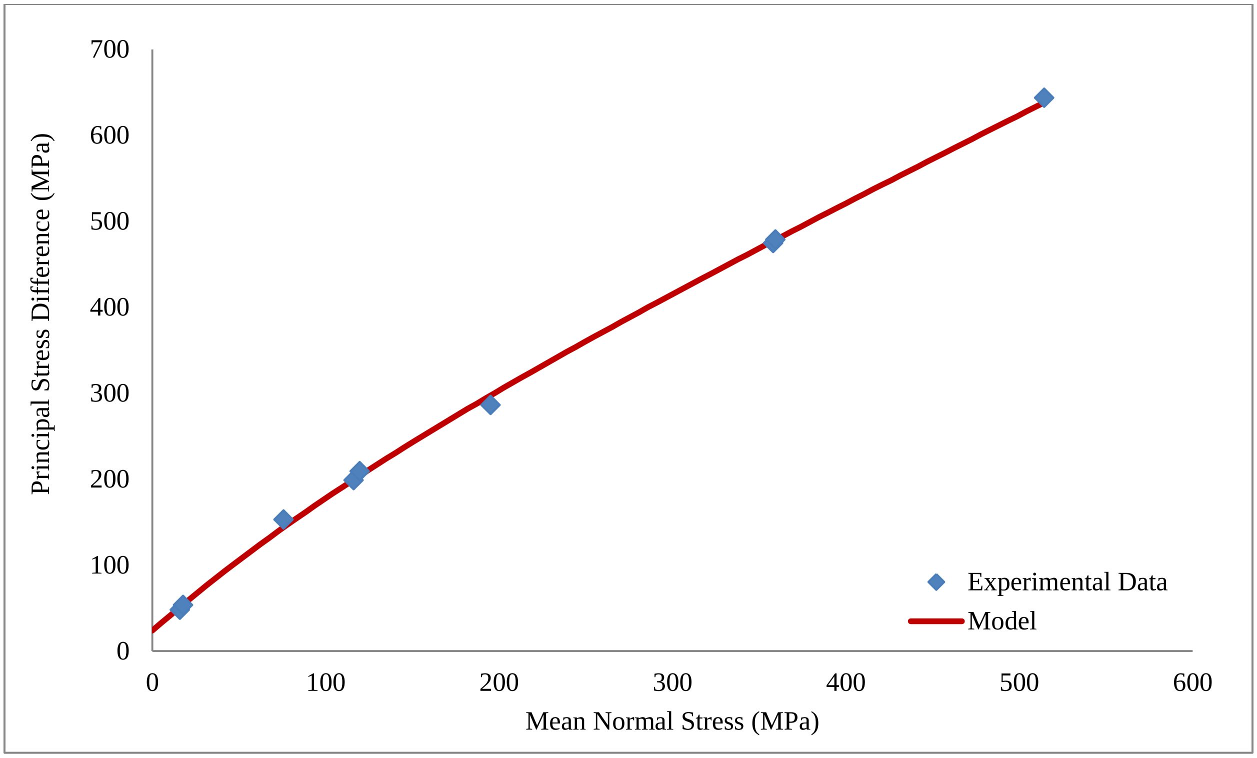

Figure 5.5 Failure Surface for Ashcrete

Next, the VUMAT must compute the pressure at each material point. To do this, the parameters $K_1, K_2,$ and K_3 must be optimized for Eq. (4.1) to fit the experimental data from the HC and UXC tests. Figure 5.6 shows the experimental data for UHSC-1 and Figure 5.7 shows the experimental data for Ashcrete. Furthermore, the model parameters μ_{crush} and P_{crush} are determined directly from the experimental data to define the end of the linear elastic region of the model and the beginning of the crushing region. Finally, the model parameters μ_{lock}, P_{lock} and K_{lock} are determined directly from the experimental data to define the final locking phase of the fully dense material. For the UXC, a cylindrical specimen was loaded in compression while maintaining zero radial strain. In the experiment, once the material reached the peak locking pressure, P_{lock}, the specimen was unloaded to determine the locking modulus, K_{lock}.

In previous constitutive models, some authors use HC tests to define the pressure-volume relation. Because HC tests simply increase radial pressure at the same level as the axial pressure, this still allows some amount of radial expansion, whereas in the UXC test the radial pressure is increased to allow no radial expansion. This leads to higher states of pressure in the UXC tests than the HC tests. This is a critical distinction that previous researchers failed to identify [18], [23]. This is important because in characterizing the behavior of brittle material during an impact event, it should be apparent that there is no time for radial expansion of the material to take place directly in front of the projectile's path. The material in the direct vicinity of the footprint of impacting projectile should be simulated using material constants calibrated from UXC tests. This difference is illustrated in Figure 2.5 and Figure 2.6. It is immediately apparent that the nonlinear behavior of the material under uniaxial strain is stronger than the hydrostatic behavior. However, this is not necessarily the case in regions of the material not in close vicinity of the projectile footprint. This brings up the possibility of partitioning the model such that the material near the point of impact and in front of the projectile path is modeled using UXC parameters and the material everywhere else modeled using HC data. This leads to many problems involving selecting the partition location and associated stress-state jumps at the interfaces that are not yet fully tractable. Therefore, only UXC data is used to define the pressure-volume relation since the local behavior of the target is considerably more important than the global behavior.

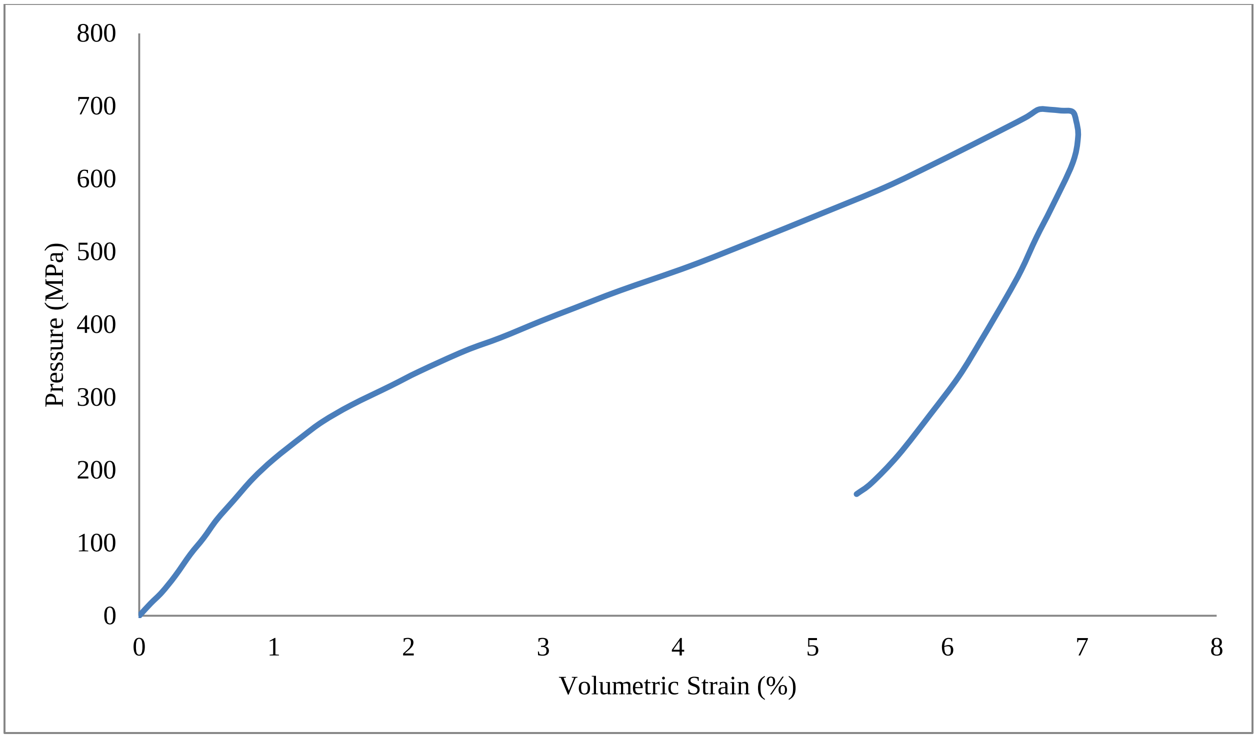

Figure 5.6 Experimental pressure-volume relation for UHSC-1 (UXC)

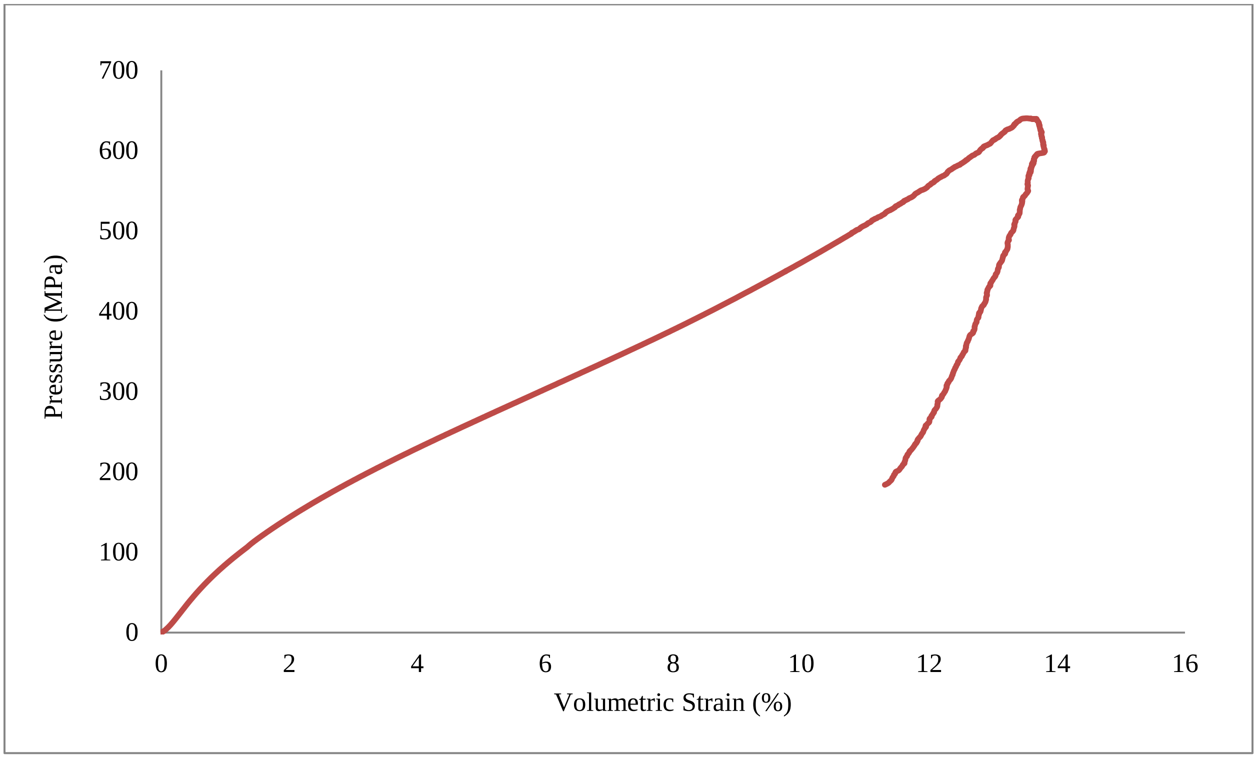

Figure 5.7 Experimental pressure-volume relation for Ashcrete (UXC)

Finally, for the damage portion of the VUMAT, the same data points used for the failure surface are converted to data points in terms of effective plastic strain as a function of mean normal stress. This data is used to find the parameter D_1 as seen in Eq. (4.8).

5.3 Determination of Parameters from Experimental Data

As discussed in the previous section, actual experimental data from UC, UXC, and TXC tests were used to determine the material constants for the constitutive model described in Chapter 4. Figure 5.4 and Figure 5.5 show the experimental data points from the UC and TXC tests and the model failure surface that fits the data. Basic parameters like mass density, ρ, and shear modulus, G, were determined at ERDC directly from basic calculations. The value of β was taken to be a typical value used from the literature [12]. A simple DT test was conducted to determine the maximum allowable tensile pressure, $T_{\max}$. For C_3 and C_{11}, Split-Hopkinson (Kolsky) Bar tests were conducted to determine the constants for strain-rate effect. To arrive at the rest of the parameters, a least-squares optimization algorithm implemented in MATLAB was used. As described previously, the three main components of the constitutive model are the pressure-volume relation, the failure surface, and the damage evolution.

For the pressure-volume relation, the experimental data for the first two material phases was input into the program; that is, all the data until the point $\left(\mu_{lock}, P_{lock}\right)$. Once input, the program prompts the user to define the end of the linear elastic region, $\left(\mu_{crush}, P_{crush}\right)$. This requires some discretion on the part of the user since some experimental data has a much more gradual transition from linear to non-linear behavior. Once this data point is known, the program redefines the data with the origin at $\left(\mu_{lock}, P_{lock}\right)$. Thereafter, Eq. (4.1) is fitted and the parameters $K_1, K_2,$ and K_3 are optimized. For the locking region (phase 3), the experimental data can simply be plotted by any graphing software and a linear trend-line fit of the data can be used, with the slope of the line representing K_{lock}. Figure 5.8 shows the MATLAB output of both the experimental input data and the model fit for Ashcrete. UHSC-1 shows a similar agreement. The units for pressure in Figure 5.8 are MPa.

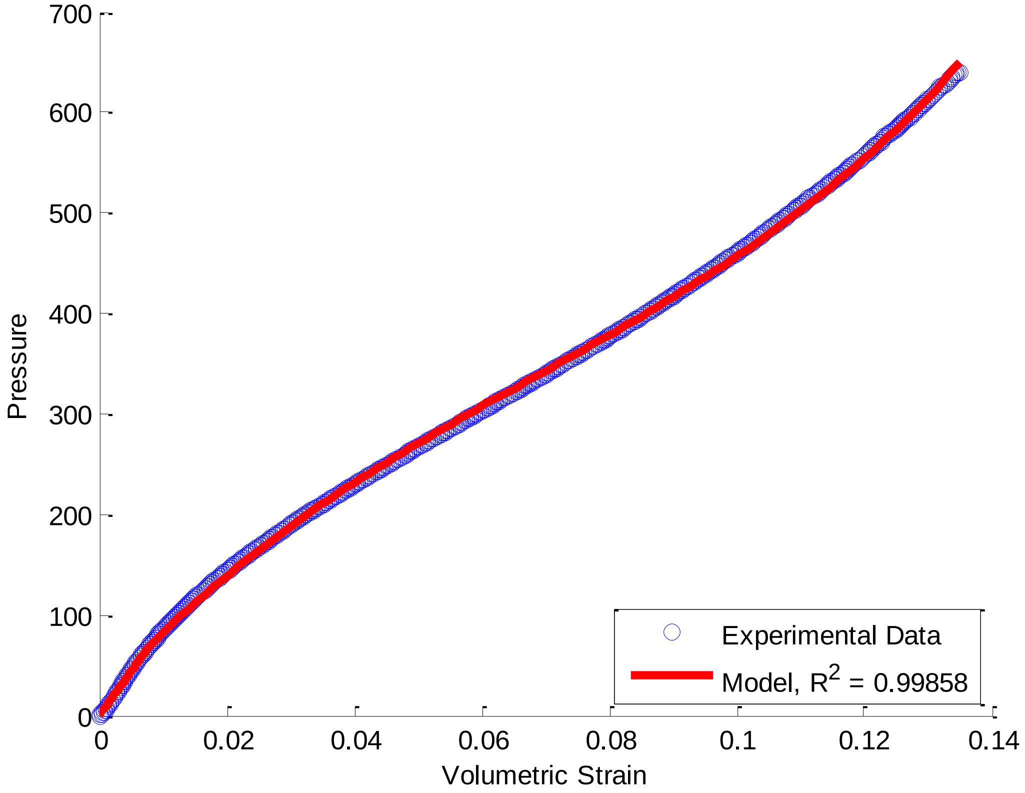

Figure 5.8 MATLAB output for optimized pressure-volume relation for Ashcrete

For the failure surface, the experimental data points shown in Figure 5.4 and Figure 5.5 are input into the program. Then, based on an initial guess for each constant as well as upper and lower bounds, the program optimizes C_1, C_2, C_4, and A_n from Eq. (4.2). Since the scalar damage parameter, *D*, appears in this equation, but is evaluated separately; it is assigned a value 0 during this optimization process. This corresponds to an undamaged material point. Figure 5.9 shows the MATLAB output of both the experimental input data and the model fit for Ashcrete. UHSC-1 shows similar agreement. The units for both mean normal stress and principal stress difference are MPa.

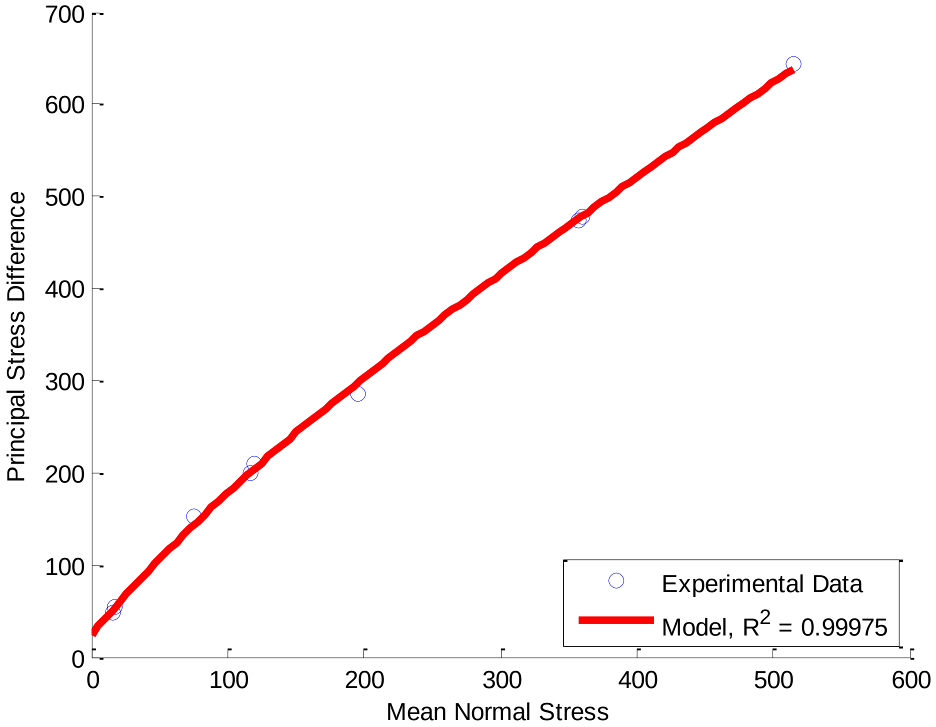

Figure 5.9 MATLAB output for optimized failure surface for Ashcrete

For the damage calculation, the experimental data points as shown in Figure 5.4 and Figure 5.5 are plotted in the form of effective plastic strain vs. mean normal stress. Since Eq. (4.8) suggests a linear relationship between the incremental effective plastic strain and mean normal stress, a simple linear fit is used to determine D_1. Figure 5.10 shows the MATLAB output of both the experimental input data and the model fit for Ashcrete. UHSC-1 shows a similar agreement. The units for mean normal stress are MPa.

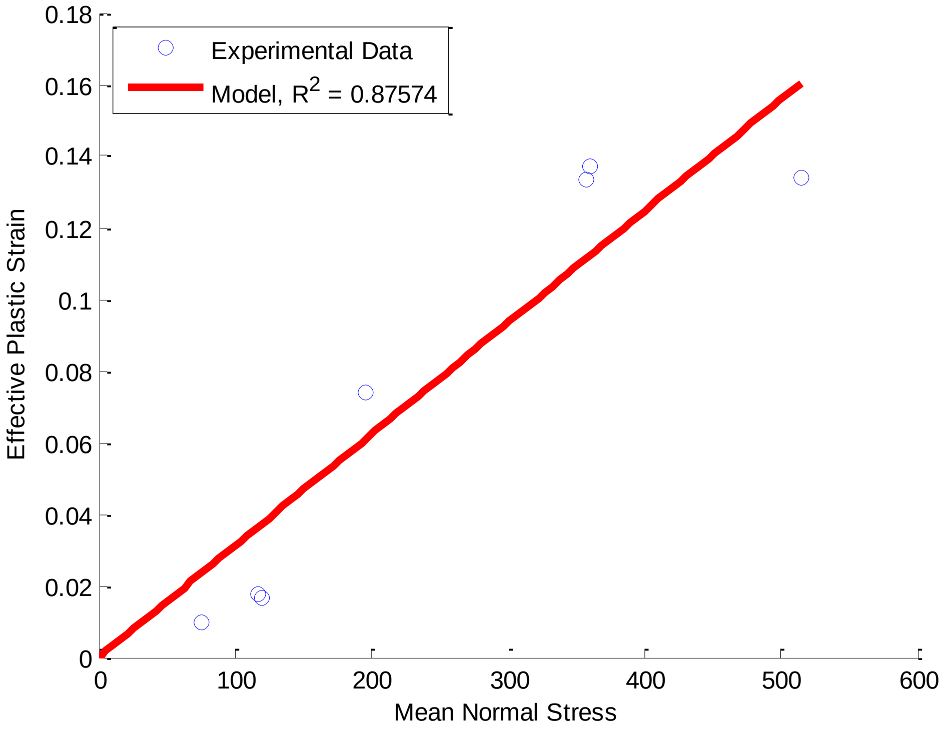

Figure 5.10 MATLAB output for optimized damage behavior for Ashcrete

For strain-rate behavior, very limited experimental data was available, so a mildly non-linear trend was used. The constants C_3 and C_{11} were iteratively determined from very simple, low fidelity calibration models. All the constants determined experimentally and/or from optimization for both UHSC-1 and Ashcrete are shown below in Table 5.1. For reference, the typical compressive strengths for these two UHSCs are 216 MPa for UHSC-1 and 103 MPa for Ashcrete. These values are not reported in Table 5.1 because these do not appear in the constitutive model.

To ensure proper implementation of these constants within the framework of a finite element program, several calibration models were made to reproduce the experimental data of TXC and UXC tests. This was done to determine if the internal algorithms within Abaqus could appropriately apply the model as a VUMAT. Since the material model was written for dynamic problems only, the TXC and UXC models also used the transient modeling option. To eliminate the issues related to inertial or other dynamic effects, the loading rate was kept low.

Table 5.1 Material constants for UHSC-1 and Ashcrete

Variable	Description	UHSC-1	Ashcrete	Units
ρ	Density	2.5557E-09	2.2763E-09	Tonne/mm^3
G	Shear Modulus	18,457	18,457	MPa
C_1	Failure Surface Constant	1,016.30	125.85	MPa
C_2	Failure Surface Constant	908.65	102.00	MPa
C_3	Strain Rate Law Constant	0.01209	0.01209	
C_4	Failure Surface Constant	0.10382	1.0	
C_{11}	Strain Rate Law Constant	-0.0006275	-0.0006275	
A_n	Failure Surface Constant	0.0017345	0.00754125	
T_{max}	Maximum Allowable Tensile Pressure	6.8946	4.3780	MPa
P_{lock}	Equation of State Constant	792.88	640.46	MPa
μ_{lock}	Damage Constant	0.10094	0.13814	
K_{lock}	Equation of State Constant	45039	18364	MPa
P_{crush}	Equation of State Constant	172.37	60.60	MPa
μ_{crush}	Equation of State Constant	0.00781	0.00683811	
K_1	Equation of State Constant	7,919.2	6,429.9	MPa
K_2	Equation of State Constant	-29,206	-47,138.6	MPa
K_3	Equation of State Constant	187,100	255,724.2	MPa
D_1	Damage Constant	0.00040598	0.000311742	
β	Extension Failure Surface Constant	0.625	0.625	
ε_{pl}^{max}	Maximum Effective Plastic Strain	2.5	2.5	

Both the TXC and UXC models used the same parts and mesh and only the radial boundary conditions were changed between them. To reduce computation time, two-way symmetry was also utilized. A simple description of the loading scenarios is shown in Figure 3.4(a). For the TXC model, a displacement-controlled boundary condition was applied in place of $-\sigma_3$. This replicated the actual loading process of the experiments most closely. For the UXC models, a radial displacement boundary condition ($u_r = 0$) was used on the outer curved surface in place of $-\sigma_1$ and $-\sigma_2$ to ensure the purely uniaxial strain condition. Conversely, for TXC models, a constant, uniform pressure load on the radial surface to replicate the confining pressure of the triaxial experiments ($-\sigma_1 = -\sigma_2 = -\sigma_3$) was used. In both models, a low-fidelity mesh with 1189 linear hexahedral elements (type C3D8R) was used, by applying the sweep technique and the medial axis meshing algorithm. Figure 5.11 shows the model assembly and mesh used for both UXC and TXC models.

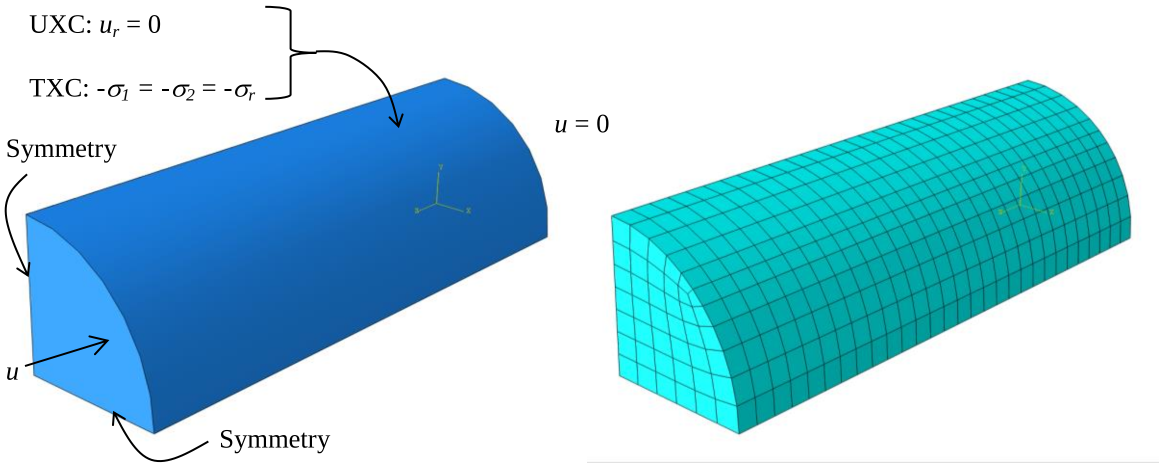

Figure 5.11 UXC and TXC model assembly (left) and mesh (right)

For the pressure-volume relation calibration model (UXC), a peak pressure load corresponding to over 1000 MPa was used to ensure that the specimen went through all the three regions, as shown in Figure 4.2. The results of this calibration model for Ashcrete are shown in Figure 5.12 giving excellent agreement with the experimental data. The UHSC-1 calibration model showed similar agreement. In the actual experiment, once the material reached the peak locking pressure, P_{lock}, the specimen was unloaded to determine the locking modulus, K_{lock}. The calibration model was loaded beyond this point to see if the fully-dense region followed the same slope, which it did very well.

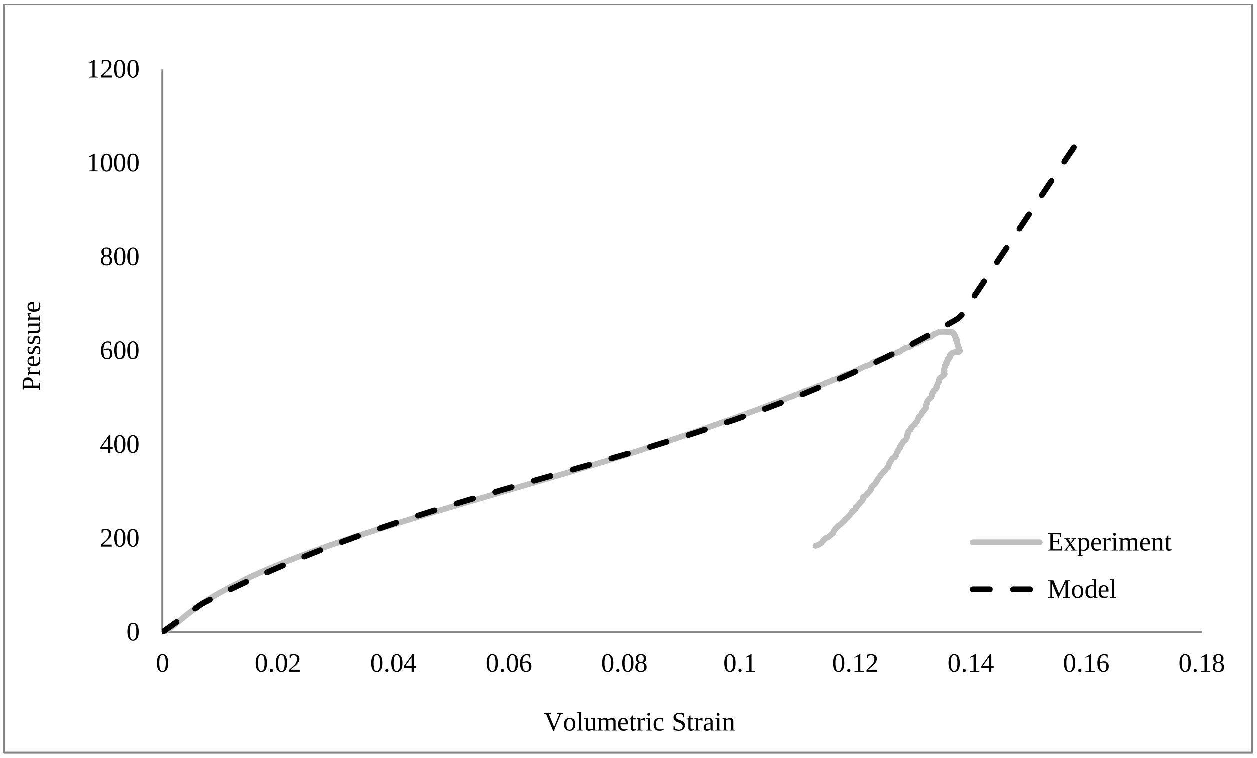

Figure 5.12 Pressure-volume relation from calibration model of Ashcrete

For the failure surface calibration model (TXC), two confining pressures were chosen to verify the appropriate failure points: 50 MPa and 200 MPa. Figure 5.13 and Figure 5.14 show the principal stress difference as a function of the axial strain for two TXC experiments and one calibration model corresponding to the corresponding level of confining pressure. The calculated peak values were then converted to points on the failure surface. These peak values are plotted against the experimental failure surface points and compared in Figure 5.15. The calculated peak values showed excellent agreement, however the corresponding volumetric strain for these points only showed fair agreement. This distinction is made more apparent at higher levels of confinement. This is a common trait in failure surface models when simulating brittle materials [3].

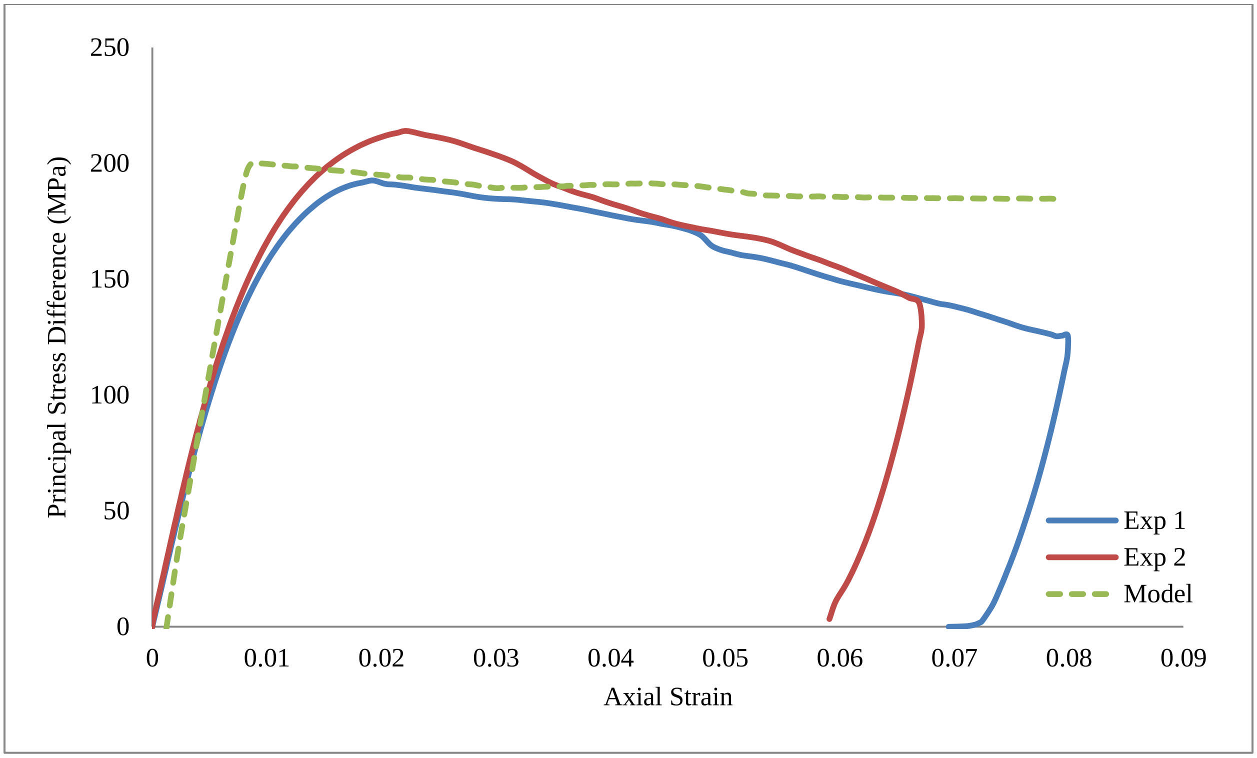

Figure 5.13 TXC calibration model and two experiments for Ashcrete (50 MPa confinement)

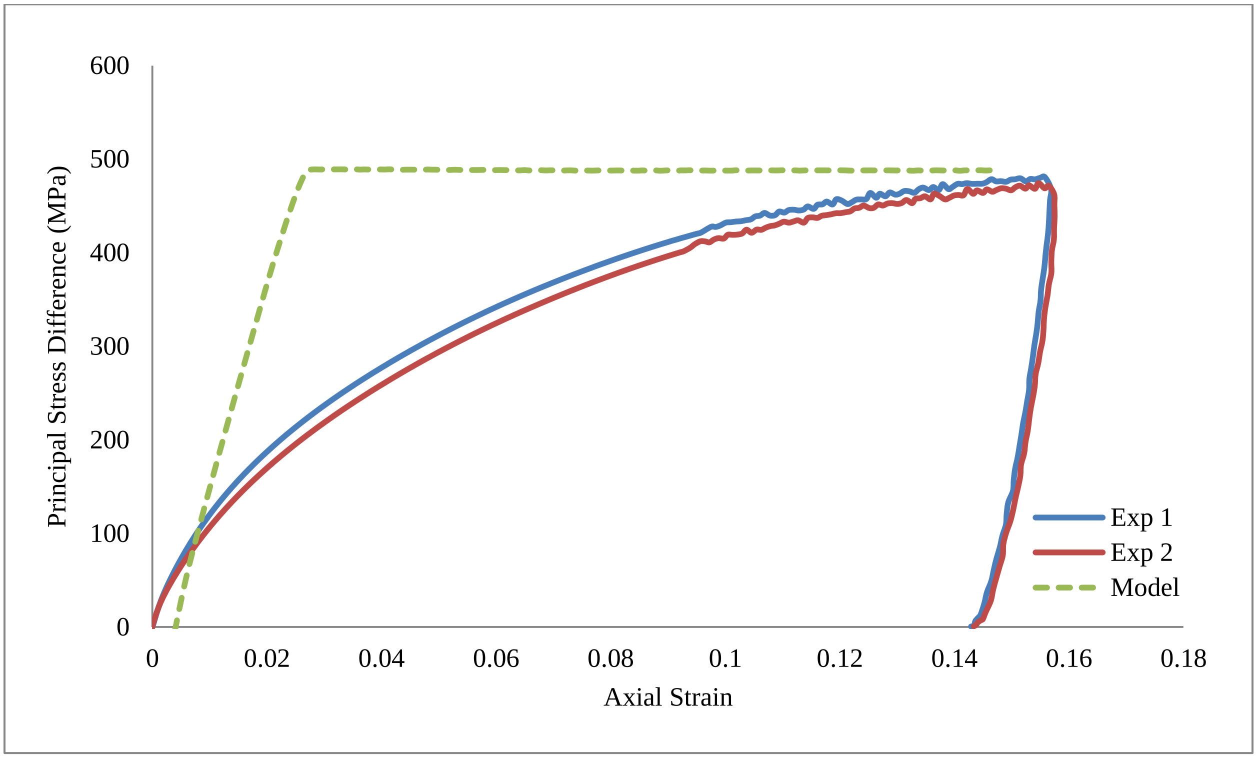

Figure 5.14 TXC calibration model and two experiments for Ashcrete (200 MPa confinement)

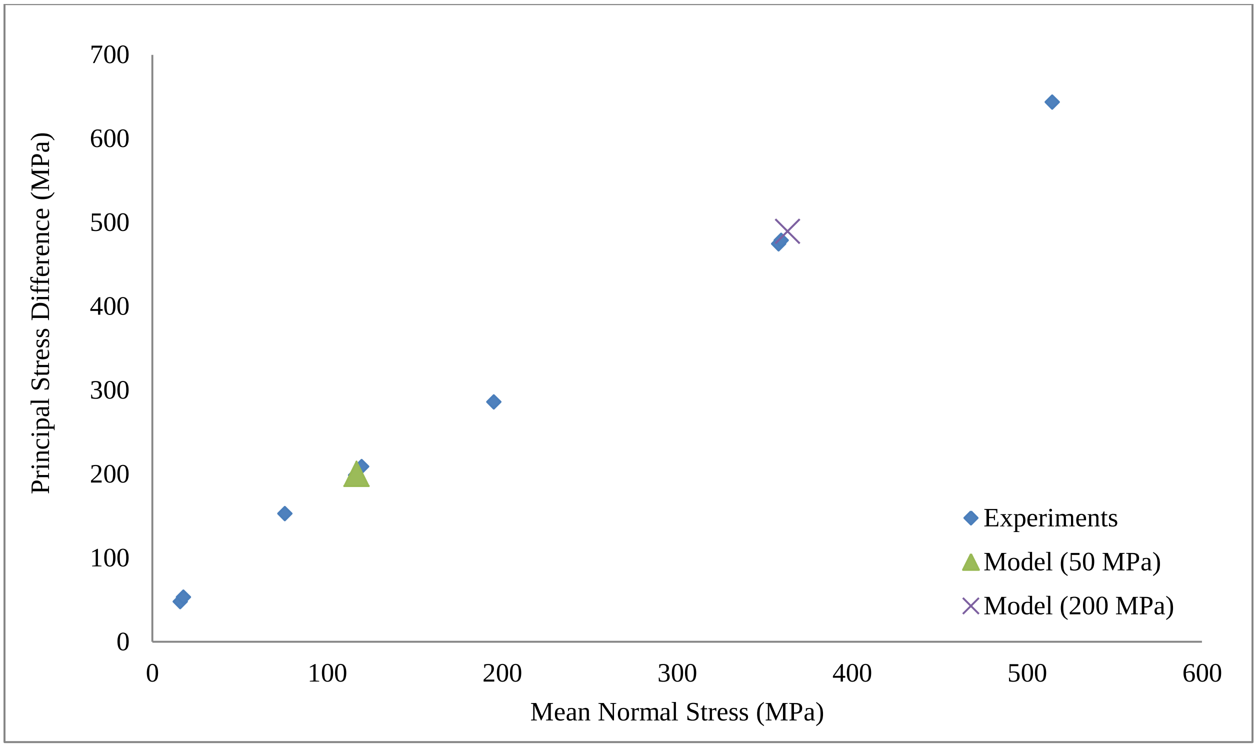

Figure 5.15 Experimental failure surface and calibration model for ASHCRETE

Given the calibration model results shown in the above figures, the material constants determined from the optimization algorithm developed are considered as suitable for simulating the behavior of UHSC-1 and Ashcrete and all simulations presented in Chapter 7 use these constants.

Chapter 6

Modeling & Simulation Strategies

6.1 Introduction

Static and quasi-static models have successfully been used to simulate micro- and macro-mechanics structural analysis. But for the majority, these models are insufficient in handling the dynamic fracture of solids. This is because of the fundamental differences between static/quasi-static and dynamic deformation. For a quasi-static deformation, at any particular instance, a condition of static equilibrium holds, implying that the sum of the forces acting on any element in the material body is zero. Conversely, in a dynamic deformation situation, when high strain-rate loading is applied to the boundary of the body such as a blast wave or impact, wave propagation of the stress occurs and a sequence of states of equilibrium defined by the well-established equations of mechanics of materials (sum of forces equal to zero, sum of moments equal to zero, compatibility of strain, constitutive relations, etc.) are no longer sufficient [50].

The current state of the art of methods for dynamic fracture simulation at macroscopic levels is divided into two categories: continuum mechanics based models such as Finite Element Analysis (FEA) and discrete element based models (like smoothed particle hydrodynamics). Methods like FEA are well known to have limitations in fracture and fragmentation predictions. When simulating material fracture or fragmentation, the lack of continuity conditions of the material being fractured hinders the effective use of FEA. These limitations of FEA come from the fundamental principle that FEA treats the material as a continuum. This means that the global element assembly technique in FEA follows the compatibility condition which states that the interior nodes still must remain connected after deformation (i.e. must have the same nodal displacement) [43]. Therefore once the continuity of the material is broken due to fracture or fragmentation, re-meshing is required to distinguish the interior and boundary nodes in need of correct element assembly at a new evolving state of geometry for the next computation iteration. FEA has been continually developed to meet these requirements and though many re-meshing techniques have been established and embedded into FEA in the context of Lagrange, Euler, or

Arbitrary Lagrange Euler implementations [42], it is still not well suited to predict multi-cracking of materials, let alone fragmentation [50].

In the discrete element models, specifically SPH, the material is usually treated as an assembly of mass particles. The constitutive equations are selected to properly define the interactions among the discrete neighboring particles. SPH does not suffer from either the mesh tangling problem encountered when using a Lagrangian mesh or even the flux conservation problem when using an Eulerian mesh. This situation naturally leads one to SPH due to in its robustness in solving material discontinuity problems.

Under extreme loading, UHSC panels experience various stress states that lead to complex failure modes. In the worst case scenario for a single projectile impact event, which corresponds to an impact orientation normal to the surface, it has been observed that a crater is formed in the front surface followed by a strong compressive shock wave. This wave weakens as it traverses through the plate thickness and is eventually reflected off the free back surface [38]. This compressive shock wave reflection generates a tensile shock wave, which if large enough in magnitude, can lead to fracture on the rear face of the panel accompanied by spalling of the material behind the point of impact. Since the speed of shock waves propagating these materials can approach over 4000 m/s, this fracture takes place before a projectile can even penetrate through the target panel. Even blast loads on UHSC panels, which typically have a more uniform application of pressure on the front surface, can still cause abrupt catastrophic failure at the points of highest stress. Typically, a line along the rear of the panel will fracture causing it to break in half, but fragmentation will still occur along the line of fracture.

Such fracture and spalling phenomena in brittle materials becomes problematic when using the traditional Lagrangian finite elements available in commercial codes. By using a dynamic user-defined material model and coupling it with an element deletion scheme, these elements can handle the large strains and large strain rate conditions without computational bottlenecks. However, it has been found that to efficiently use an element deletion scheme without loss of accuracy or increase in computational time, very large strains can still be experienced in the model [39]. The resulting model can accurately predict the exit velocity of the penetrating projectile, but cannot track the free-flying fragmented pieces of the target which may be, especially, important when the fragments impinge a secondary target. The SPH numerical method has received considerable theoretical support since its inception. Beginning with the same material model and associated parameters as for a traditional finite element model, an SPH model can easily handle the complex failure states that occur during an impact event, and more accurately handle the fragmentation process in a more natural way [47].

6.2 Finite Element Analysis (FEA)

As mentioned previously, traditional FEA has many advantages when coupled with a dynamic user-defined material model. The model used in this study is very efficient and quick when used in FEA simulation. Models of this type have no issues with contact between a target and projectile or high-rate pressure loading from a blast wave. These models can easily handle the behavior of elements during damage initiation and evolution and the stress wave propagation that results from complex geometries and boundary conditions. Chapter 7 will more thoroughly discuss these advantages using multiple example problems.

The drawbacks to FEA simulations come in the form of particularly large strains inherent in extreme loads of brittle materials. For decades the high-strain, high strain rate modeling of ductile metals has been accurately simulated using the simplistic Johnson-Cook plasticity and damage models [21], [22]. These models use a similar failure surface (at least in formulation), damage scheme, strain rate law, and equation of state. The distinct difference that ductile materials under impact or blast rarely fragment to the degree that brittle materials do, though obvious, is the leading decision factor for what type of modeling scheme to use. When dealing with the extreme failure of ductile metals, an element deletion scheme is often used to allow for the complete penetration of a projectile (or the catastrophic fracture caused by blast). This is not optimal when dealing with brittle materials because a significantly larger portion of the damaged elements would need to be removed in order to accurately simulate the events. This would bring in errors when dealing with the conservation of mass. This removal of elements would also have to take place fairly early in the analysis in order to show the appropriate failure scenario, leading to the model simulating a weaker target than in real life and significantly increase the computation time. Chapter 7 will more thoroughly throw light on these difficulties with multiple example problems.

6.3 Smoothed Particle Hydrodynamics (SPH)

The smoothed particle hydrodynamics (SPH) method was first developed for problems related to astrophysics [14], with the important advance being a method for the calculation of derivatives without the mesh associated with the traditional finite element method. In the conventional SPH method the time-dependent partial differential equations, which describe conservation of mass, momentum, and energy and together with a constitutive equation describe the motion of a continuum, are discretized in space using kernel interpolation [50]. This method is based on a kernel interpolation which uses distributed interpolation points, with no fixed connectivity, to approximate field variables and their spatial derivatives. In SPH, spatial derivatives are calculated by analytical differentiation of the kernel function. For illustrative purposes, consider a continuum represented by a set of interacting particles as seen in Figure 6.1. Each particle i interacts with all surrounding neighbor particles within a given distance (traditionally 30-50 nearest particles). The smoothing length r controls this distance and all particles within r of the i particle are neighbor particles. The interaction between i and a neighbor particle is weighted by the kernel function, W_{ij}, where j represents the neighboring particle. Using this principle, the value of a continuous function can be approximated at any location within the domain based on known values at neighboring particles, j [50].

Over the past few decades, the application of SPH to solid mechanics, specifically for high-velocity impact, has been evolving for the last few decades. In this Lagrangian formulation variable element connectivity is used to allow for severe distortions. This Lagrangian representation is favored because it allows the grid to be embedded in the material and thus reduces some of the material interface problems associated with Eulerian codes. The ability of SPH to handle severe distortions allows it to be applied even to problems that have been specifically been reserved for Eulerian approaches [25]. The SPH technique was first introduced by Lucy and Gringold and Monaghan in 1977 [31], [14]. Thereafter, SPH nodes were linked to finite elements by Johnson et al. in 1993 [24], [20].

SPH is a numerical method that is part of the larger family of meshless methods. Instead of defining nodes and elements, one only needs a collection of points to represent a given body. In SPH, these points are commonly referred to as particles (mass points). The SPH methods used in this study are a fully Lagrangian modeling scheme that permits the discretization of a prescribed set of continuum equations by interpolating the properties directly at a discrete set of points distributed over the solution domain without the need of a traditional spatial mesh [25]. The difficulties associated with fragmentation and free-flying motion of spalled particles coupled with very large deformations of free surfaces are resolved in a comparatively natural way. Moreover, in a case where there is interest in the secondary impact of fragmented particles against some second target a certain distance away from the first target, SPH has no additional computational cost associated with tracking these fragments through a large empty volume (as would be prohibitively expensive with a coupled Eulerian-Lagrangian scheme).

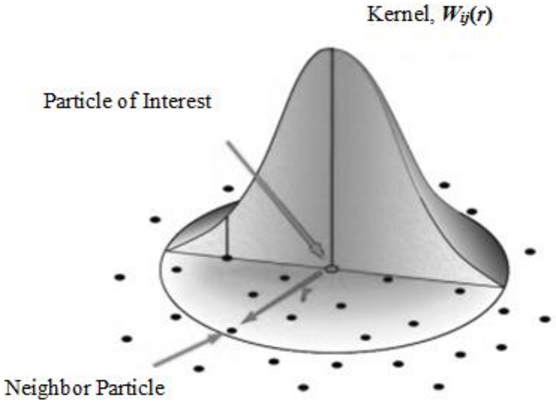

Figure 6.1 The SPH kernel function [28]

SPH is a method of estimating function values and gradients when the function values are known for a set of disordered points (not necessarily in a traditional, gridded finite element mesh). Following Monaghan [33], the value of an arbitrary function *F* at a particle *i* is approximated as

$$\langle F_i \rangle = \sum_i V_j F_j W_{ij} \tag{6.1}$$

where the kernel *W* is a function of the smoothing length *h* and the distance between particle *i* and its neighbor *j*. The volume assigned to each particle, *V*, is usually expressed in terms of density and particle mass as

$$V_j = \frac{m_j}{\rho_j} \tag{6.2}$$

The gradient of *F* can be found by taking the gradient of the kernel

$$\langle \nabla F_i \rangle = \sum_j V_j F_j \nabla W_{ij} \tag{6.3}$$

The governing equations of solid mechanics are modeled using Eq. (6.3) to compute required gradients [28]. Typical SPH kernel functions satisfy the normalization condition that the integral of the kernel over its region of influence should equal unity [33]. However, this condition is not generally satisfied in the discrete summation form as applied in SPH. As a result, SPH cannot properly evaluate the values or gradients of a constant function. Belytschko introduced the definition of consistency order from the finite element method as the "order of polynomial that can be represented exactly" [6]. Traditional SPH doesn't achieve 0 order consistency and this lack of consistency leads to significant error when the particle spacing is not uniform [28]. This creates computational difficulty when trying to simulate large objects where SPH is only necessary in a highly localized region in the model.

The SPH scheme used in this work includes a virtual artifact as the "domain." This is a rectangular region computed at the beginning of the analysis as the bounding box within which the particles are tracked. This fixed rectangular box is 10% larger than the overall dimensions of the whole model and is centered at the geometric center of the model. As the analysis progresses, if a particle moves outside the domain, then it behaves like a free-flying point mass and no longer contributes to the SPH calculations. As mentioned earlier, SPH interpolates the properties of each particle. This is done using what is called a "smoothing length calculation". Even though particle elements are defined in each model using one node per element, the SPH method computes contributions from each element based on adjacent particles that are within a sphere of influence. This smoothing length governs the interpolation basis of the method. For every increment, this local connectivity is recalculated internally and the kinematic quantities like normal and shear strains as well as deformation gradients are computed [47].

However there are some limitations inherent with SPH models that are not present in FEA models. In regions of the model where deformations are not too large and elements are not highly distorted, the SPH analyses are found to be less accurate in general than Lagrangian finite element analyses. Another large problem that has been identified is that of tensile instability. When the material is in a state of tensile stress, the particle motion may become unstable. This instability is strictly related to the interpolation technique of the standard smoothed particle dynamic method. Because of this instability, particles tend to clump together and show numerical fracture-like behavior and artificial voids. The underlying cause has been shown to be a lack of formal consistency in SPH. It cannot reproduce exactly any class of functions on a defined set of points. Because of this drawback, a numerical clumping instability manifests itself when nodes are mutually attracted. More specifically, the SPH kernel function is unable to keep the nodes apart once they are sufficiently close to each other [32].

Yet another limitation inherent to the SPH functionality currently implemented in Abaqus is that bodies modeled with particles that were not defined with the same material cannot interact with each other. Therefore, SPH cannot be used to model the mixing of bodies with dissimilar materials. This limits one to model only the brittle target panel with particles; whereas, the projectile model must use traditional finite elements. The new functionality of Abaqus version 6.12 has incorporated the automatic conversion of finite elements to SPH particles. This eliminated many of the limitations associated with applying loads directly to bodies that could, eventually, become particles. But this functionality has the limitation that once the elements are converted to particles, whether by time-, stress-, or strain-based criterion, they are free-flying particles which no longer obey symmetric boundary conditions. This leads to inaccurate fragmentation patterns if a user wishes to take advantage of the symmetry in the problem.

Within this study, all simulations using SPH functionality are built the same way as the FEA models. In all simulations, the panel (brittle) is meshed using particles. To do this, the panel is meshed in the exact same way as the FEA models. Once the mesh is assigned, a set of all the nodes within the panel mesh is made, which is then converted manually within the input file to particles. Figure 6.2 illustrates the process of meshing a part and then converting to particles.

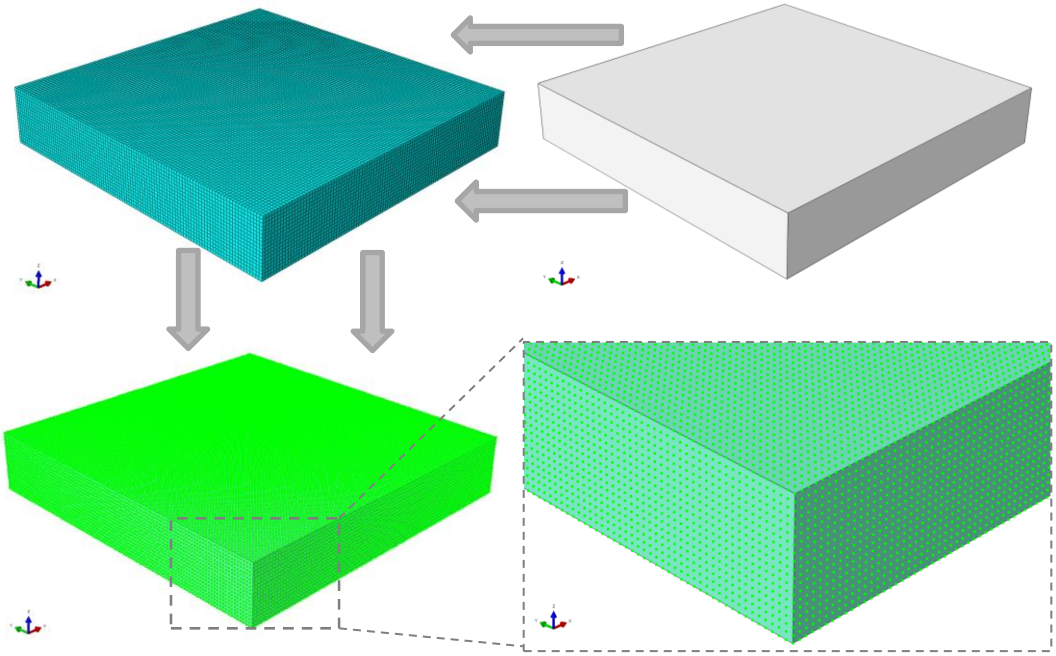

Figure 6.2 Particle meshing process in SPH models

Chapter 7

Numerical Simulations

7.1 Introduction

In the study of impact phenomena, many problems of the low-velocity regime (< 250 m/s) fall in the area of structural dynamics. As the impact velocity increases to the range of 500-2000 m/s, the response of the structure becomes secondary to the behavior of the material within a small zone (typically 2-3 times the projectile diameter) of the impact area [57]. As discussed, the mechanics of ballistic impact on plates is a problem of high complexity. The nature of response is determined by material type as well as nature and dimensions of the target, namely, semi-infinite or finite. Moreover, the shape, size, material type, velocity, and angle of impact of the projectile are important contributory factors. In order to validate the material model described in this paper, actual tests were undertaken in the laboratory at ERDC on USHC panels for both UHSC-1 and Ashcrete. One of the main concerns in the study of impact phenomena is the determination of a velocity below which an object will fail to perforate a protective barrier. This determination is of utmost importance in the design of protective structures or for the evaluation of the effectiveness of military armors. This velocity is referred to commonly as the ballistic limit. There are two approaches for finding this limit: deterministic and probabilistic. In the former, the ballistic limit is determined from physical principles, but due to the complexity of the governing partial differential equations, simplifications and assumptions are introduced that generally require empirical determination of one of two constants. In the probabilistic approach, models are built relying on a substantial base of data consisting of the object’s striking velocity and its residual velocity.

The deterministic approach to ballistic limits is a history of attempts to determine projectile performance during penetration through development of models based on conservation laws and assumptions about the mechanical behavior of the system. One of the major simplifications is assuming that the projectile is rigid and uniform in shape. The corresponding takes the form

$$V_r = \begin{cases} 0, 0 \le V_s \le V_l \\ \alpha\left(V_s^{\,p} - V_l^{\,p}\right)^{l/p}, V_s > V_l \end{cases}, \tag{7.1}$$

where V_r is the projectile residual velocity, V_s is the projectile striking velocity, and V_l is the limit velocity.

For rigid projectiles, p = 2 and α, V_l are empirical parameters determined from a regression analysis. Limit-velocity curves, as shown in Figure 7.1, define boundaries with a sharpness that is unreal. Near these boundaries, terminal behavior tends to be probabilistic in nature, rather than deterministic. Figure 7.2 is a typical plot of the probability of complete penetration as a function of velocity for a certain projectile and target combination. This plot was obtained by firing a great number of rounds so as to obtain a statistically significant sample. Any velocity in the range of mixed results can be used as a limit velocity. For example, the V_{10} and V_{90} limit velocities are those velocities at which there is a 10% and 90% probability of a complete penetration, respectively. Usually the V_{50} limit velocity is used to represent the ballistic limit. Near V_{50}, the slope of the probability curve is greatest and, thus, the V_{50} can be located with greatest precision.

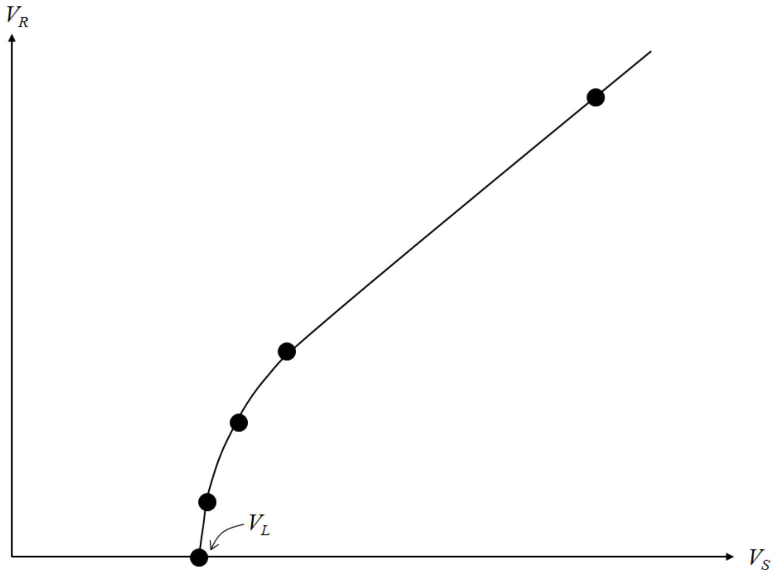

Figure 7.1 Limit-velocity curve

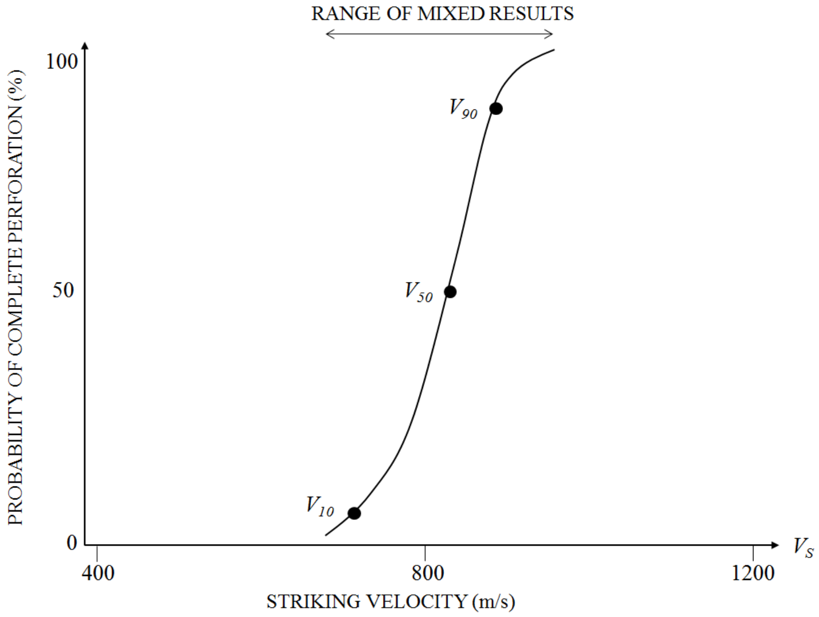

Figure 7.2 Typical penetration-probability curve

Another primary concern for military design engineers is the response of protective armor panels to fragments from mortars and other improvised explosives. A mortar is an indirect fire weapon that fires explosive projectiles known as mortar bombs at low velocities, short ranges, and high-arcing ballistic trajectories. These are considered small-arms weapons, i.e. capable of being transported by personnel without vehicle assistance. The danger of mortars is that it hurtles fragments of shrapnel radially outward from the explosive at significantly higher velocities than traditional bullets. Whereas the typical range of velocities for bullets from guns seen in war environments are somewhere between 300-500 m/s, mortar fragments can reach velocities greater than 1000 m/s. These hypervelocity speeds coupled with the unknown shape makes impact from these fragments extremely difficult to predict. To tackle this problem, laboratory tests at ERDC used a fragment simulating projectile (FSP) at velocities greater than 1000 m/s.

For these two types of tests (ballistic limit and fragment simulating), different panel materials and projectiles were used. For the ballistic limit tests, 20 panels of UHSC-1 were shot with a spherical projectile. For the fragment simulating tests, several panels of Ashcrete were shot with a steel FSP. The fragment simulating tests were also done for single panel cases as well as stacked panels, where two of the same dimension and material panels were stacked back-to-back to improve the impact resistance. In all experiments, the same ballistic testing facility and test setup was used. A diagram of the experimental setup is shown in Figure 7.3. A universal receiver and 0.50 caliber test barrel fired the projectile first through a blast panel, which is essentially a steel plate with a small hole cut out for the projectile to pass. This panel prevented any powder or other particles to be picked up by the first set of chronograph screens (which determine the impact velocity, V_i). The projectile penetrates the specimen and passes through a witness panel, which is used to stop any spalled material from passing through the second set of chronograph screens used to determine the residual velocity, V_r.

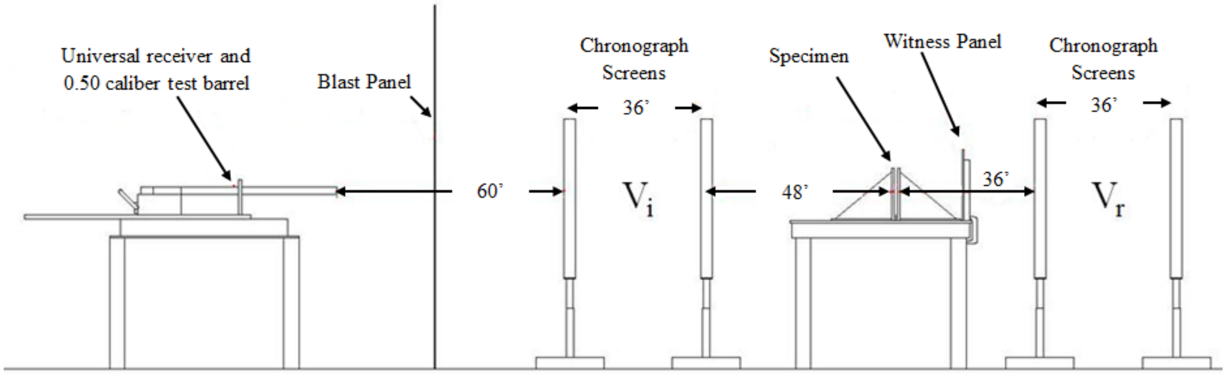

Figure 7.3 Typical experimental setup for ballistic performance evaluation tests

These experiments and their corresponding simulations are discussed in the following three sections. Simulations using both FEA and SPH have been completed and compared. All simulations were completed on an AMD Phenom^{TM} II X6 1075T Processor (3.00 GHz).

7.2 Application of Model to Ballistic Limit Test

For this study, UHSC-1 target was used to validate the modeling schemes. This UHSC had a compressive strength of f_c' = 216 MPa. Actual ballistic impact laboratory experiments to determine the ballistic limit were undertaken for comparison of traditional element models to SPH models. The panels tested were of size 305 mm x 305 mm x 27 mm and clamped on all four sides as shown in Figure 7.4. The projectile was a 12.7 mm diameter sphere made of AISI Type S2 Tool Steel and was fired at the target panels at speeds between 350 m/s to 500 m/s, the range of ballistic limit for this panel material. The material parameters used to simulate the elastic-plastic behavior of the steel projectile are listed in Table 7.1. To model this experiment, two-way symmetry was utilized requiring only one quarter of the panel and projectile to be simulated. Appropriate symmetric boundary conditions were implemented along the axes of symmetry and the periphery of the panel enforced fixed boundary conditions. Figure 7.5 shows an isometric view of the model configuration and mesh. The projectile, as shown in the enlarged view on the right, has been initiated with a predefined field to induce an initial velocity of V_i = 483 m/s at the instant of impact in the positive Z direction. In both FEA and SPH models, 187,272 degrees of freedom were used in the panel while 848 linear tetrahedral elements were used in the projectile.

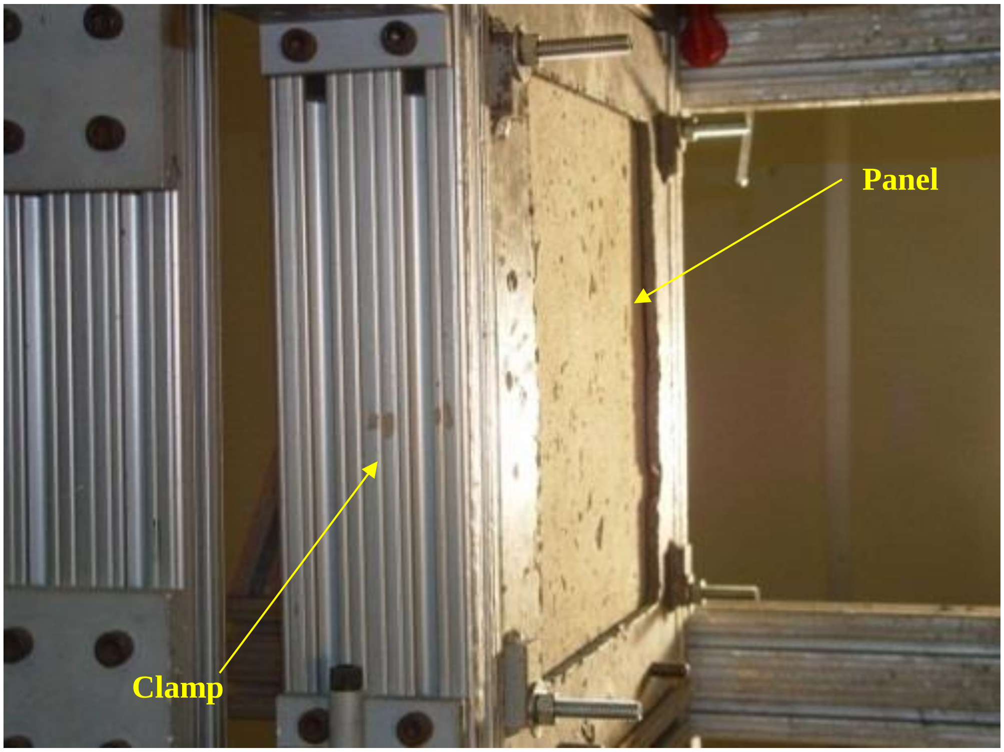

Figure 7.4 Target panel in test setup (exit side, before impact)

Table 7.1 Type S2 Tool Steel Material Constants (Spherical Projectile)

Variable	Description	Value	Units
ρ	Density	7.79E-09	Tonne/mm^3
E	Young's Modulus	190,000	MPa
ν	Poisson's Ratio	0.25	
σ_y	Yield Stress	2,000	MPa
ε_{pl}	Plastic Strain	0.0105	

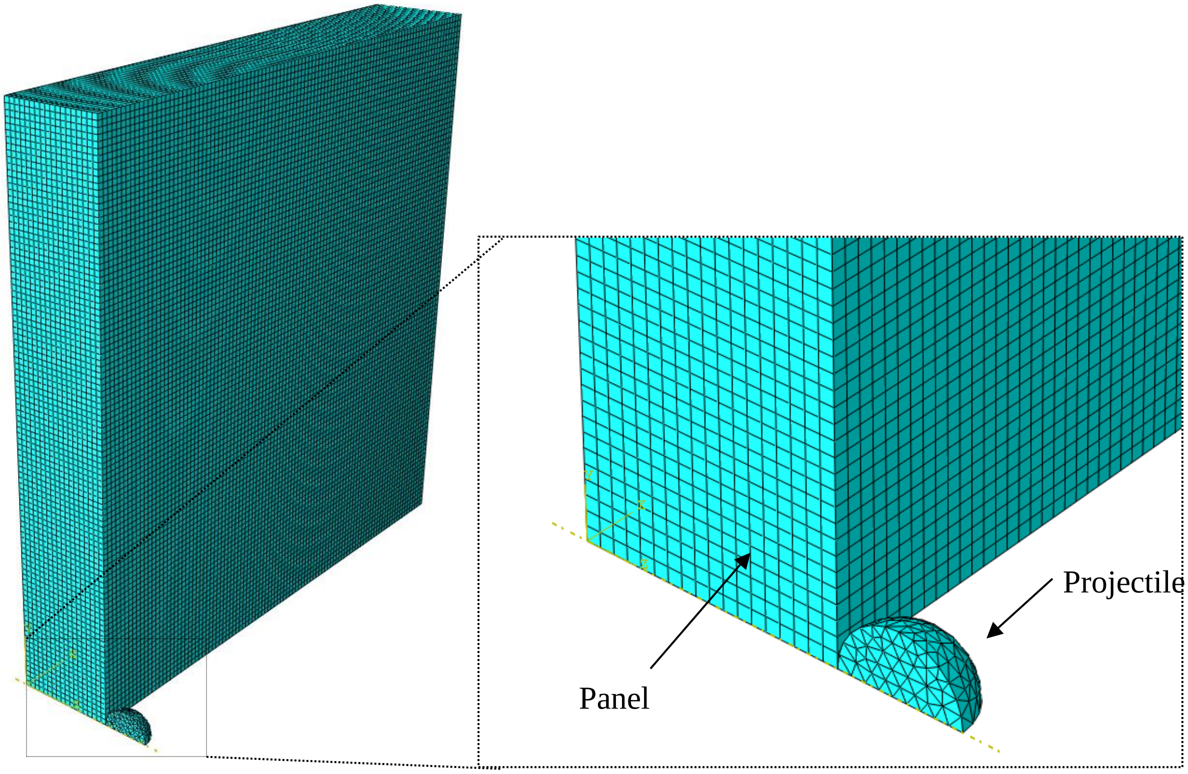

Figure 7.5 - Model assembly and mesh for ballistic limit test

Twenty ballistic impact experiments were undertaken to validate the models built for this purpose. Views from one such experiment is shown in Figure 7.6. As seen on the left (the front side of the panel), the hole created by the projectile is only slightly larger than the diameter of the projectile itself (13 mm). However, the crater formed is approximately five times that size (63 mm). It is noted that for some of the experiments, a few large cracks emanated from the impact site and followed the shortest path to the periphery. But in majority of the experiments, damage was found to be highly localized and no significant cracking occurred away from the damaged region. For the experiment shown in Figure 7.6, the impact velocity was 483 m/s and the residual velocity was 88 m/s. Figure 7.7 shows images from high-speed video taken of the same experiment and at a similar viewing angle as in Figure 7.4. As shown, the damage is highly local, but there is extremely large amounts of fragmentation taking place relatively early in the impact event.

Figure 7.6 Target panel test setup (front side and exit side, after impact)

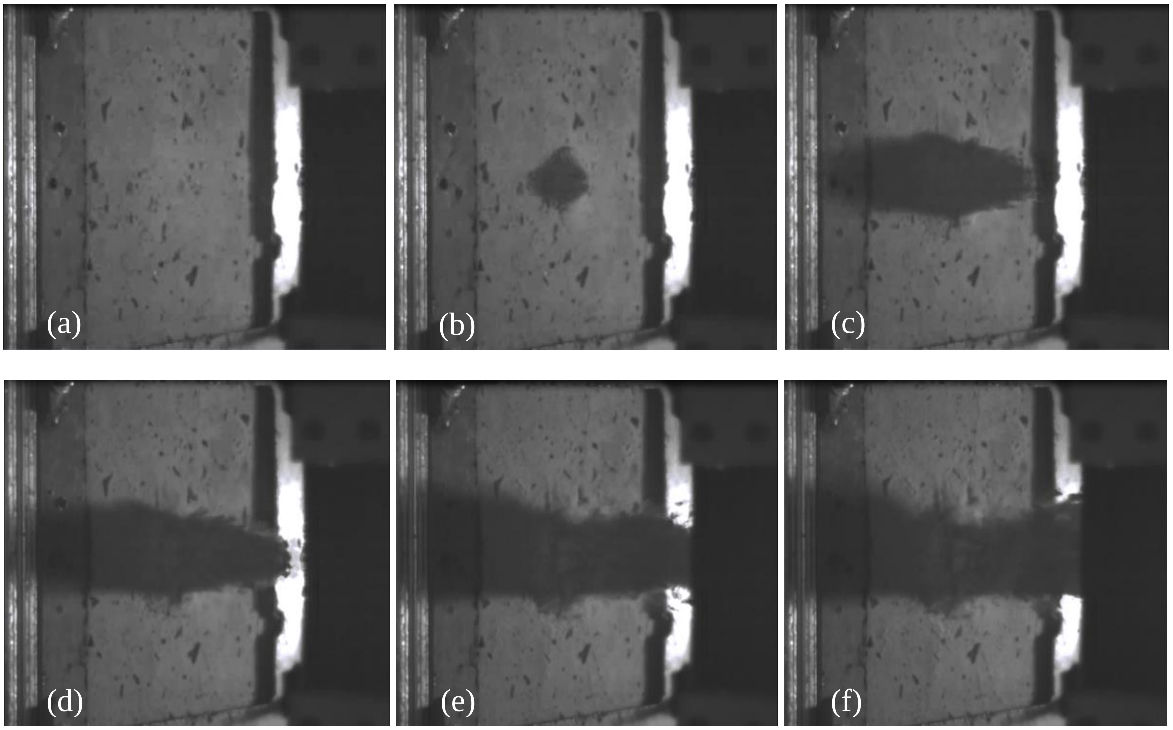

Figure 7.7 Exit side of UHSC-1 target panel at increasing instances of time (a) through (f)

The model presented relies heavily on the calculation of plastic strain for use in the damage evolution model. Figure 7.8 below shows the results of the model once a constant velocity is achieved, signifying that the projectile continues penetrating the panel with no further resistance. The residual velocity of the projectile for the FEA model was 92 m/s. The FEA model was found to be very good at predicting the exit velocity as well as the approximate failure pattern, but as shown by the cross sectional view of the panel the elements in front of the projectile path were heavily distorted. Eventually the analysis stopped when the distortions became excessive. A brief study was undertaken incorporating the element deletion option using effective plastic strain as a metric for removing excessively distorted elements from the mesh. The resulting outcome will be discussed in detail in the next section. The total analysis time of the run was 22 minutes, 21 seconds.

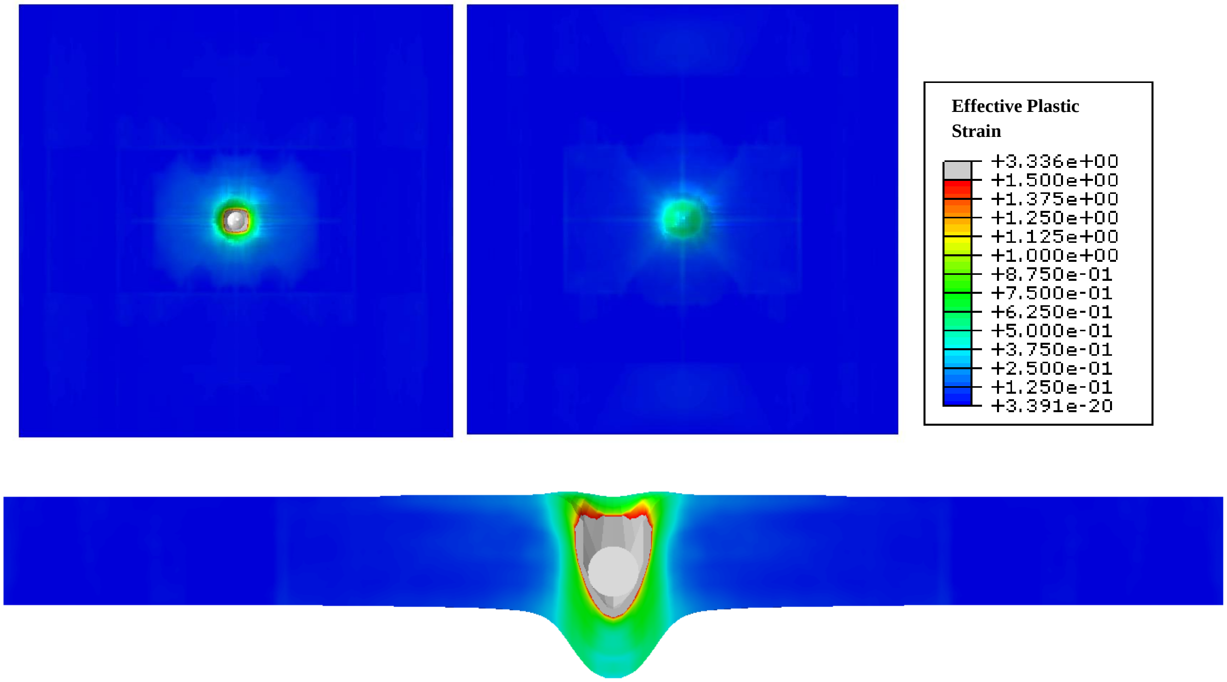

Figure 7.8 Effective plastic strain contours of FEA model

An identical model to the FEA model shown in Figure 7.5 was created, but SPH was used instead. The same VUMAT, material properties, boundary conditions, and number of elements as the FEA model were used. This allowed for a direct comparison of the performance of FEA and SPH models. Figure 7.9 illustrates the results of the SPH model. The residual velocity of the projectile from the SPH model was 138 m/s. This is significantly higher than the velocity predicted by the FEA model as well as the experimental results. Additionally, the SPH model took longer to run. This can be attributed to the smoothing length calculation that is undertaken at each increment, for each particle. However, enabling the excessively strained particles to become free-flying point masses is highly advantageous. This eliminates the complications associated with excessive distortion, element deletion, and secondary impact. The failure pattern predicted by the SPH model is highly accurate as is the spalled behavior of the fragmented UHSC material directly in front of the projectile. The total analysis time was 1 hour, 40 minutes, 20 seconds, which is more than four times longer than needed with the FEA model, and can be viewed as a significant drawback for SPH.

The traditional FEA model performed significantly better in predicting the exit velocities of the projectile than a comparable SPH model. The FEA model is also faster to run. Figure 7.10 shows the impact velocity vs. the residual velocity of the twenty experiments, the FEA model, and the SPH model. Figure 7.11 shows the velocity vs. time for both models compared to the experimental value. These results suggest that the SPH model predicts a relatively weaker panel than the equivalent FEA model without element deletion.

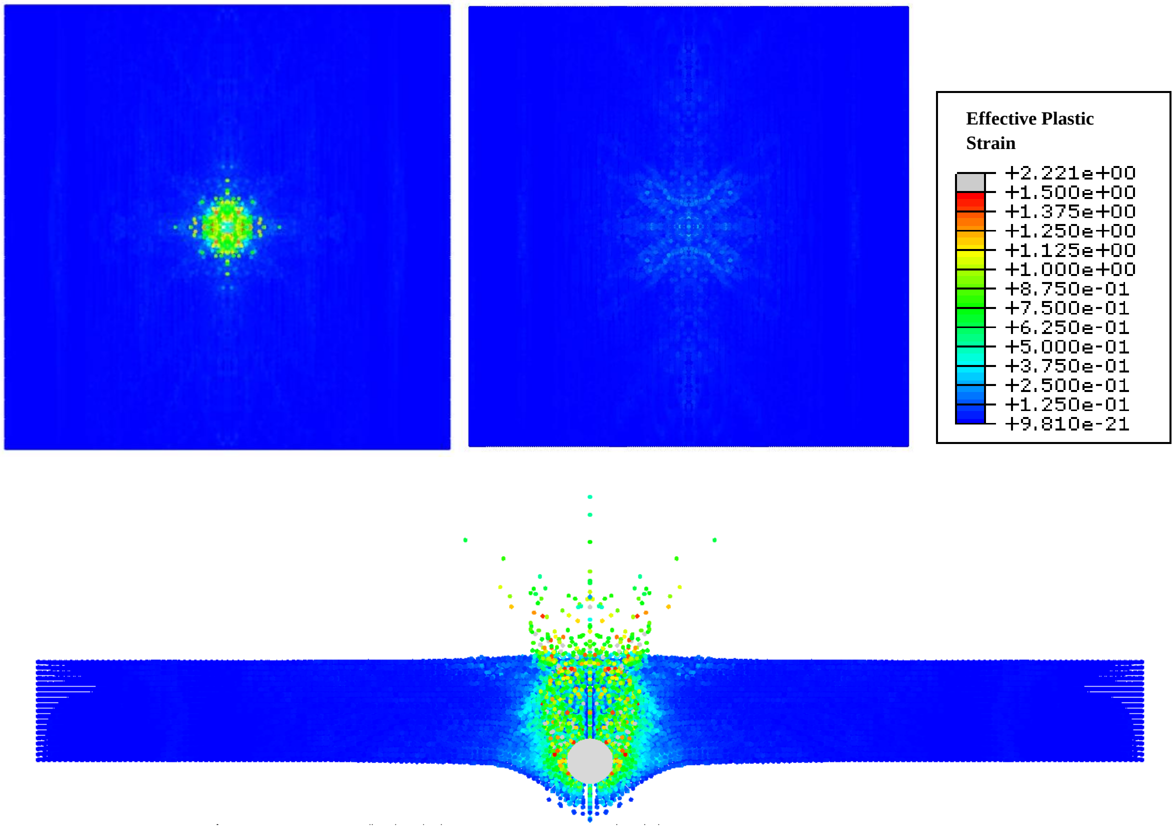

Figure 7.9 Effective plastic strain contours of SPH model

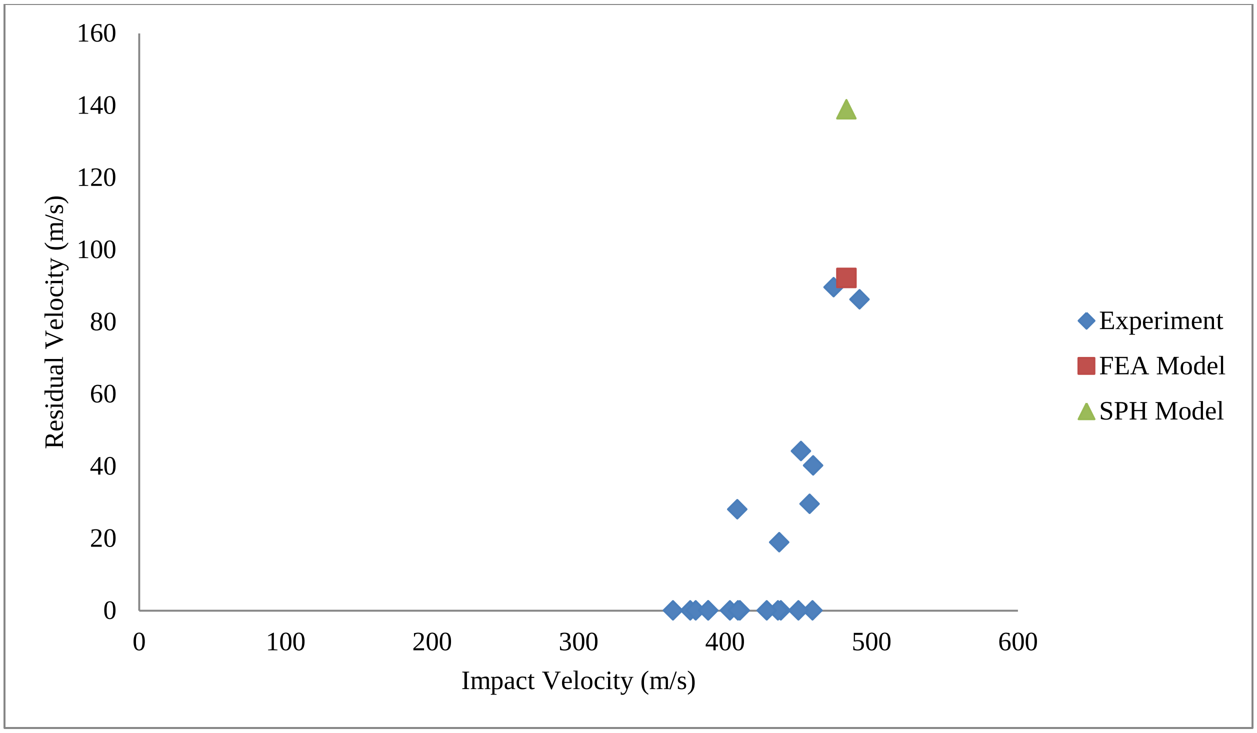

Figure 7.10 Impact vs. residual velocity of ballistic limit experiment and models

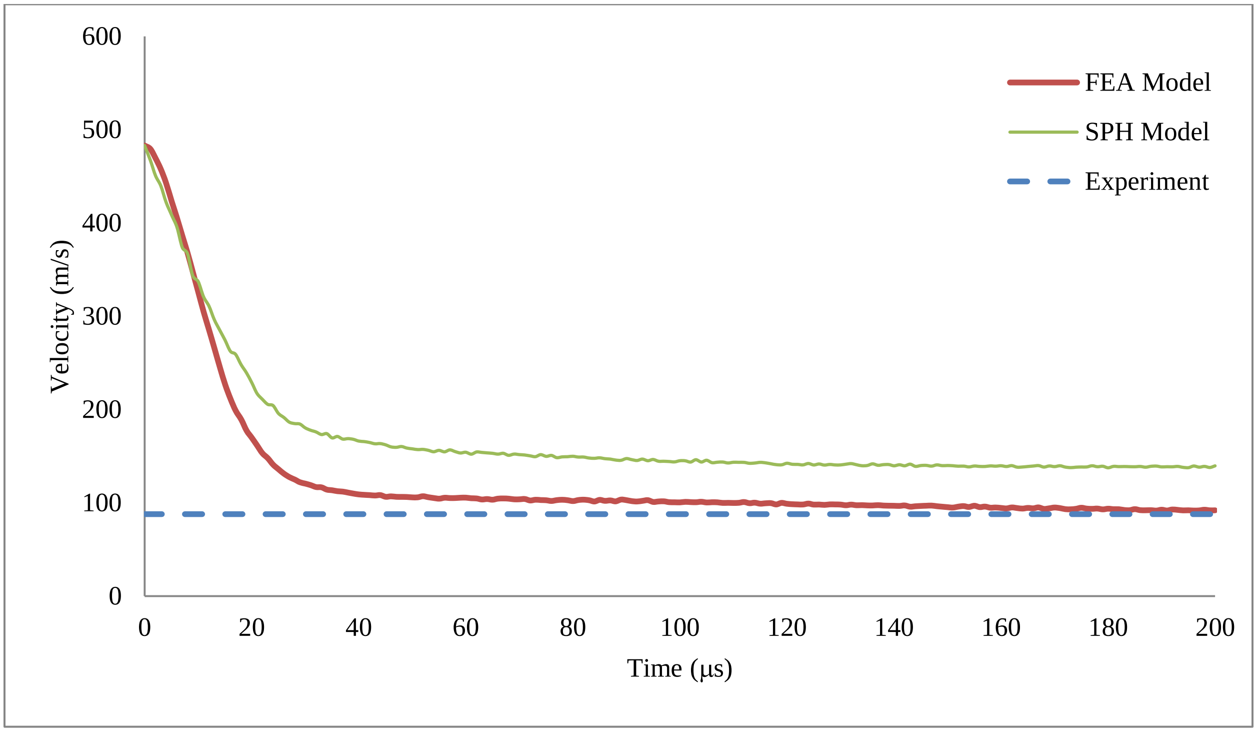

Figure 7.11 Velocity vs. time of FEA and SPH models compared to experiment

7.3 Application of Model to Single Panel

In this study, Ashcrete panels were tested in the laboratory. They were approximately 304.8 x 304.8 x 11.9 mm and clamped at the periphery. The projectile used was a MIL-P-46593A Standard FSP. It is a 0.50 caliber, 207 grain FSP made of 4340-H Steel with a Rockwell Hardness of C = 30±1. Multiple tests were performed with impact velocities varying between 1067 m/s and 1097 m/s with the impact angle oriented normal to the plate surface. A picture of the FSP is shown in Figure 7.12 as well as the projectile model and mesh used for all simulations discussed in this paper. The projectile model contained 584 linear hexahedral elements (C3D8R) and the panel elements varied depending on the individual simulation. All initial shots were fired eccentrically with respect to the center of the panel, namely, closer to a corner. The purpose of this was to re-mount a damaged panel and fire at an opposite corner to test the ballistic resistance of a damaged panel. For this study, only the first projectile is simulated. The problem of a multiply impacted panel is a problem of high complexity and deserves future study.

Figure 7.12 MIL-P-46593A Standard 0.50 Caliber FSP (left) and model (right)

For the projectile, the Johnson-Cook plasticity and damage models were used. The model constants for 4340-H steel are given in Table 7.2. For the projectile, the Johnson-Cook plasticity and damage models were used. Eqs. (7.1) and (7.2) give the failure surface (von Mises tensile flow stress, σ) and the general expression for the strain at fracture (ε_f), respectively. The constants were taken directly from two studies completed by Johnson and Cook [21], [22]. Figure 7.13 shows a test plate target on the left (impact side). A steel-frame clamp constrains the plate at the periphery. On the right is the same test plate after impact. The hole in the panel is only slightly larger than 1 inch, but the crater on the entrance side is roughly 2 inches in diameter. Only one significant crack propagates from the impact region. Also, two larger cracks developed at the lower-left and upper right corners. Repeated experiments at such high impact velocities showed that the effects of damage were mostly localized. This fact was further supported by simulations, as discussed in the following. Figure 7.14 successively shows the damage process on the exit side of the test plate target at time instants of 110 μs, 310 μs, and 510 μs after firing of the FSP. These high-speed video frames show large amounts of fragmentation, but again, a relatively small damaged region.

$$\sigma = \left(A + B\varepsilon^{n}\right)\left(1 + C\ln\left(\dot{\varepsilon}^{*}\right)\right)\left(1 - T^{*m}\right) \tag{7.1}$$

$$\varepsilon^{f} = \left(D_1 + D_2 e^{D_3\sigma^{*}}\right)\left(1 + D_4 \ln\left(\dot{\varepsilon}^{*}\right)\right)\left(1 + D_5 T^{*}\right) \tag{7.2}$$

Table 7.2 4340-H steel material constants for Johnson-Cook Material Model

Variable	Description	Value	Units
ρ	Density of material	7.83E-09	Tonne/mm^3
E	Elastic modulus	205,000	MPa
ν	Poisson's Ratio	0.29	
A	Johnson-Cook Plasticity Constant	792	MPa
B	Johnson-Cook Plasticity Constant	510	MPa
n	Johnson-Cook Plasticity Constant	0.26	
m	Johnson-Cook Plasticity Constant	1.03	
θ_{melt}	Melting Temperature	1793	K
$\theta_{trans.}$	Transition Temperature	293	K
C	Strain Rate Constant	0.014	
$\dot{\varepsilon}_0$	Reference Strain Rate	0.002	
D_1	Johnson-Cook Damage Constant	0.05	
D_2	Johnson-Cook Damage Constant	3.44	
D_3	Johnson-Cook Damage Constant	-2.12	
D_4	Johnson-Cook Damage Constant	0.002	
D_5	Johnson-Cook Damage Constant	0.61	

Figure 7.13 Ashcrete target panel before (left) and after (right) impact

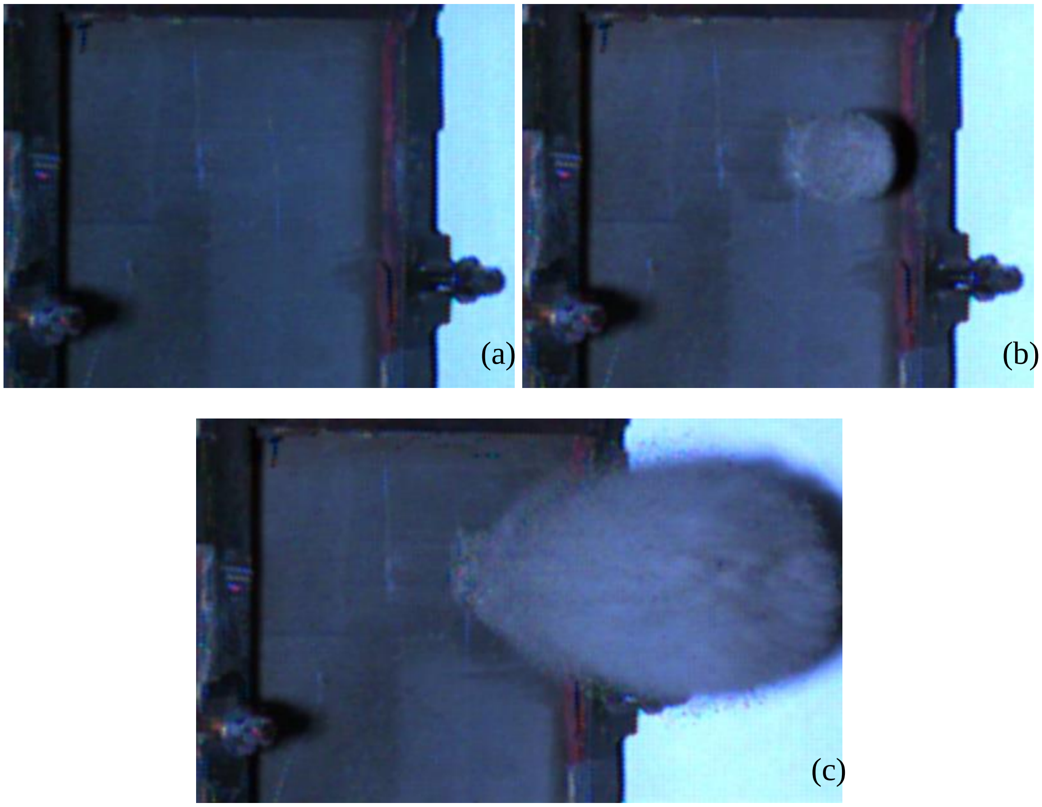

Figure 7.14 Exit side of target panel at (a) 110 μs, (b) 310 μs, and (c) 510 μs after firing of FSP

As stated previously (and illustrated in Figure 7.13), the FSP impacted the panel eccentrically so as to reuse the panel for a second shot. This raised the concern that the location of the impact closer to the boundary condition would affect the performance of the panel. To test this, two cases of a single panel FSP simulation were completed: (1) the centric impact case and (2) the eccentric impact case. These were done within the FEA framework only. Figure 7.15 shows an isometric view of the model configuration and mesh. The projectile, as shown in the enlarged view on the right, initiated with a predefined field to induce an initial velocity (V_i) at the instant of impact in the positive *Z*-direction. To replicate the experimental setup as closely as possible, fixed boundary conditions were enforced at target's peripheral surfaces. The impact velocity, V_i, was 1076.8 m/s and the result showed a residual velocity of 784.2 m/s. Figure 7.15 shows the scalar damage value, *D*, of the front and rear of the panel after impact. A value of 0 signifies an undamaged element whereas a value of 1 signifies a fully damaged element. As part of this exercise, a brief study of the effect of element deletion was undertaken. In order to increase the speed of calculation, a highly distorted element was deleted when its effective plastic strain value, ε_{pl}, reached a predefined maximum value, $\varepsilon_{pl}^{\max}$. This, supposedly, allowed for more efficient computation by removing highly distorted elements that were no longer appreciably contributing to the results. A note of caution is that the process of element deletion happens to be separate from the damage evolution process within an element.

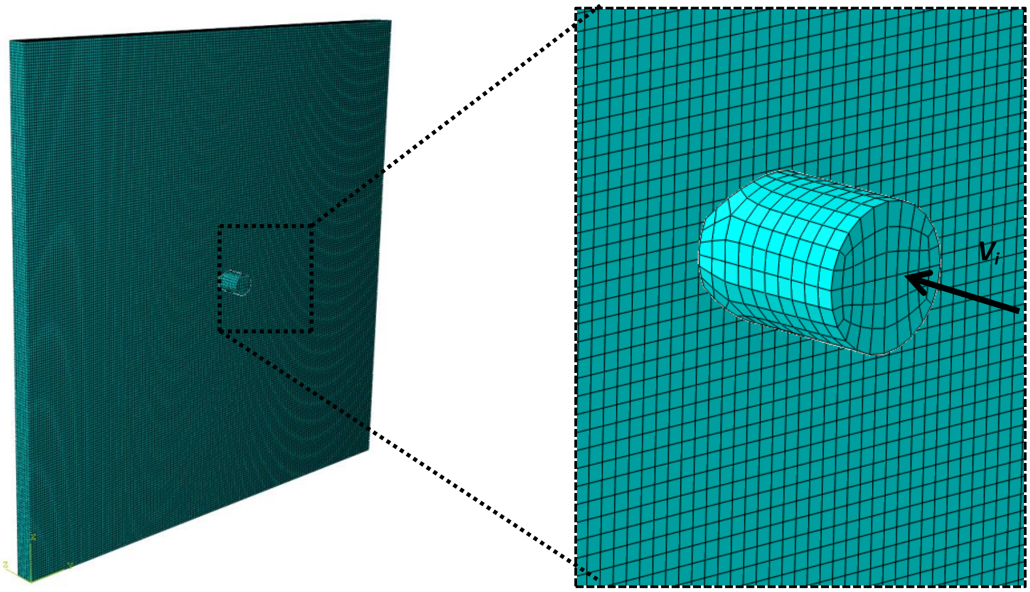

Figure 7.15 Assembly and mesh of Ashcrete FSP model (Centric Case)

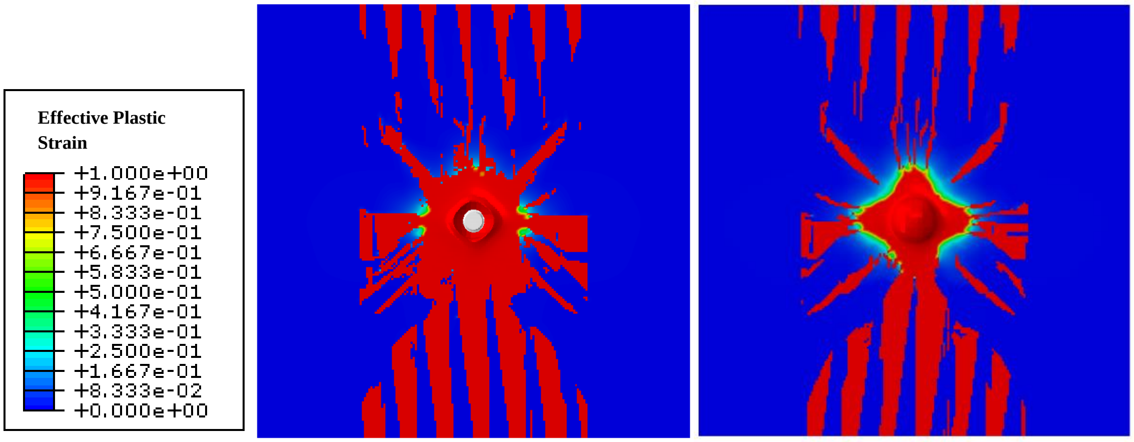

Figure 7.16 Simulation results of Ashcrete panel with scalar damage parameter (Centric Case)

Figure 7.18 shows an isometric view of the model configuration and mesh for the eccentric case (the model replicating the actual experiment as seen in Figure 7.13 and Figure 7.14). As in the centric case, the projectile, as shown in the enlarged view on the right, was activated with a predefined field to induce an initial velocity, V_i, at the instant of impact in the positive Z-direction. To replicate the experimental setup as closely as possible, as before, fixed boundary conditions were enforced at the panel's peripheral surfaces. A convergence study was undertaken to determine the appropriate mesh density for accurately predicting the residual velocity. The final panel mesh consisted of 2,334,784 degrees of freedom. No further refinement was used because the change in residual velocity prediction between the previous mesh refinement (1,618,400 degrees of freedom) and the final mesh refinement (2,334,784 degrees of freedom) was less than 0.7% but with a significant increase in computation time. Figure 7.17 shows the results of the convergence study, illustrating both the convergence to the actual solution and the exponential increase in computation time.

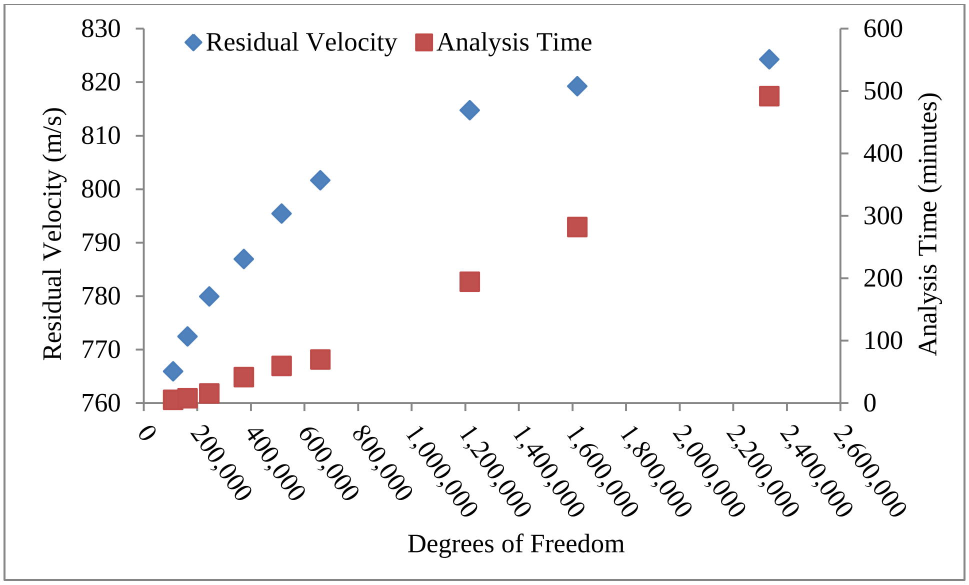

Figure 7.17 Mesh refinement study results

In all cases, the Abaqus simulation was continued until the projectile reached a constant residual velocity, signifying that the projectile had escaped the target after full penetration. In Figure 7.19 the velocity as a function of time for both the cases, centric and eccentric impact, is shown. The results suggest that at such high velocities, projectile impact location is irrelevant. However, as the value of $\varepsilon_{pl}^{\max}$ was decreased, the value of velocity over time increased, implying that the removal of the distorted elements leads to a weaker target, accompanied by an increase in the time to complete the simulation. In the cases shown, that is when $\varepsilon_{pl}^{\max}$ is equal to 2.5, 1.5, and 1.0 (or 250%, 150%, and 100%), the simulation times were 9 minutes, 64 minutes, and 104 minutes, respectively. Previous studies into element deletion have suggested that a value of 150% for ε_{pl}^{max} is sufficient to achieve computational efficiency without sacrificing accuracy [12].

Majority of models and codes for impact and penetration of brittle composites use the scalar quantity of effective plastic strain as a metric to evaluate the damage or failure in a material. The present model also relies heavily on the calculation of plastic strain for use in the damage evolution model. Specifically, attention is focused on the panel being impacted at an initial velocity of 1076.8 m/s. Figure 7.20 shows snapshots, from the impact side as well as the cross section, of damage at 10, 20, 30, and 40 μs.

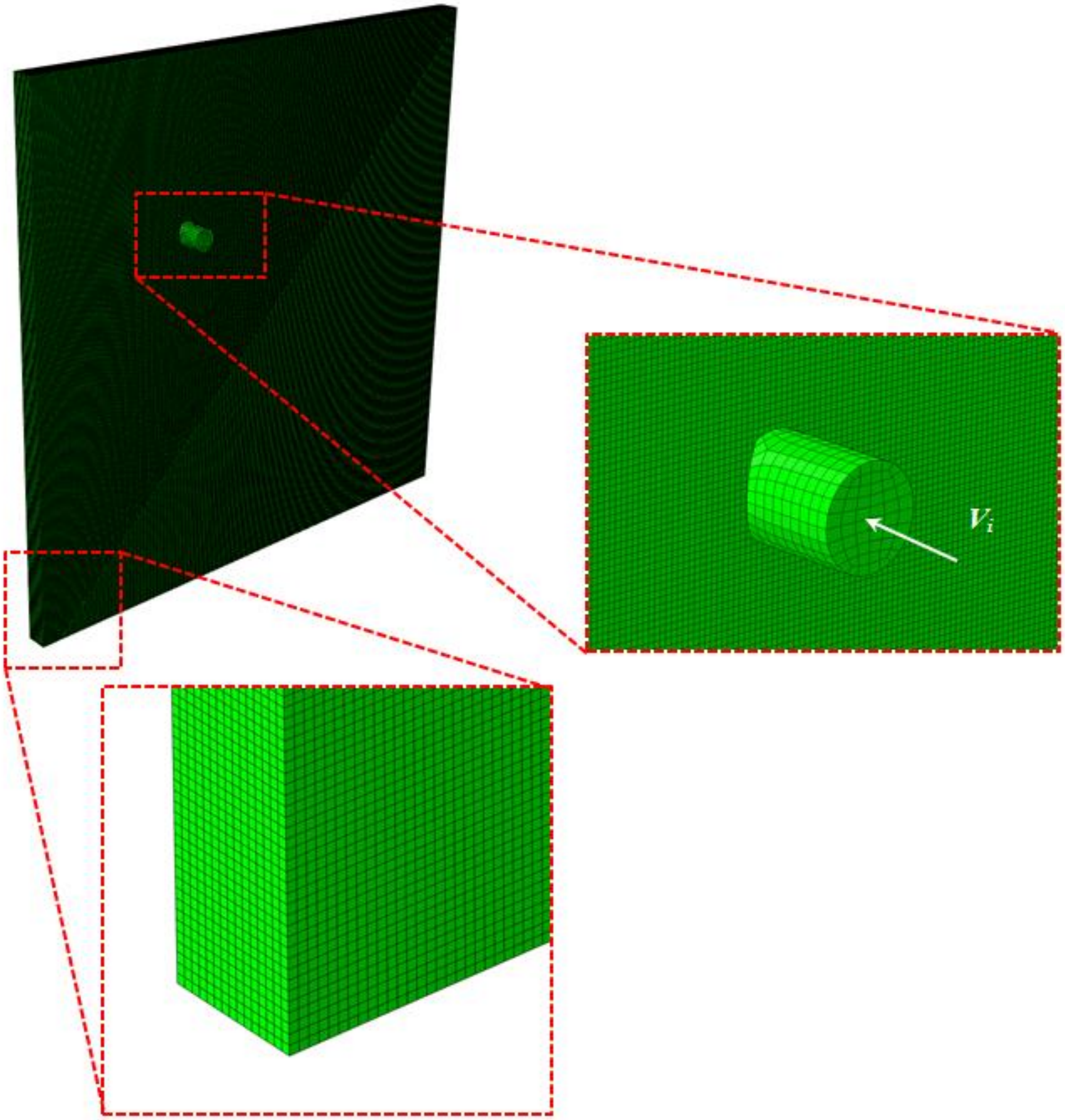

Figure 7.18 Assembly and mesh of Ashcrete FSP model (Eccentric Case)

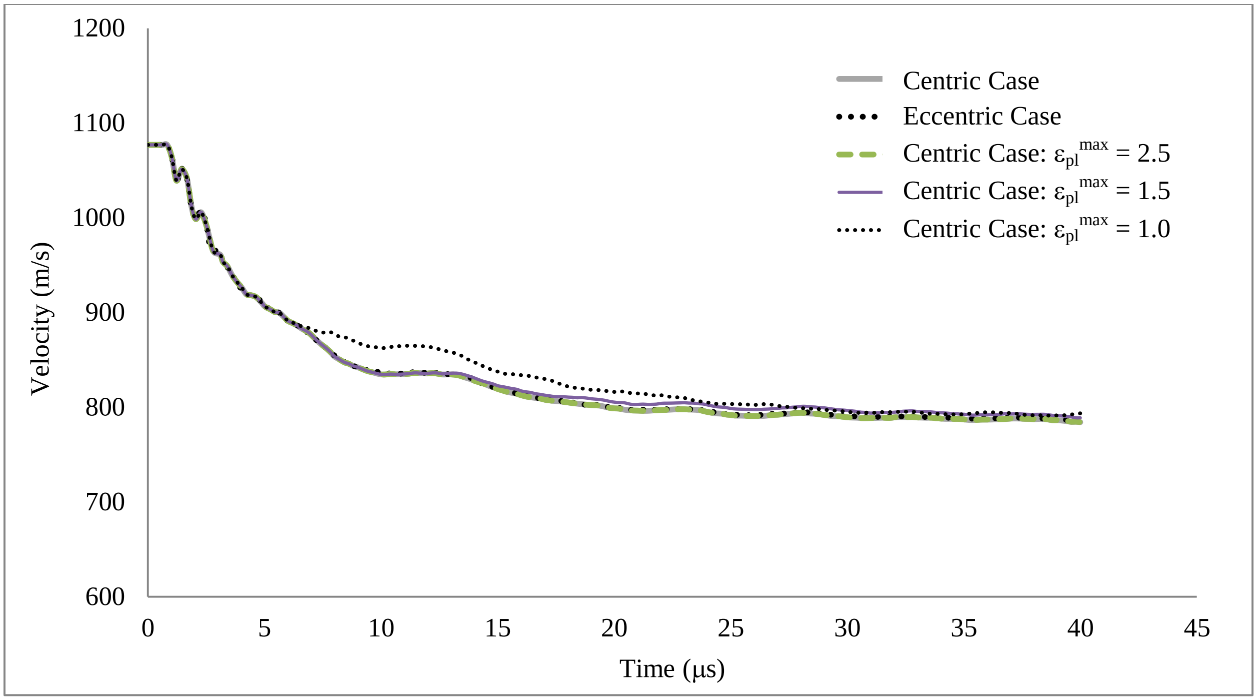

Figure 7.19 Velocity vs. time of Ashcrete FSP models for both centric and eccentric models

Now the performance of the FEA and SPH models are evaluated and compared. Two metrics were used to compare the performance of the two models with respect to the experimental result. The first metric is the residual velocity of the FSP after full penetration. The second metric is the damage pattern seen in the panel. Due to the heterogeneous nature of Ashcrete, there was a wide range of values that were seen in the experiments. The average exit velocity seen in the experiments was 829 m/s. The exit velocity seen in the FEA model was 824 m/s and the exit velocity in the SPH model was 832 m/s. These values have an error that is only 0.67% off and 0.28% off of the average experimental value, respectively. The velocity histories of both models are compared in Figure 7.21 with the baseline experimental average shown in the dotted line.

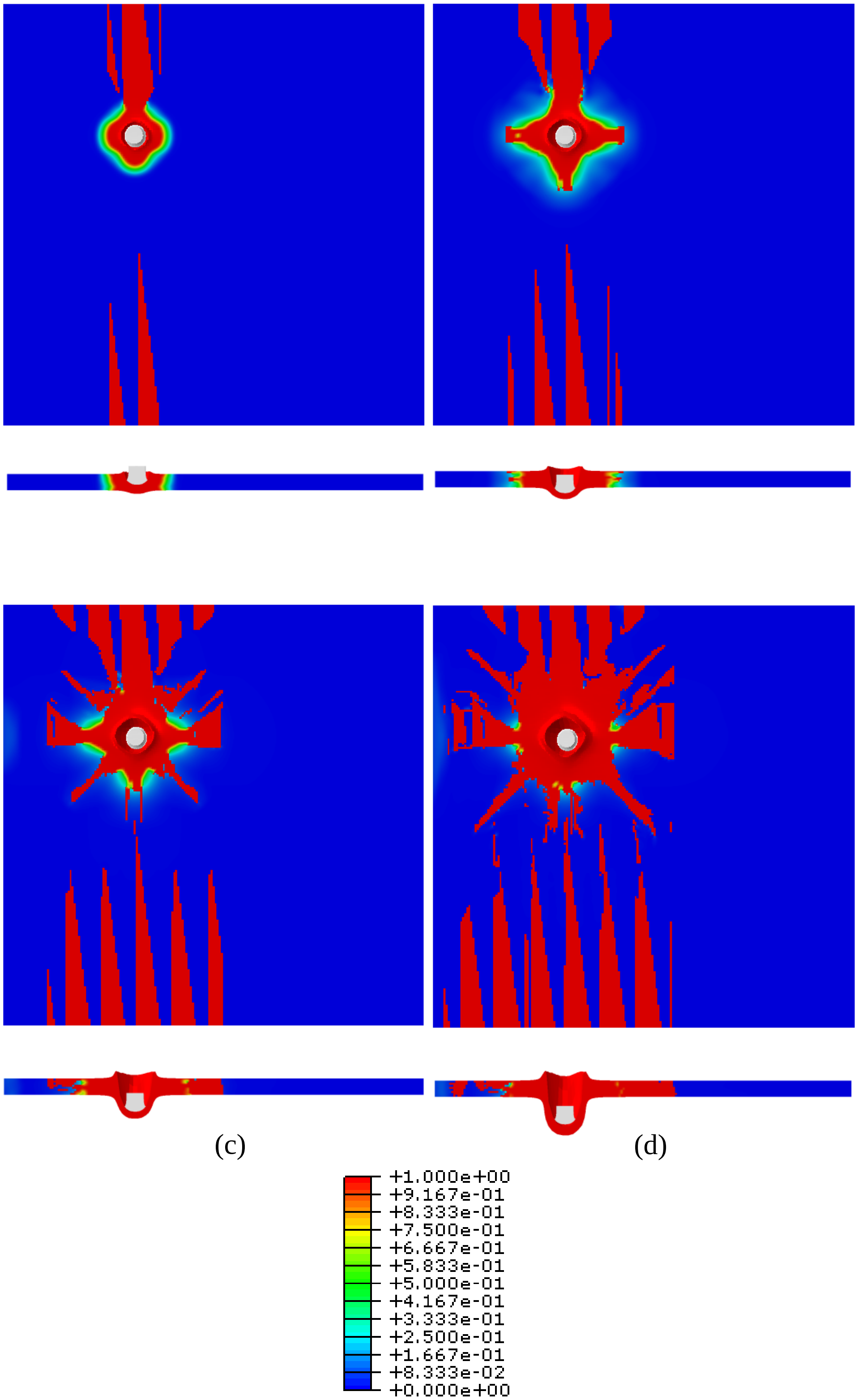

Figure 7.20 FEA simulation of Ashcrete panel with scalar damage parameter at (a) 10 μs, (b) 20 μs, (c) 30 μs, and (d) 40 μs (Eccentric Case)

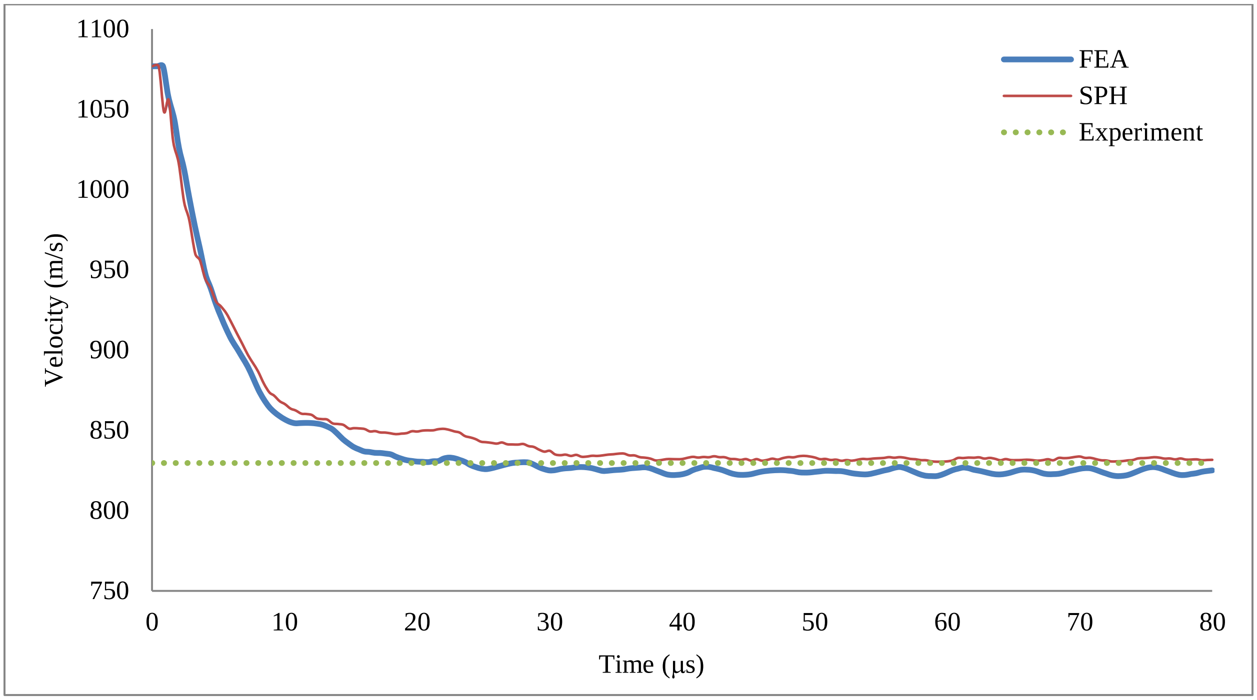

Figure 7.21 Velocity vs. time of Ashcrete FSP models for both FEA and SPH

Figure 7.22 shows the damage pattern in the models, both front (entrance) and back (exit) sides, in comparison with the experiment. It can be seen that the failure pattern in both models show a similar damage behavior. The hole in the panel was slightly larger than the FSP, and a slightly larger crater on the front and back sides. There was peripheral cracking occurring near the supports directly above and below the impact location. It is important to note that the peripheral cracks in both models do not traverse the entire depth of the panel, but rather show several smaller cracks extending through the thickness. The SPH model not only has a more accurate exit velocity for the FSP, but it also has a slightly more concentrated crater. Figure 7.23 shows temporal snapshots, from the impact side as well as the cross section, of damage at time instants of 10, 20, 30, and 40 µs. Figure 7.23(e) shows an isometric view of the panel from the impact side to illustrate that the damage near the bottom periphery of the panel does not traverse the entire depth. Damage of this type is more indicative of smaller cracks.

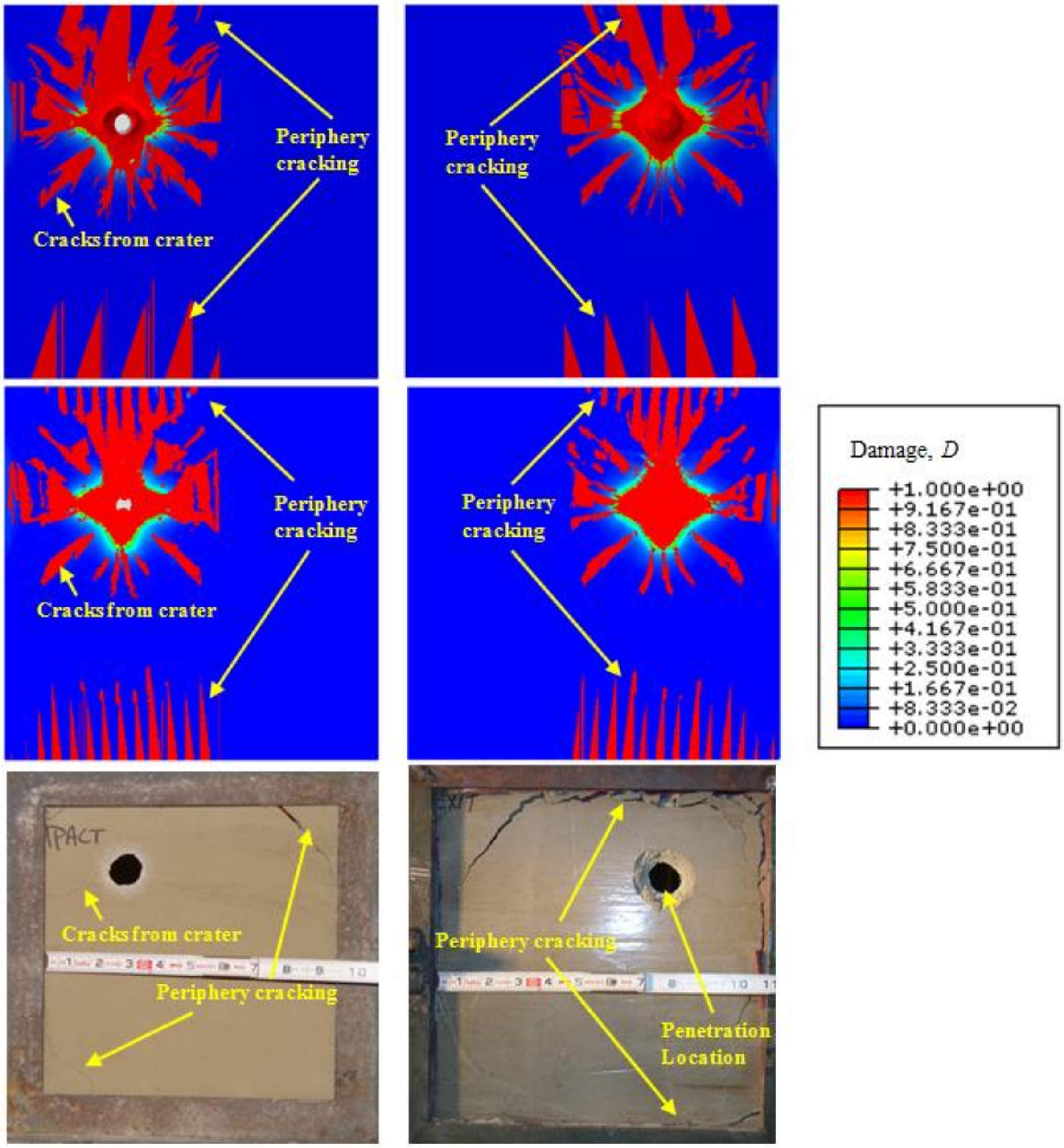

Figure 7.22 Single panel: FEA model (top row), SPH model (middle row), and test panels (bottom row)

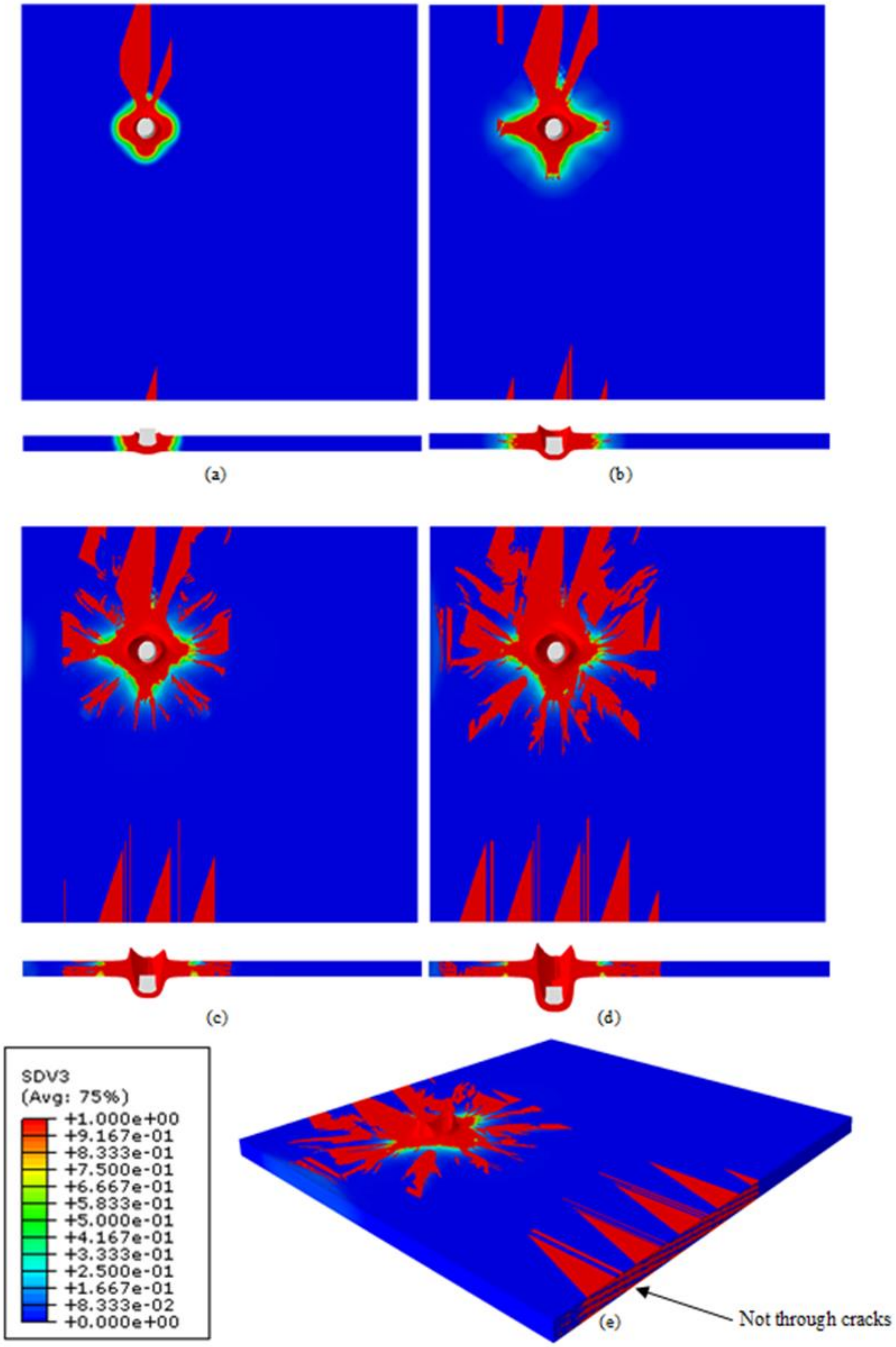

Figure 7.23 Abaqus simulation of Ashcrete panel with scalar damage parameter at at (a) 10 μs, (b) 20 μs, (c) 30 μs, (d) 40 μs, and (e) isometric view at 40 μs (Eccentric Case)

As shown in the FSP simulation, the SPH model has advantage over the FEA model in residual velocity prediction. In addition, an important aspect of modeling high-rate impact of a brittle target is the issue of spalling and fragmentation. It was shown in Section 7.2 that FEA models are good at predicting exit velocities of projectiles if the impact velocity is near the ballistic limit of the target, but without an element deletion scheme, the elements will continue to deform until excessive distortion causes instability in the model. The standard metric for element deletion is effective plastic strain, $\varepsilon_{pl}^{\max}$. The previous article showed that deleting an element when $\varepsilon_{pl}^{\max}$ is below 1.5 (150% strain) causes both inaccuracies in the model as well as large increases in computation time [39]. But a value this large negates the model's ability to show accurate spalling behavior. To illustrate the spalling phenomena, Figure 7.24 compares zoomed-in cross sectional views of both the FEA and SPH single panel models, stepped through time.

The other metric for comparison between these two models is the propagation of a compressive (and subsequently, tensile) shock wave. This phenomena is better seen through time in the single panel case due to the highly localized damage pattern (stress cannot pass through fully damaged elements/particles). Figure 7.25 shows the von Mises stress contours through time on the entrance side of single panel models. For easier viewing, only stress values between zero and 150 MPa are shown since much higher stress states are reached in the much stiffer FSP.

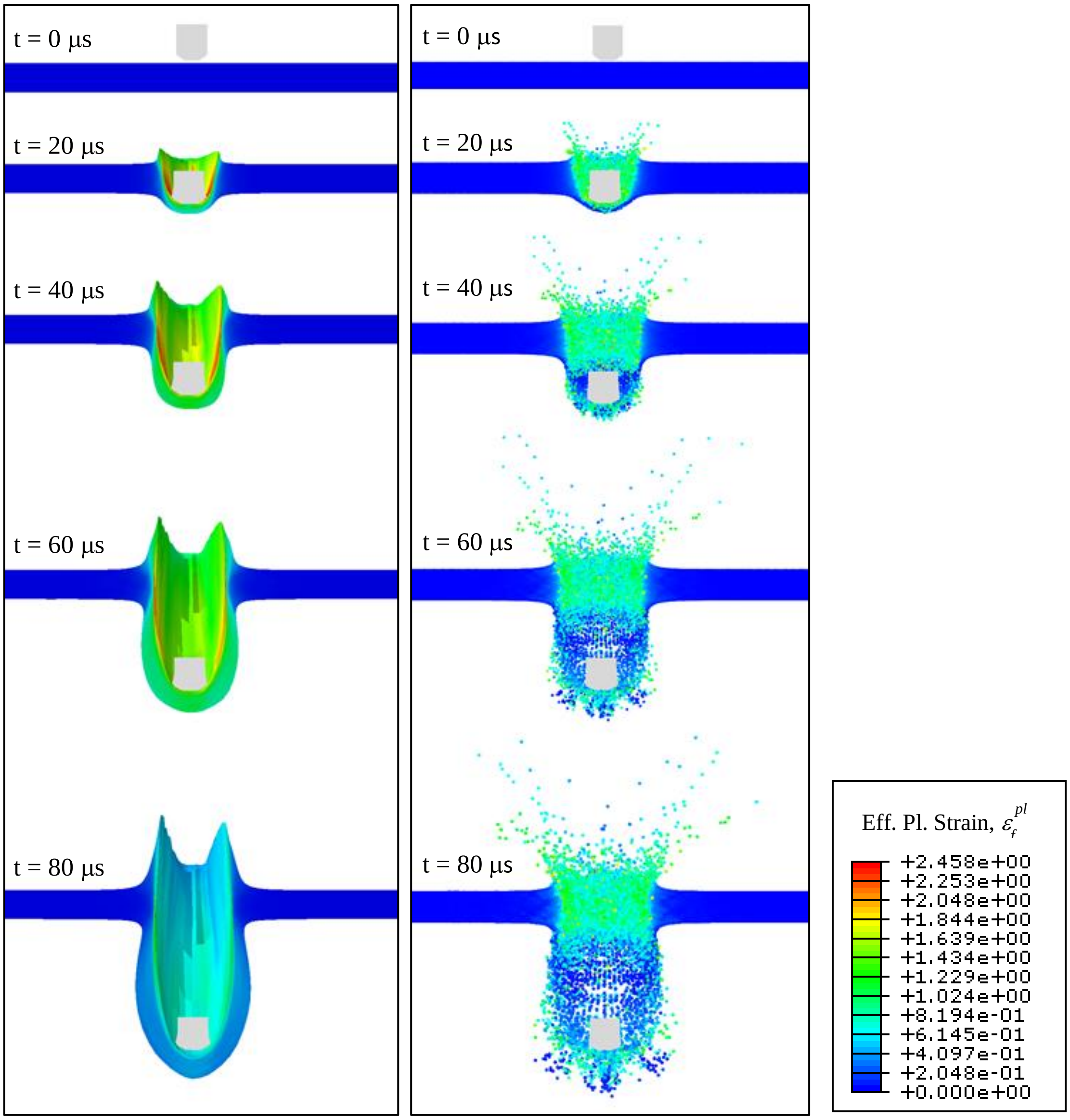

Figure 7.24 Cross section of Ashcrete panel showing effective plastic strain for both FEA (left) and SPH (right) through time

As illustrated, both models perform well in predicting the regions of largest effective plastic strain, but only the SPH model can handle the transition of particles from being part of the original target to being free flying fragments. As shown in the FEA model in Figure 7.24, at around 80 μs much higher plastic strains develop in the target elements surrounding the projectile. An element deletion scheme can handle this issue, but it still will not give results as seen in the SPH models. This behavior becomes even more pronounced in the stacked panel case. While the SPH model does show an appropriate fragmentation and spalled behavior, some local grouping of particles near the rear free surface was observed. This may be a result of the presence of tensile instability noted in SPH formulations. In addition to accuracy, there is also the issue of computation time. While the FEA simulation took 8 hours, 11 minutes, and 27 seconds to run, the SPH simulation took 20 hours, 10 minutes, and 48 seconds to complete. Like the UHSC-1 simulations in Section 7.2, SPH shows a significant increase in computation cost over traditional FEA.

Figure 7.27 gives an overall comparison of all the Ashcrete FSP experiments compared to the FEA and SPH models. Note that the impact velocities are over a range of only 50 m/s.

An additional study was undertaken to see the effects of boundary conditions on the local and global damage responses. Since the experimental panels were clamped at the periphery and part of the clamp material overlaps the plate by about 0.5” in the front and back at the panel edges (as seen in Figure 7.13), the model shown in Figure 7.18 was analyzed again by simulating this boundary condition. This essentially caused no change in the residual velocity and local damage pattern, though the computation time did increase by over 20%. However, the secondary or global damage away from the area of impact closely resembled the experimental results, with much less damage occurring at the periphery, mostly in the form of smaller surface cracks. Figure 7.26 shows the front, back, cross-section, and isometric views of the damage at 40 μs (as in Figure 7.23(d) and (e)).

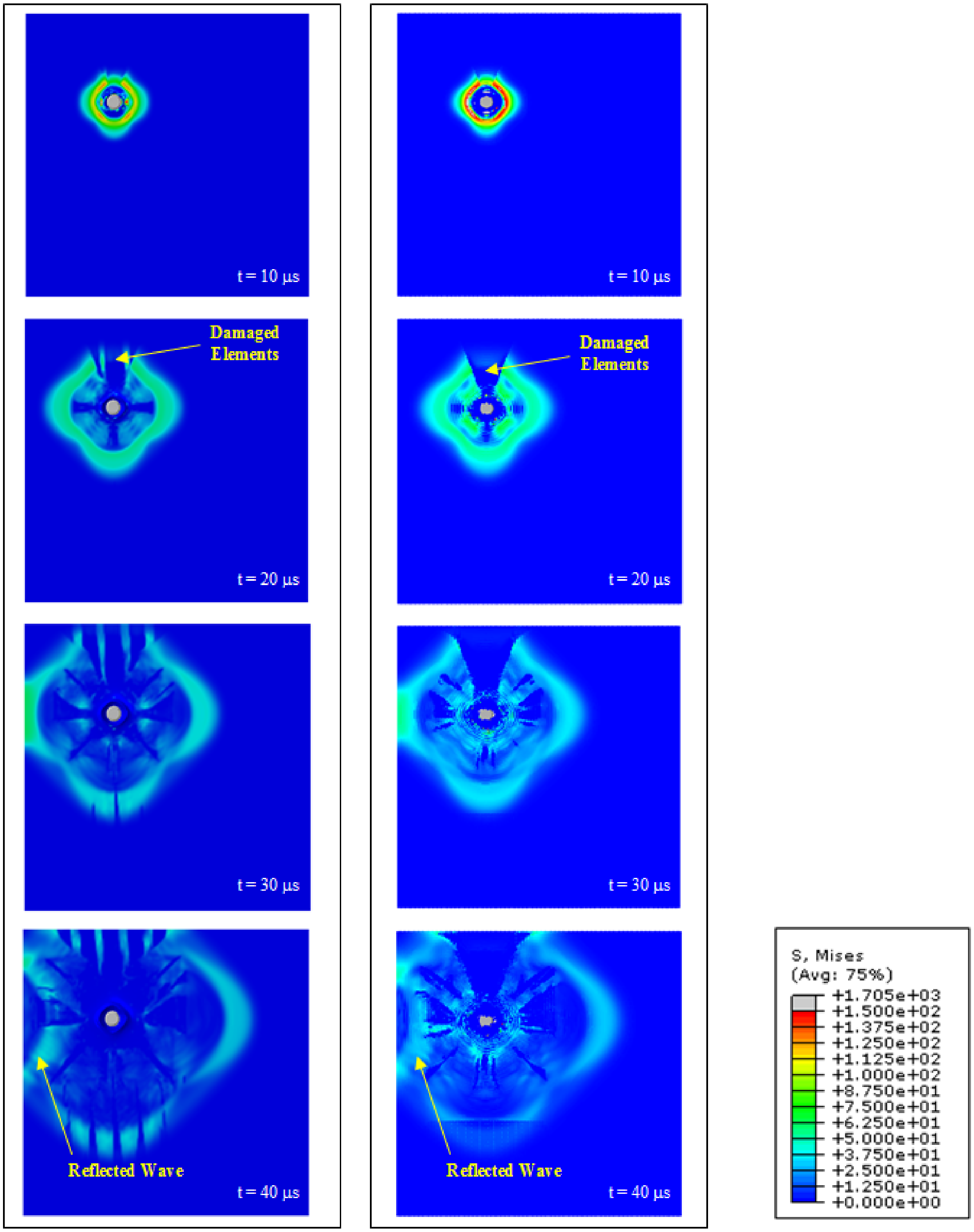

Figure 7.25 Stress contours of single Ashcrete panel models, FEA (left) and SPH (right) through time

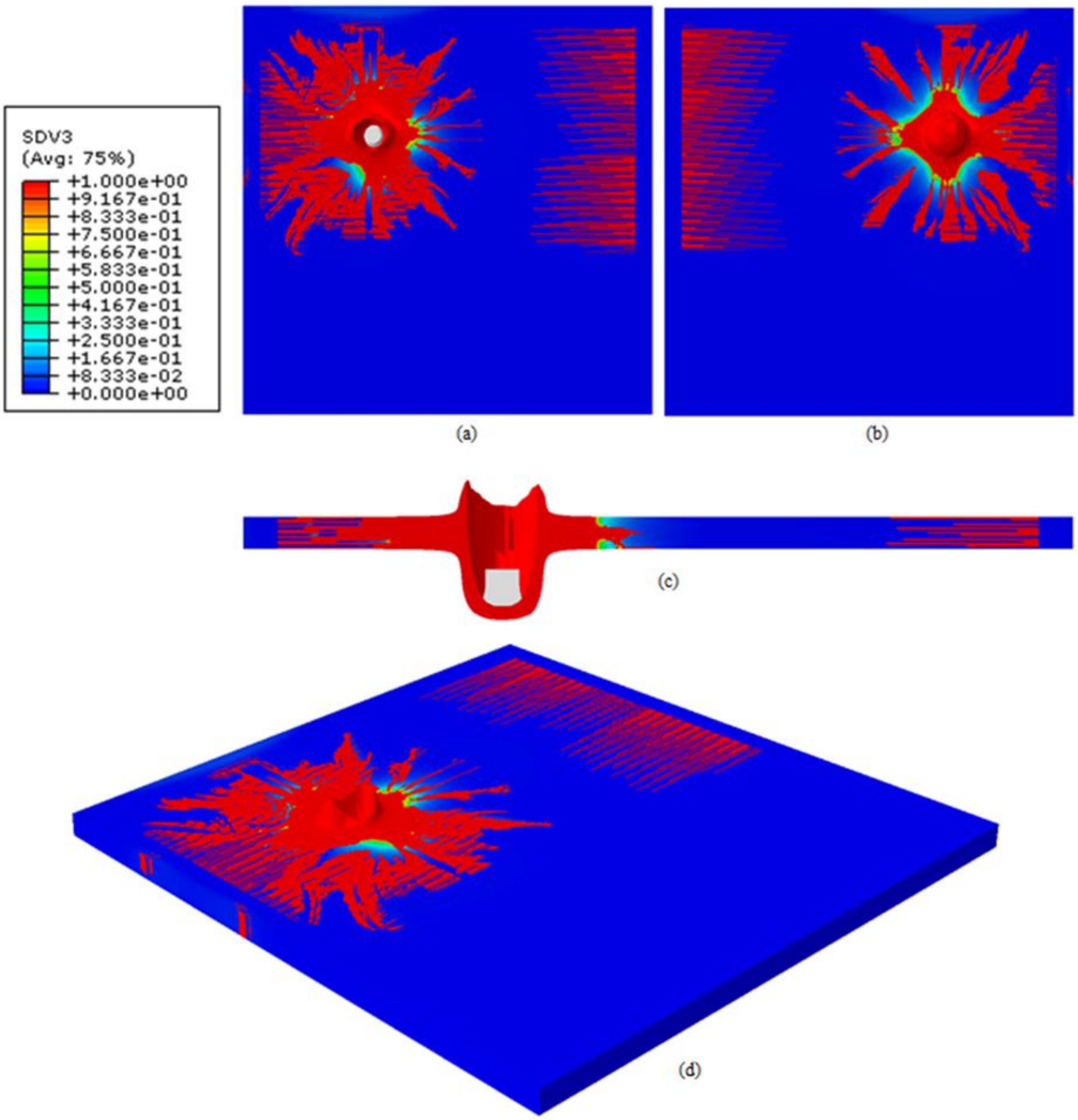

Figure 7.26 Abaqus simulation of Ashcrete panel with scalar damage parameter at 40 μs (a) front view, (b) back view, (c) cross sectional view, and (d) isometric view (clamped boundary condition)

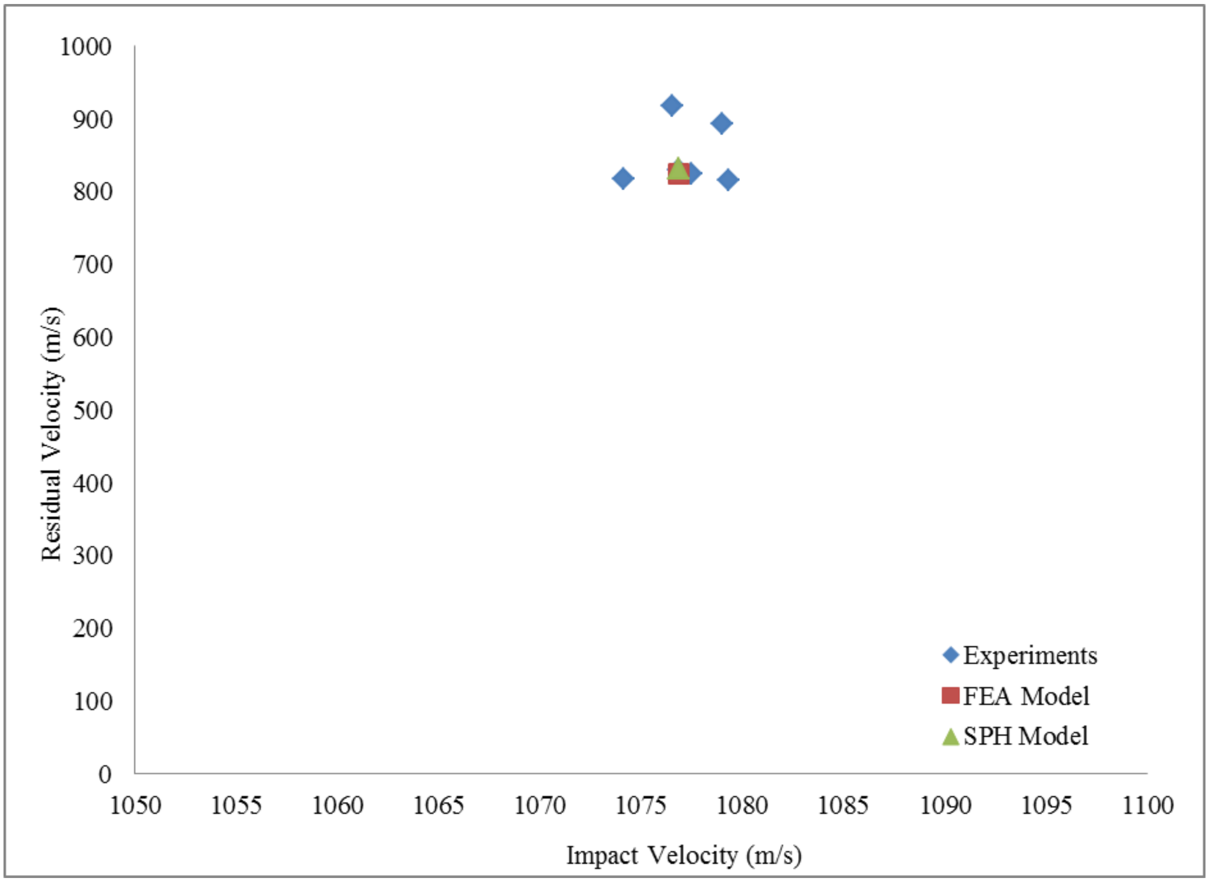

Figure 7.27 Impact vs. residual velocity of single panel Ashcrete FSP experiment and models

7.4 Application of Model to Stacked Panels

A more complex problem to solve is the case in which two of the panels simulated in Section 7.3 are stacked back to back. This is a very important problem for the military since force protection can be greatly increased by stacking armor panels. In this section, two Ashcrete panels were stacked back to back and simulated at an impact velocity of 1074 m/s, fired eccentrically as in the previous example. FEA and SPH models are built, analyzed, and compared. Both models are identical in assembly, boundary conditions, and material properties. However, due to the memory constraints on the available computers, the SPH model could not attain a similar mesh refinement. Due to the smoothing length calculations required by SPH, an incredibly large amount of computer memory is required to complete these analyses. For the FEA model, 4,645,152 elements were used while the SPH model could only achieve a mesh refinement of 1,561,184 elements. For the SPH model, all elements were converted to particles prior to running the model. Figure 7.28 shows the assembly and mesh of the model, with a zoomed-in view to see the projectile and stacked assembly of the panels. To ensure that no problems ensued in the SPH model as a result of the particles in contact with each other from opposing panels occupying the same 3D space, the panels were placed a distance of 0.75 mm apart, which corresponds to the characteristic length of the particles. For consistency, the FEA model also had a gap of 0.75 mm between the two target panels.

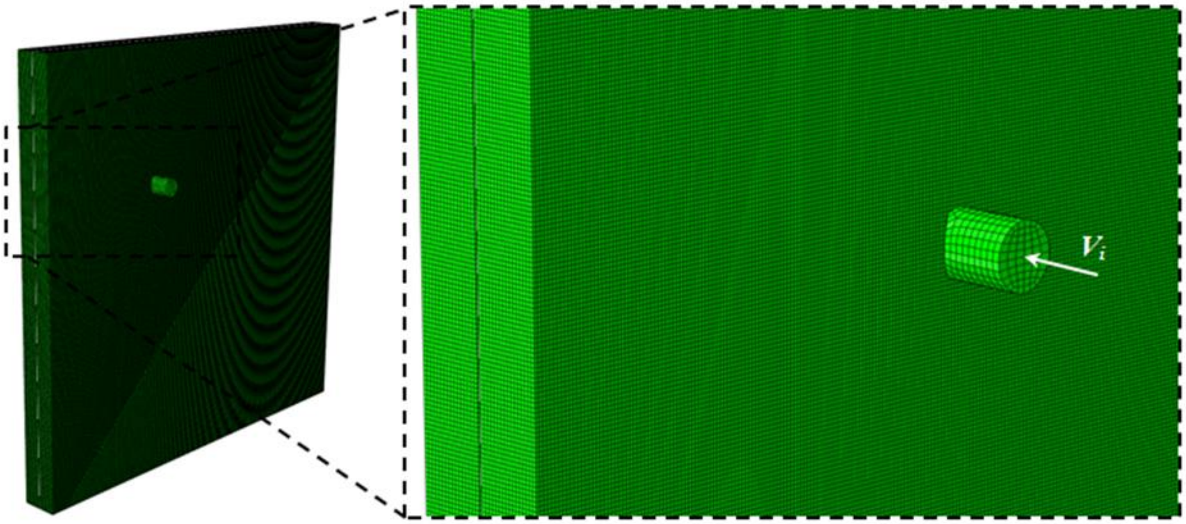

Figure 7.28 Assembly and mesh of Ashcrete FSP stacked model

A number of such pairs of test panels were shot and the models are compared to the average result of the tests. Similar to the results in Section 7.3, the same two metrics are used in comparing the performance of the two models with the experimental result. The average exit velocity seen in the experiments was 637 m/s. The exit velocity seen in the FEA model was 539 m/s and the exit velocity in the SPH model was 540 m/s. These values have an error that is 15.5% off and 15.4% off of the average experimental value, respectively. The velocity histories of both models are compared in Figure 7.29 with the baseline experimental average shown by the dotted line.

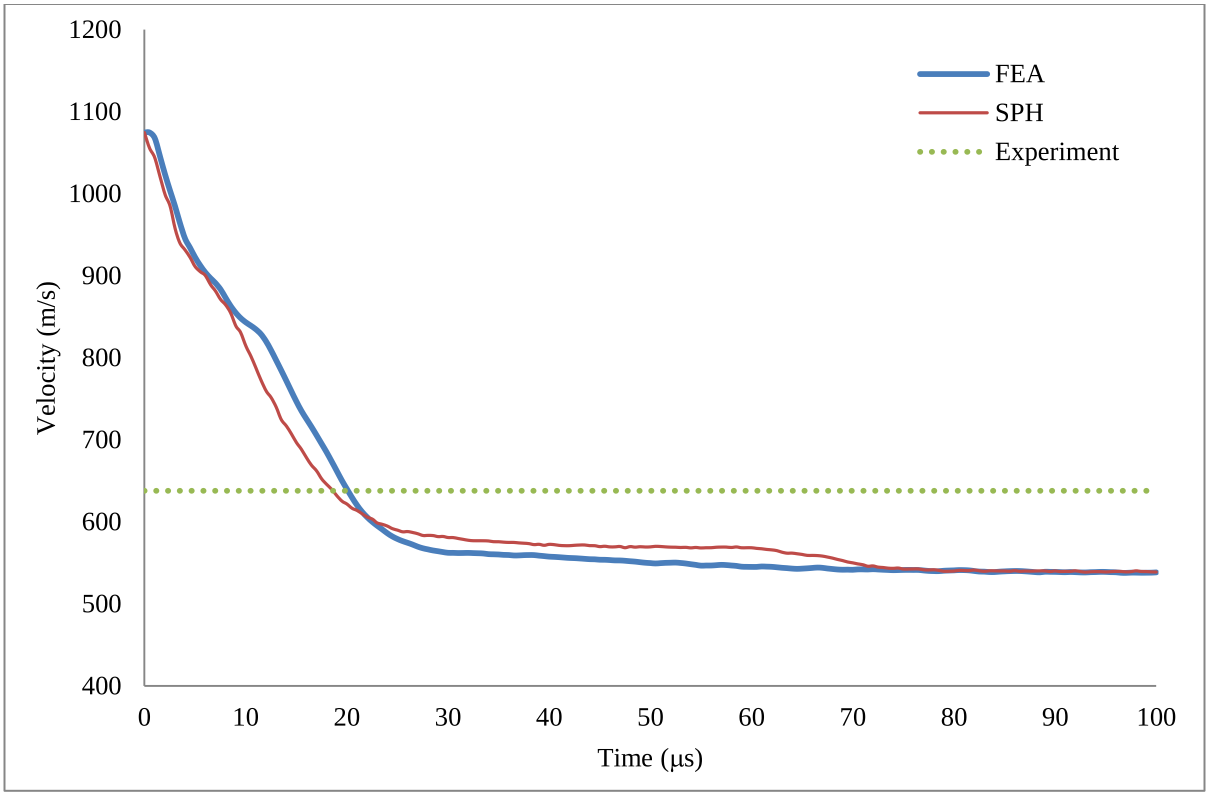

Figure 7.29 Velocity vs. time for FEA and SPH models compared to experiment (stacked panels)

Figure 7.30 shows the damage pattern in the models of the stacked panels, both the front (entrance) and back (exit), as compared to the experiment. It can be seen that the failure pattern in both models show a large amount of damage in the corner of the panel close to where the projectile hit. The experiment indicates not only a large damaged region, but long cracks that traverse the entire panel to the periphery in every direction. Because of the large amount of damage both near the region of impact and at the periphery, it is difficult to directly compare the two models purely based on damage, *D*. Based on the FSP residual velocity, the SPH model seems to show similar accuracy to that of the FEA model, however the cap on computer memory has truncated the mesh refinement and therefore it can be theorized that with an appropriate particle size, the SPH model would indeed give superior results over the FEA model.

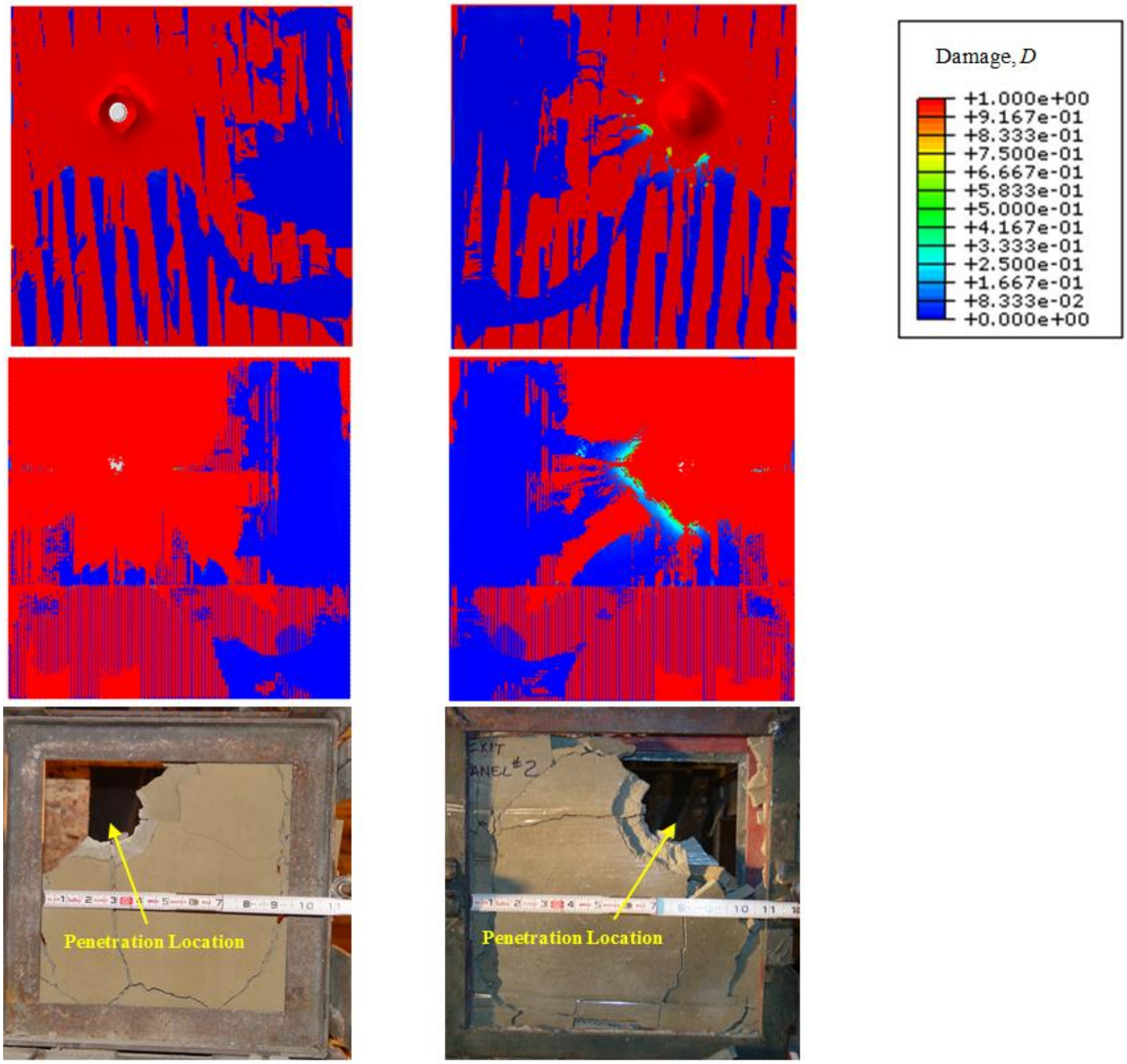

Figure 7.30 Stacked panels: FEA model (top row), SPH model (middle row), and test panels (bottom row)

Similar to the comparison of FEA and SPH for the single panel case as shown in Figure 7.24, a direct comparison of the effective plastic strain contours through the zoomed-in cross section of both the models, stepped through time, is shown in Figure 7.31.

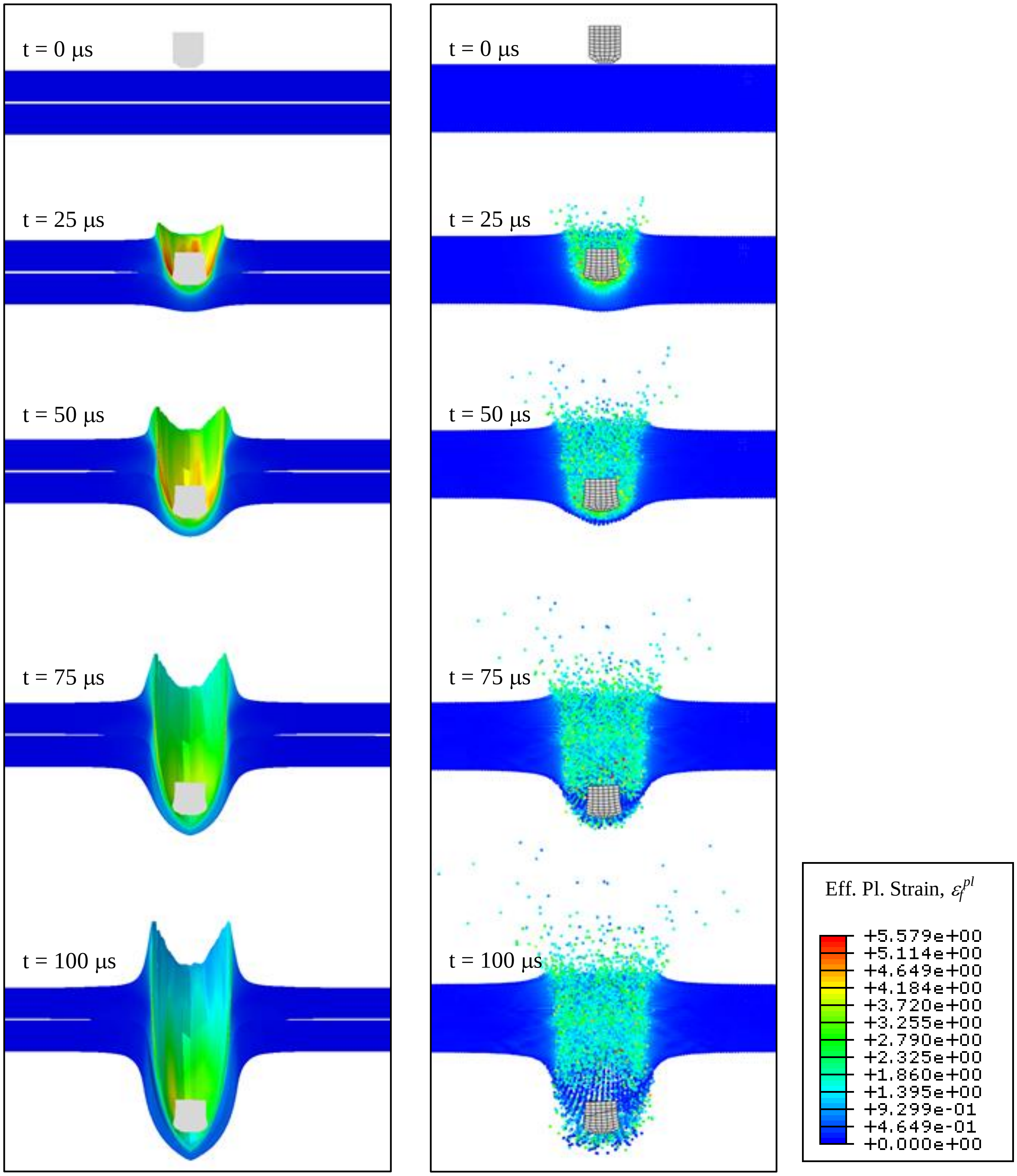

Figure 7.31 Cross section of stacked panels showing effective plastic strain for both FEA (left) and SPH (right) through time

As was seen in Section 7.3, there was a distinct difference in analysis time between the FEA model and the SPH model. Since the number of degrees of freedom for the stacked case nearly doubled (only for the FEA model), the analysis time is expected to increase. For the FEA model, the analysis time was 31 hours, 23 minutes, and

19 seconds. For the SPH model, the analysis time was 19 hours, 32 minutes, 59 seconds. So for all model scenarios outlined in sections 7.2 and 7.3, the SPH models took more than 4.5 times the computation time than the comparable FEA model. This comparison could not be made for the stacked panel FSP test since different mesh refinements were used. A summary of all the model analyses times and degrees of freedom are summarized in Table 7.3.

Table 7.3 Computation time and size of all models

			Analysis Time	DOFs	
Model	Panel Material	Projectile Material	(HH:MM:SS)	Panel	Projectile
Ballistic Limit Test (FEA)	UHSC-1	S2 Tool Steel	00:22:21	187,272	848
Ballistic Limit Test (SPH)	UHSC-1	S2 Tool Steel	01:40:20	187,272	848
Single Panel FSP Test (FEA)	Ashcrete	4340-H Steel	08:11:27	2,177,415	584
Single Panel FSP Test (SPH)	Ashcrete	4340-H Steel	20:10:48	2,177,415	584
Stacked Panel FSP Test (FEA)	Ashcrete	4340-H Steel	31:23:19	4,645,152	584
Stacked Panel FSP Test (SPH)	Ashcrete	4340-H Steel	19:32:59	1,561,184	584

Another major difference noted in the performance of the two model types is the deformation of the FSP. Though the projectiles go through relatively little permanent deformation (given the extremely high rate of impact), the deformed shape between the two models are very distinct. Figure 7.32 shows the undeformed and deformed shapes of the FSP for the FEA and SPH stacked models. As seen by the FSP on the left, the FEA model seems to give a more smoothed deformed shape, while the SPH model causes jagged edges on the projectile nose, likely caused by the nature of contact experienced between the regular finite elements of the FSP and the particles of the target. This difference in the failure pattern of the projectile may be responsible for the difference in residual velocity, since permanent plastic strain in the projectile is a form of dissipation of kinetic energy. It can be expected that, since the prediction of residual velocity decreased in accuracy from the single panel case to the stacked panel case, additional decrease in accuracy can be expected in simulations involving more stacked panels. Figure 7.33 gives an overall comparison of all the stacked panel Ashcrete FSP experiments and the FEA and SPH model predictions. Note that the impact velocities are clustered over an interval of 50 m/s only. A summary of results for all the impact models is shown in Table 7.4.

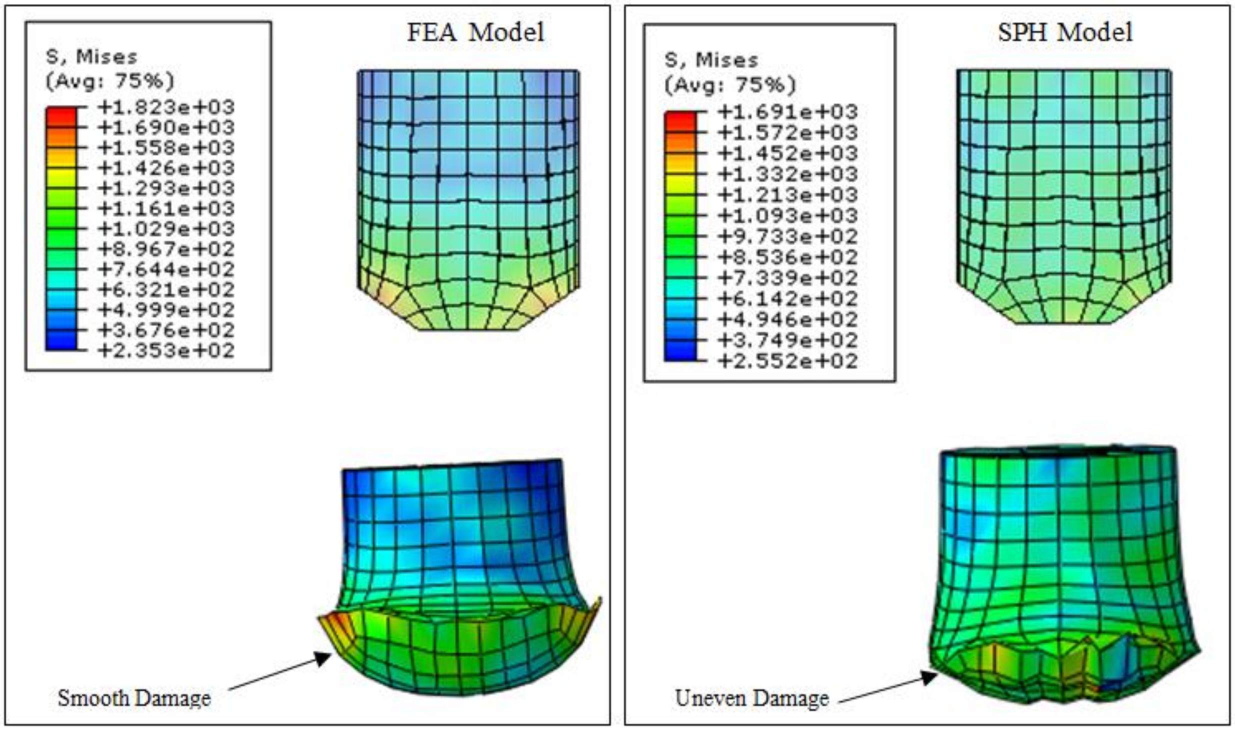

Figure 7.32 FSP before (top) and after (bottom) impact of ASHCRETE panels

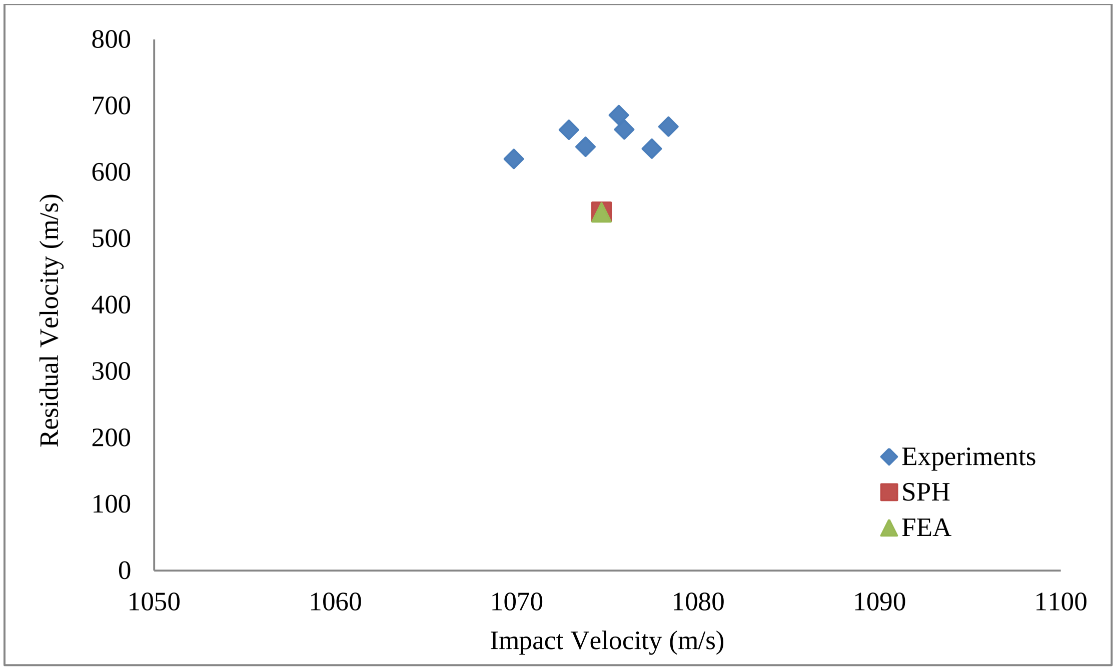

Figure 7.33 Impact vs. residual velocity of stacked panel Ashcrete FSP experiment and models

Table 7.4 Summary of impact models and experiments

Test	Panel Material	Impact Velocity (m/s)	Exit Velocity (m/s)		
			Exp. (Average)	FEA	SPH
Ballistic Limit Test	UHSC-1	483	88	92	138
Single Panel FSP Test	Ashcrete	1076.8	829	824	832
Stacked Panel FSP Test	Ashcrete	1074	637	539	540

The last impact scenario considered is that of two stacked panels that are not back to back, but separated by some distance. The idea of separating panels is to allow the fragmented particles from the first panel to disperse and spread their impact energy over the surface of the second panel. This will cause much more widespread damage, but ultimately should decrease the residual velocity of the projectile more. Since this problem is highly dependent on both fragmentation as well as secondary impact, only SPH is used for the simulation. In this scenario, two 1-inch thick Ashcrete panels are separated by a distance of 12 inches. The same FSP as in the previous example has an initial velocity of 1076.8 m/s at an impact orientation normal to the face of the panel and the panels are assumed to be fixed at the periphery. To achieve a similar mesh density as the previous stacked panel case while minimizing computation time, quarter symmetry was utilized. The model used a total of 383,319 degrees of freedom and was analyzed over a total time of 1.0 msec.

Figure 7.34 shows a cross sectional view of the model over increments of time throughout the impact event. The figure shows a highly localized damaged region during the penetration of the first panel, but the dispersion of the fragmented particles causes majority of the second panel to be damaged in the second penetration event. The total analysis time for this run was 59 hours, 54 minutes, 51 seconds. The drastic increase in computation time is due to the significantly larger total time (1000 μsec) over the previous SPH models (100 μsec). This increase in time was needed in order to track all the fragmented particles through empty space prior to the secondary impact. The velocity of the FSP over time is shown in Figure 7.35. The graph shows an initial residual velocity of 458 m/s after penetration of the first panel and a final residual velocity of 152 m/s after impact of the second panel.

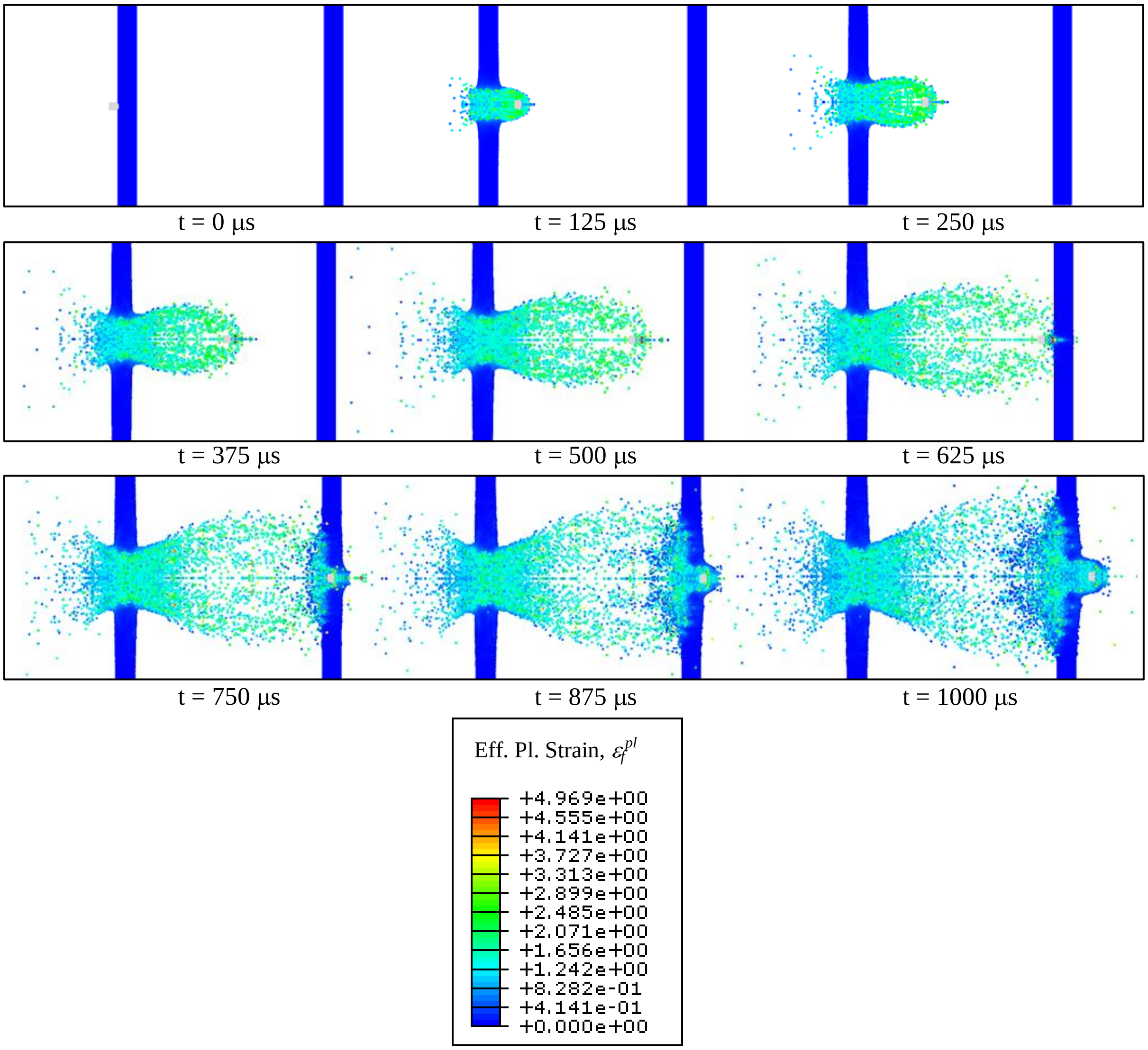
t = 0 µs

t = 125 µs

t = 250 µs

t = 375 µs

t = 500 µs

t = 625 µs

t = 750 µs

t = 875 µs

t = 1000 µs

Figure 7.34 Stacked panel simulation at 12-inch separation through increments of time

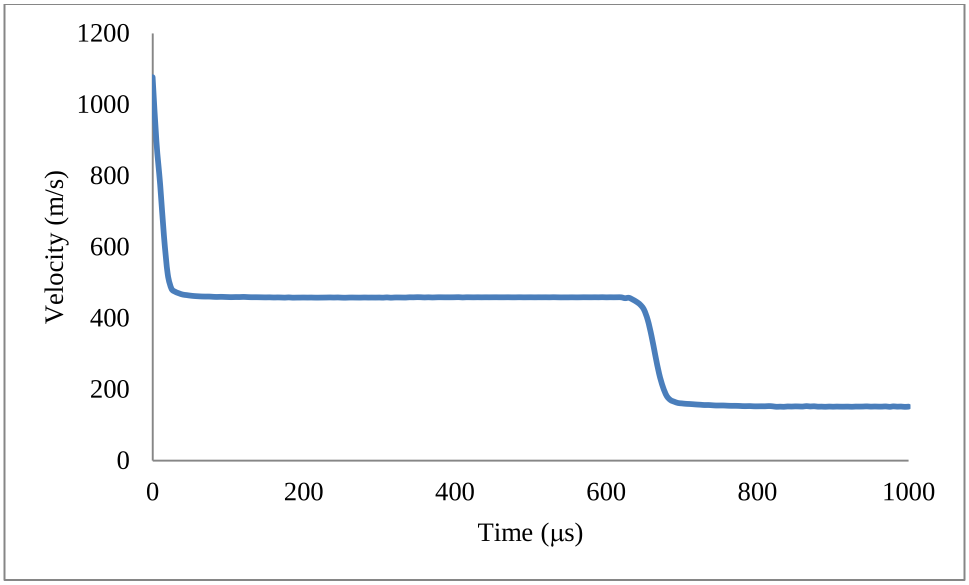

Figure 7.35 Velocity vs. time of stacked panel simulation at 12-inch separation

7.5 Conclusions

The robust and efficient constitutive model proposed in Chapter 4 and implemented in Chapter 5 has been successfully applied and validated against several actual ballistic impact experiments. Based on the findings in Sections 7.2-7.4, the following conclusions can be drawn:

[1] When simulating UHSC-1, an FEA model is significantly better at predicting the exit velocity of the projectile. This may be due to the fact that it is close to the ballistic limit of the panel

[2] For simulating Ashcrete, the SPH model seems to be slightly better at predicting the exit velocity of the projectile impacting a single panel.

[3] For simulating Ashcrete, an SPH model is definitely better at predicting the exit velocity of the projectile impacting stacked panels, but it can be assumed that based on the mesh convergence study illustrated in Figure 7.17, a more refined mesh for the SPH model would likely improve the solution significantly.

[4] Conclusions (*2*) and (*3*) may be attributed to the fact that the velocities simulated are significantly higher than the ballistic limit, which supports the theory that SPH is not as accurate for lower values of strains, as would be seen in lower velocity impact range.

[5] SPH models are significantly more computationally expensive than FEA models.

[6] SPH models can simulate fragmentation of brittle armor panels very realistically

[7] The same material model works seamlessly for both FEA and SPH models

[8] Predicted damage patterns agree with test results very well

Chapter 8

Multi-Scale Treatment of the Ductility of Short-Fiber Reinforcement

8.1 Introduction

The armor panels described and analyzed in Chapter 7 are undergoing continuous refinement to ensure that they are lightweight, inexpensive to manufacture, rapidly deployable, and capable of providing effective protection against bomb blast and projectile impact. An important recent improvement to the cementitious armor panel system is the addition of short-fiber reinforcement to improve the ductility of the panels, leading to enhanced energy dissipation capacity under impact and shock loads. The matrix material in the panels is still UHSC, enabling the attainment of high compressive strength in a matter of days. Short fiber-reinforced UHSC is a composite material of two components: matrix and short fibers. The matrix material is brittle, whereas the fiber component can be a ductile, high modulus material such as steel, or a ductile, low modulus material such as polypropylene. The choice of fiber material and geometry (i.e. fiber length, diameter, and surface treatment) is based primarily on the fiber-matrix interaction that will yield the highest overall ductility in the composite. The yield and failure strain of the various fibers is invariably greater than the yield and failure strain of the matrix material. As a crack appears in the matrix, short fibers are pulled out after progressive bond failure. Longer fibers or fibers of low strength would break instead. In either case, fibers serve as crack bridges and arrestors. The volume of fibers will typically range from 0.5 to three percent by volume of the matrix [15].

To reduce the cost while maximizing efficiency, the reinforcing short fibers are simply added to the matrix mixture before casting the panels, and therefore, the fibers would be randomly dispersed and oriented. Since fibers typically used range in length from 1-1.5 inches (which is often more than the panel thickness), it is expected that local constitutive properties over a panel would vary depending on fiber distribution and orientations. This leads to the conclusion that the traditional approach of using a representative volume element (RVE) for homogenization would not be appropriate due to the lack of any periodicity. Because of this, an alternative approach is followed in this study, as discussed in Section 8.4.

8.2 Nature of Matrix-Fiber Bond Interaction

In fiber-reinforced composite problems, the most influential parameters are the fiber material (typically, steel or polypropylene), fiber geometry (length, diameter, surface treatments, if any), matrix material properties, interfacial bond characteristics between fiber and matrix, fiber locations or distributions, fiber orientations, and total volume percentage of fibers in the composite. The respective material properties of fiber and matrix, coupled with the bond behavior between the two have been challenging issued for recent researchers.

In modeling the interfacial bond between the reinforcing fibers and the cementitious matrix, the consideration for surface-based cohesive interactions between the two phases are essential. These interactions are intended for bonded interfaces with negligibly small interface thickness, as in the present case. These surface-based interactions use a traction-separation behavior, based on a pure master-slave formulation where constraints are enforced at the slave nodes, and do not add mass to the model (as element-based cohesive interactions would). Surface-based cohesion uses what is called a “bond-link” element, first proposed by Ngo and Scordelis (1967) who were the earliest publishers on the application of the finite element method to the analysis of reinforced concrete structures [36]. To account for the bond-slip behavior of reinforcing steel, these bond-link elements are placed between the adjacent nodes of matrix and fiber [27]. This link has no physical dimensions; therefore two connected nodes would occupy the same coordinates. These bond-links constitute three, fictitious orthogonal spring elements connecting adjacent nodes and transmitting shear and normal forces between the two phases, that is, fibers and matrix. In addition to cohesive behavior, which is linearly elastic, the damage evolution of the bond is specified as well.

A contact pair formulation was used to identify all the internal surfaces in the composite (i.e. the surfaces of the fibers in contact with the corresponding matrix surface). For simulating the interaction with an elastic bond behavior as well as a degraded post-failure behavior, the model uses a traction-separation behavior that is initially linearly elastic, followed by the initiation and evolution of damage. The initial elastic behavior is written in terms of an elastic constitutive matrix that relates the normal and shear stresses to normal and shear separations across the interface. The nominal traction stress vector $\vec{t}$ consists of three components in a three-dimensional model: t_n, t_s, and t_t which represent the normal and the two shear tractions, respectively. The corresponding separations are denoted by δ_n, δ_s, and δ_t. Such elastic behavior can be summarized by the equation

$$\bar{t} = \begin{Bmatrix} t_n \\ t_s \\ t_t \end{Bmatrix} = \begin{bmatrix} K_{nn} & K_{ns} & K_{nt} \\ K_{ns} & K_{ss} & K_{st} \\ K_{nt} & K_{st} & K_{tt} \end{bmatrix} \begin{Bmatrix} \delta_n \\ \delta_s \\ \delta_t \end{Bmatrix} = \vec{K}\vec{\delta}, \tag{8.1}$$

where K_{nn}, K_{ss}, and K_{tt} are the elastic stiffness values assigned to the normal, and local 1- and 2- direction fictitious shear springs, respectively. Due to the uncoupled traction-separation behavior, the $\vec{K}$ matrix in Eq. (8.1) simplifies to a diagonal matrix.

At some point during the fiber pullout process, the bond begins to fail. Damage modeling allows the simulation of the associated progressive degradation process and eventual failure of the bond. This failure mechanism consists of the damage initiation criterion and a damage evolution law. The bond response prior to failure is linear, as discussed above. But once the damage initiation criterion is met, damage evolves according to a user-defined law. Damage initiation refers to the beginning of degradation of the cohesive response at a contact point. For the models presented, degradation begins when contact separation satisfies the criteria specified. Figure 8.1 shows the full behavior of the bond from elastic stage to damage initiation, to damage evolution, and culmination to total bond failure.

The damage evolution law, which governs the rate at which the cohesive stiffness is degraded, gets mobilized after the corresponding initiation criterion has been reached. During this process, a scalar damage variable, *D*, represents the overall damage at an interfacial contact point. Initially, *D* has a value of 0, which monotonically evolves from 0 to 1 on further loading after the initiation of damage [6]. The contact stress components, $\bar{t}_n, \bar{t}_s$, and $\bar{t}_t$ are affected by the damage according to:

$$
\begin{aligned}
t_n &= \begin{cases} (1-D)\bar{t}_n, \bar{t}_n \geq 0 \\ \bar{t}_n, \qquad \qquad \textit{otherwise} \end{cases} \\
t_s &= (1-D)\bar{t}_s, \\
t_t &= (1-D)\bar{t}_t.
\end{aligned}
\tag{8.2}
$$

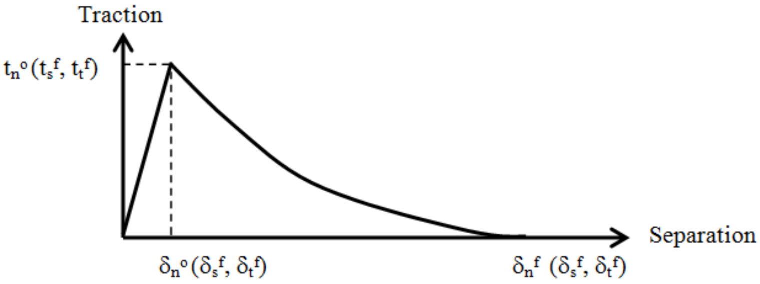

Figure 8.1 Typical traction-separation response of cohesive bond with nonlinear damage evolution

In the experiment conducted at ERDC, bunched polypropylene fibers were selected and one example of which is shown in Figure 8.2. The matrix material used was Ashcrete and no more than 2% fibers by volume were used. To properly characterize the fiber and bond behavior of one such fiber cast in Ashcrete, single fiber direct tension tests and single fiber pullout tests (at various embedment lengths) were undertaken at ERDC. A view of the single fiber pullout test is shown in Figure 8.3 and the results of the direct tension and pullout tests are shown in Figure 8.4.

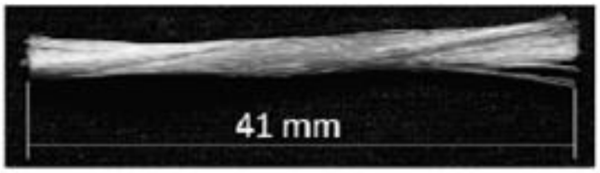

Figure 8.2 Bundled polypropylene fiber [16]

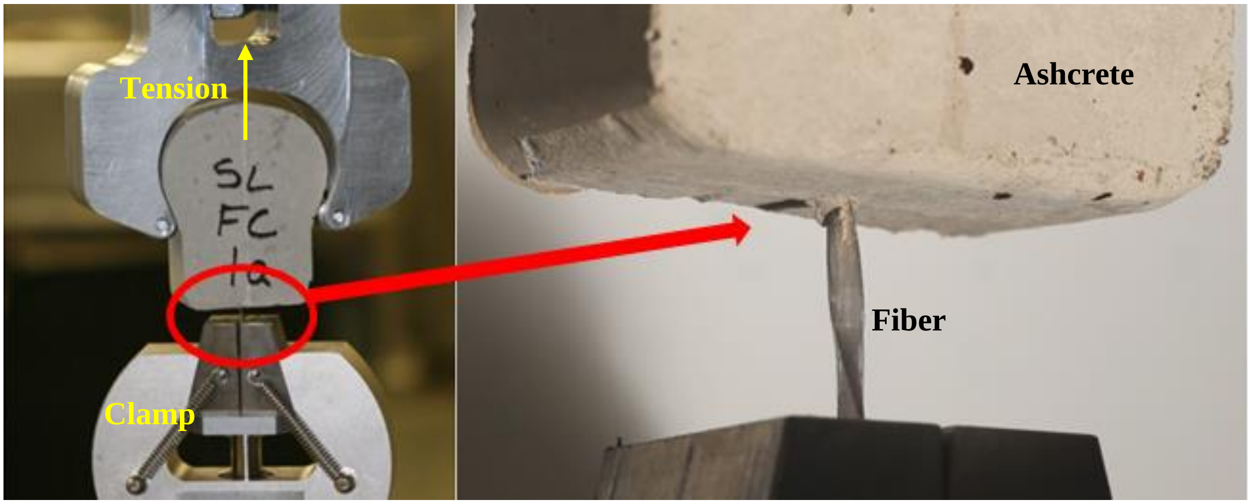

Figure 8.3 Single fiber pullout test of polypropylene bundled fiber embedded in Ashcrete

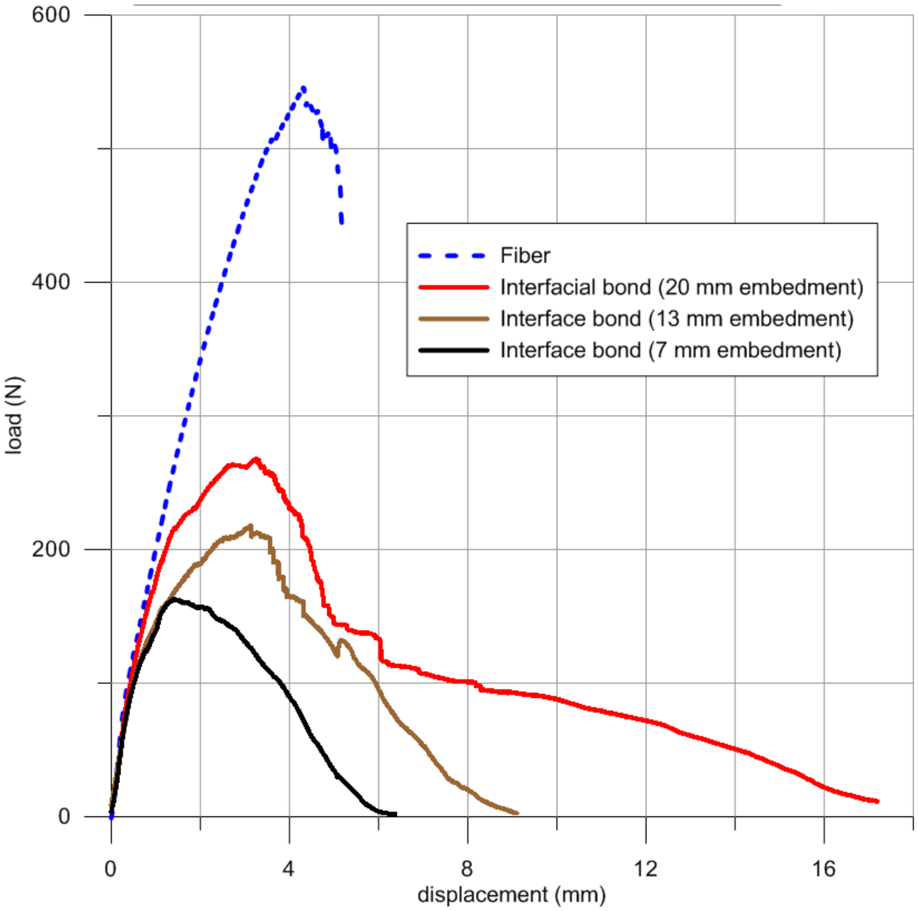

Figure 8.4 Single fiber tension test and single fiber pullout tests for various embedment lengths [16]

The results of fiber pullout test given in Figure 8.4 for embedment depths of 7 mm to 20 mm suggest that the post-failure criterion did not show linear damage evolution. Therefore, damage evolution is based on the experimental data, and the value of the damage parameter D is defined by the following relationship

$$D = 1 - \left\{ \frac{\delta_m^o}{\delta_m^{\max}} \right\} \left\{ 1 - \frac{1 - \exp\left(-\alpha \left(\frac{\delta_m^{\max} - \delta_m^o}{\delta_m^f - \delta_m^o} \right) \right)}{1 - \exp(-\alpha)} \right\} \tag{8.3}$$

where α is a non-dimensional parameter that defines the rate of damage evolution, δ_m^f is the effective separation at complete failure, δ_m^o is the effective separation at damage initiation, $\delta_m^{\max}$ is the maximum value of the effective separation attained during the loading history [47].

An additional facet to the bond behavior is that of mode-mix failure. Due to the random orientations of the reinforcing fibers, the load transfer mechanisms are always likely to be in some combination of shear (in two tangential directions) and normal forces. During simulations, the relative proportions of normal and shear separations at a contact point define the mode mix at that point. The form of mode mix measurement used in this study, as in the cases of damage initiation and total failure, is based on traction components. The definitions of the mode mix based on these traction components are

$$\begin{aligned} \phi_1 &= \left(\frac{2}{\pi} \right) \tan^{-1} \left(\frac{\sqrt{t_s^2 + t_t^2}}{\langle t_n \rangle} \right), \\ \phi_2 &= \left(\frac{2}{\pi} \right) \tan^{-1} \left(\frac{t_t}{t_s} \right), \end{aligned} \tag{8.4}$$

where $(2/\pi)$ is an angular normalizing factor. The angular measures ϕ_1 and ϕ_2 are illustrated in Figure 8.5.

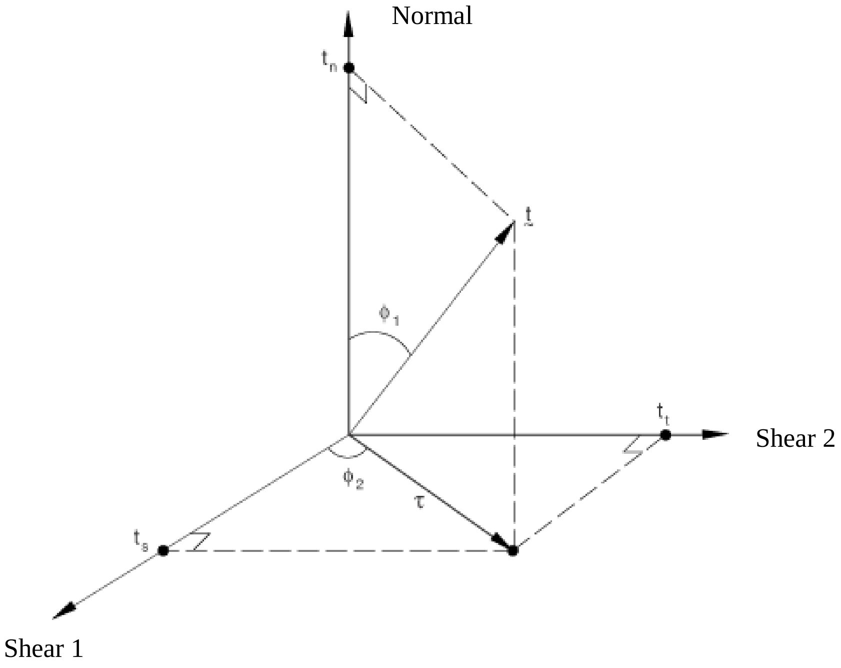

Figure 8.5 Mode-mix measurements based on tractions [47]

Since a direct tension single fiber pullout experiment gives the full behavior curve as shown in Figure 8.4, the model parameters for bond stiffness, *K*, are easily determined. The pre-failure behavior must be linear elastic, so these terms are determined based on the peak values. Due to the geometry of the fibers, only the local shear in the 1- direction (along the fiber length) will allow any substantial transfer of force. However, it should be noted that because there is no agreement in the literature on how to experimentally determine the local shear 2- or normal bond parameters of reinforcing fibers, it is assumed in this research that it is equivalent to the local shear 1- parameters. Realistically this is unlikely to be true, but for this particular experiment, which is direct tension and thus mobilizes almost entirely shear forces only, this assumption is considered to be adequate.

To achieve the desired bond behavior as seen in Figure 8.1, there are four bond behavior components that must be implemented in the model: (1) tangential behavior, (2) normal behavior, (3) surface-based cohesive interaction, and (4) damage evolution. The tangential behavior defines the friction coefficient which would only become useful after a bond has failed but the contacting surfaces may still transfer shear stresses. The normal behavior uses a "hard" contact relationship that minimizes the penetration of the slave surface into the master surface at the constraint locations and does not allow for the transfer of tensile stresses across the interface. The cohesive interaction coupled with the damage evolution law is what defines the relationship seen in Figure 8.1. A summary of all the constants used to achieve the results shown in Figure 8.6 is given in Table 8.1.

Table 8.1 Parameters for surface-based cohesive bond

Bond Component	Description	Constant	Value
Tangential Behavior	Coefficient of Friction	μ	0.45
Normal Behavior	"Hard" Contact		
Cohesive Behavior	Stiffness in Shear 1	K_{ss}	8990 lb/in
	Stiffness in Shear 2	K_{tt}	8990 lb/in
	Stiffness in Normal	K_{nn}	8990 lb/in
Damage Behavior	Max Separation for Damage Initiation	δ_o	0.137 in
	Max Separation for Failure of Bond	δ_f	0.630 in
	Damage Parameter	D	1.4
	Mode Mix 1	ϕ_1	0.6
	Mode Mix 2	ϕ_2	0.5

The final, calibrated model results for the fiber pullout experiment of a fiber at 20 mm embedment is shown in Figure 8.6, plotted along with the experimental results for comparison. Although minimal discrepancy is noted in the plots, the critical element of comparison is the energy dissipated due to failure, G^C. This value is equivalent to the area under the traction-separation curve. With respect to G^C, the model given in Figure 8.6 is within 2% of the experimental results.

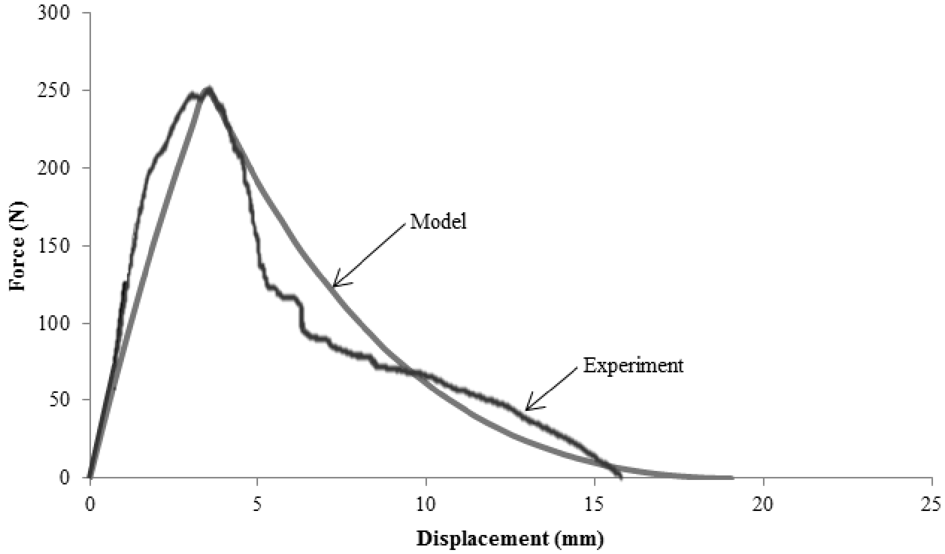

Figure 8.6 Single fiber pullout experiment and calibrated model results

For the sake of simplicity, a concrete material model available in Abaqus was used to simulate the behavior of the cementitious matrix. The concrete damaged plasticity (CDP) model uses concepts of isotropic damaged elasticity along with isotropic tensile and compressive plasticity to represent the inelastic behavior of the matrix. Since it has the capability of smearing the effect of reinforcement, it is an ideal candidate for the homogenized macro model as well. It is generally accepted that Hillerborg's (1976) fracture energy proposal is adequate to allay any concerns of mesh sensitivities in models of concrete where there is no reinforcement in large regions of the model [47]. Hillerborg defined the energy required to open a unit area of crack, G_f, as a material parameter, using brittle fracture concepts. Since the primary principles of blast center on energy absorption, this fracture energy, G_f, is directly related to the composite's eventual blast resistance. By performing a direct uniaxial tension test of unreinforced Ashcrete, the necessary material parameters to calibrate a CDP material model were found. The relationship between fracture energy, G_f, failure stress, σ_{t0}, and cracking displacement, u_{t0}, is shown in Eq. (8.5) and Figure 8.7.

$$u_{t0} = 2G_f / \sigma_{t0} \tag{8.5}$$

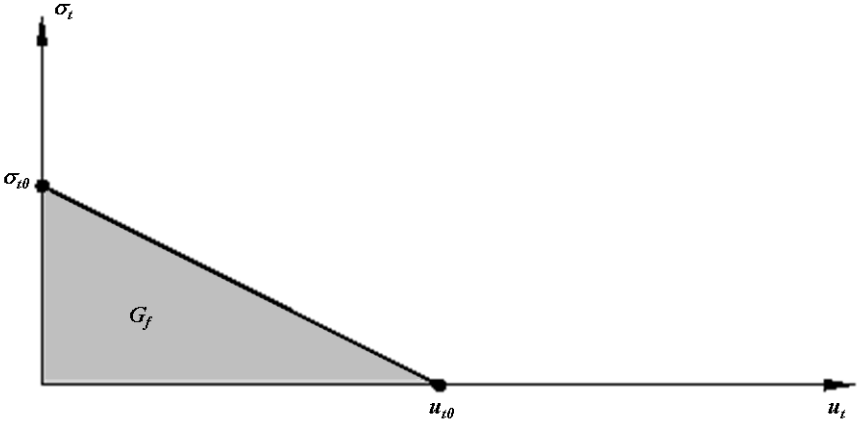

Figure 8.7 Post-failure stress-fracture energy curve

It should be noted that the implementation of this stress-displacement concept in a FE model requires the definition of a characteristic crack length associated with an integration point and is based on the element geometry. This definition of characteristic crack length is used and necessary because the direction in which cracking occurs is not known prior to the analysis. This means that elements with large aspect ratios will have a different behavior depending in which direction the cracking occurs. Therefore, some mesh sensitivities remain because of this bias to aspect ratio. To avoid these issues, meshes were created with as many elements as possible having aspect ratios close to one.

To characterize the tensile response of the unreinforced Ashcrete matrix material, direct tension (DT) experiments were undertaken at ERDC. The sample geometry used in this study is shown in Figure 8.8 and the corresponding test setup is shown in Figure 8.9. Due to the shape of the specimen, this particular geometry is referred to as a dog-bone (DB) specimen. In the literature, there appears to be little consensus on the recommended procedure for testing concrete in direct uniaxial tension [16], [54]. Some researchers have attempted creating a uniform sample geometry with various epoxy bonded end designs to transfer the load from the grips of the universal testing machine (UTM) to the sample. However this approach requires tedious sample preparation and allows the potential for slippage due to insufficient epoxy strength. Moreover, this method has a tendency to induce significant clamping forces on the sample area held within the grips of the testing equipment.

The alternative approach used in this study was to use a variation in sample geometry near the ends to enable load transfer through friction grips. With this approach, stress concentrations are unavoidable at the change in sample geometry, but a low angle of change can minimize this local effect [16]. The experimental setup also included the proper rotational degrees of freedom, so nearly identical boundary conditions could be applied in the model. As this specimen was created in a lab by use of molds, the randomly oriented fibers contained within the matrix material are confined within the boundaries of the mold. All fibers are whole, and for simplification in the model, assumed to be straight. Computer tomography (CT) scans of actual specimens were undertaken to view the internal layout of all the fibers and the assumption that the fibers remain straight was found to be valid.

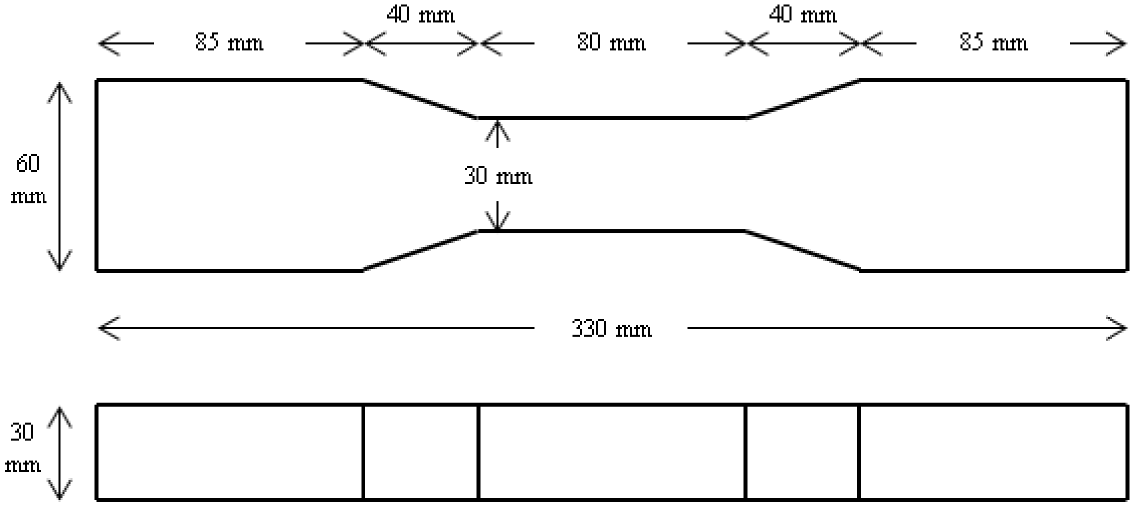

Figure 8.8 Dimensions for direct tension DB specimen

An example of the experimental results of direct uniaxial tension is shown in Figure 8.10. The CDP constants that give this response are shown below in Table 8.2. The widely dispersed data points are a result of high sensitivity of the displacement-controlled universal testing machine (UTM) as well as the magnification of the rather small magnitude of displacements being applied. A simple model of the dimensions in Figure 8.8 was built and analyzed iteratively to determine the appropriate G_f value for Ashcrete. The model results are also plotted on Figure 8.10.

Table 8.2 Material parameters for unreinforced Ashcrete

Material Model	Description	Value
Concrete Damaged Plasticity	Dilation Angle, ψ	31
	Eccentricity, ε	0.1
	σ_{b0}/σ_{c0}	1.16
	K	0.667
	Viscosity, μ	0
Compression	Yield Stress	21,000 psi
	Inelastic Strain	0.001
Tension	Yield Stress	600 psi
	Fracture Energy	0.3 lb/in
Elasticity	Young’s Modulus	5,500,000 psi
	Poisson’s Ratio	0.15

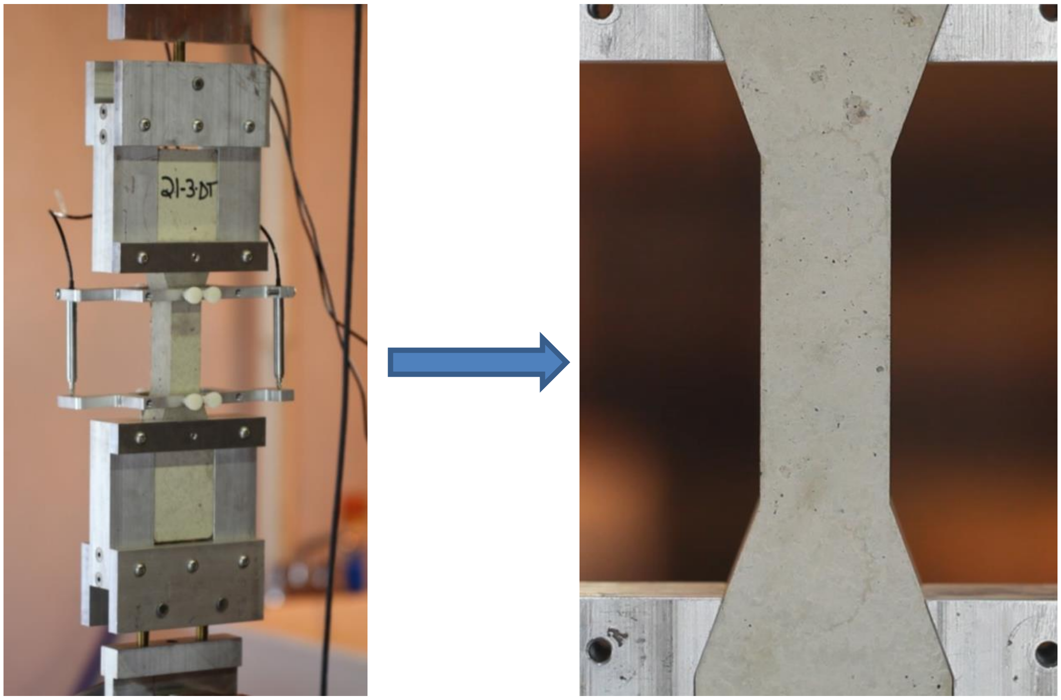

Figure 8.9 Experimental setup of direct tension test of Ashcrete DB specimen [16]

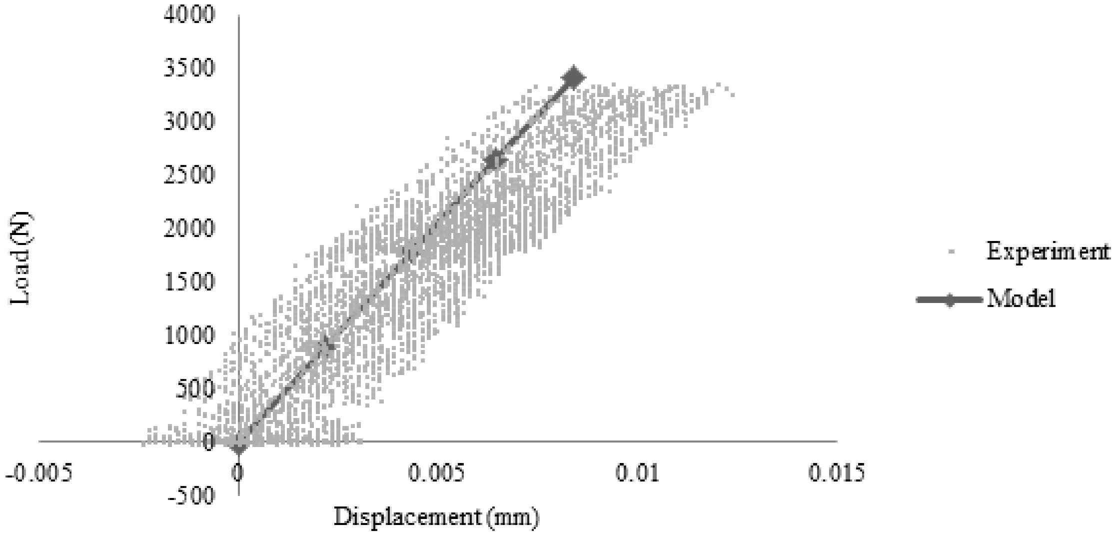

Figure 8.10 Direct uniaxial tension of unreinforced Ashcrete

The results in Figure 8.10 show good agreement between the model and the experiment used to calibrate it. The fracture energy, G_f, failure stress, σ_{t0}, and cracking displacement, u_{t0}, used in this calibration are used in all the subsequent simulations using this matrix material. Any further changes in the material of interest would require this particular test and calibration methodology for the model to be applied appropriately.

The calibration for the material model used for the polypropylene fibers also involved a direct uniaxial tension experiment (Figure 8.4). A simple elastic-plastic material model was used to define the behavior. The helical twisting of the bundled fibers created a modeling challenge. As the exact number of monofilaments varies from fiber to fiber, ideal rectangular-cubic geometry was assumed in order to reduce computation time and simplify the meshing algorithms. As long as the approximate cross section and surface area remained more or less equivalent, no large scale discrepancies were noticed.

8.3 Random Dispersion and Orientation of Short Fibers

The random distribution and orientation of fibers in the present composite allows for ease of manufacture in the field, but presents new challenges in modeling. Preliminary modeling studies showed that while slight variations in fiber orientations do not largely affect the composite's ductility, the fiber locations have a major influence in energy absorption. Although majority of the fiber dispersions and orientations are random, certain outside influences can affect these parameters. For example, in casting the direct tension DB specimens, the molds used have a minimum web width that is smaller than the fiber length. A similar behavior would be observed in casting reinforced panels where the thickness of the panels is less than the fiber length. This causes the orientations in the web to be less random. Orientations near any mold barrier are likewise affected. To handle this phenomenon, a MATLAB script was written to encompass the semi-random dispersion and orientations of fibers in a short-fiber reinforced composite structure. Given the length and number of fibers and rectangular mold geometry, the program randomly generates a number of fiber midpoint coordinates in three-dimensional space and two orientation angles (one angle in the local x-y plane, and a second angle into the z-dimension). Based on these parameters, the fiber endpoints are then computed. If any of these endpoints cross the boundary, they are deleted and new fibers are generated. Once the proper number of fibers is generated, a minimum distance check is performed. This is because the MATLAB script treats these fibers as lines with no finite thickness orthogonal to the axis. In order to avoid fibers overlapping each other, a minimum distance is assigned (typically the diameter of a fiber) and each fiber is checked against all others to ensure that none overlap. Figure 8.11 gives the flow diagram of the algorithm developed for the purpose.

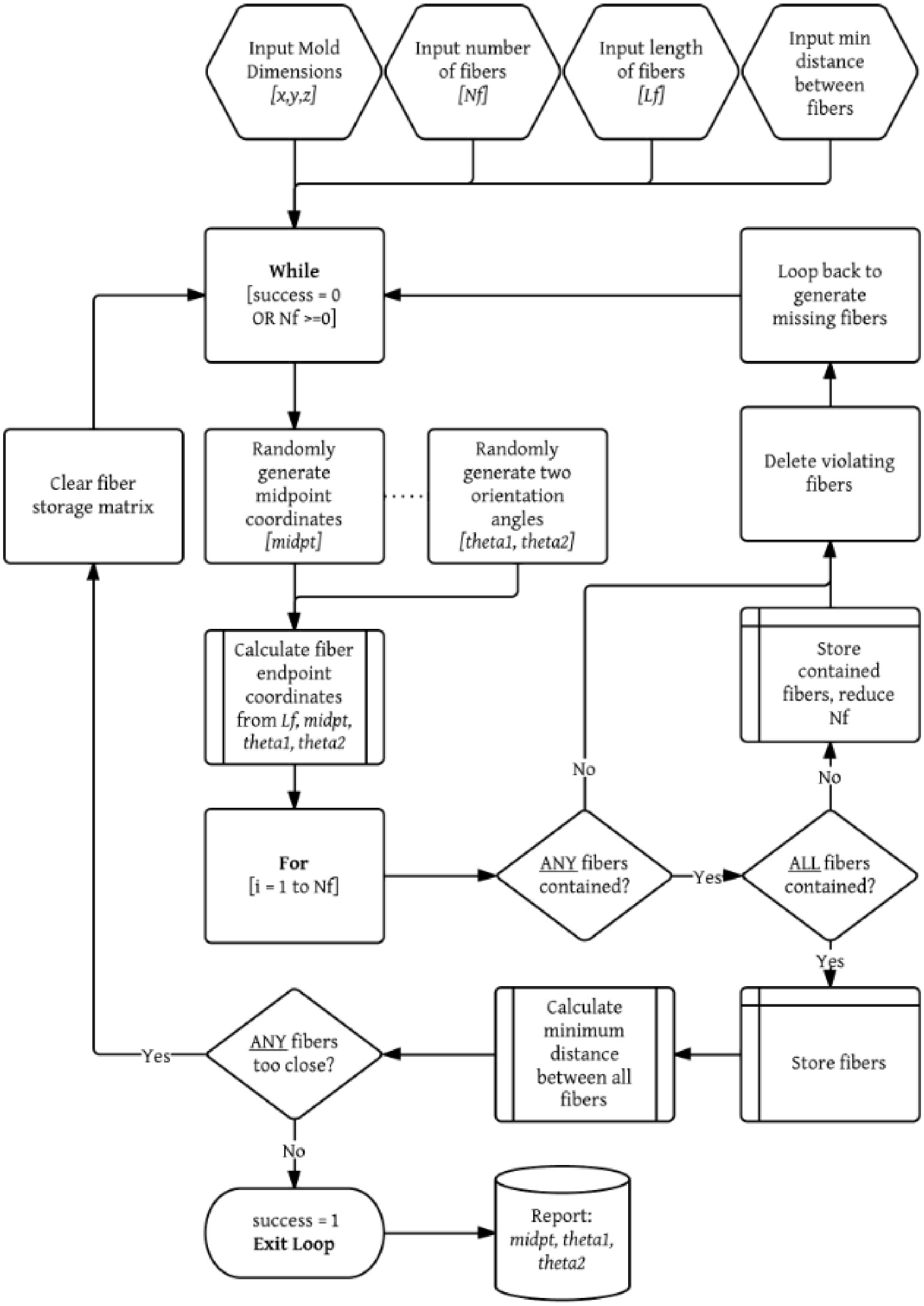

Figure 8.11 Flow chart of MATLAB program for random fiber generation

For the DB model, a 2% volume percentage of fibers gave 386 total fibers. Using the program above, the entire DB model was assembled. Figure 8.12(a) and (b) below shows the final assembly in plan view and side view, respectively.

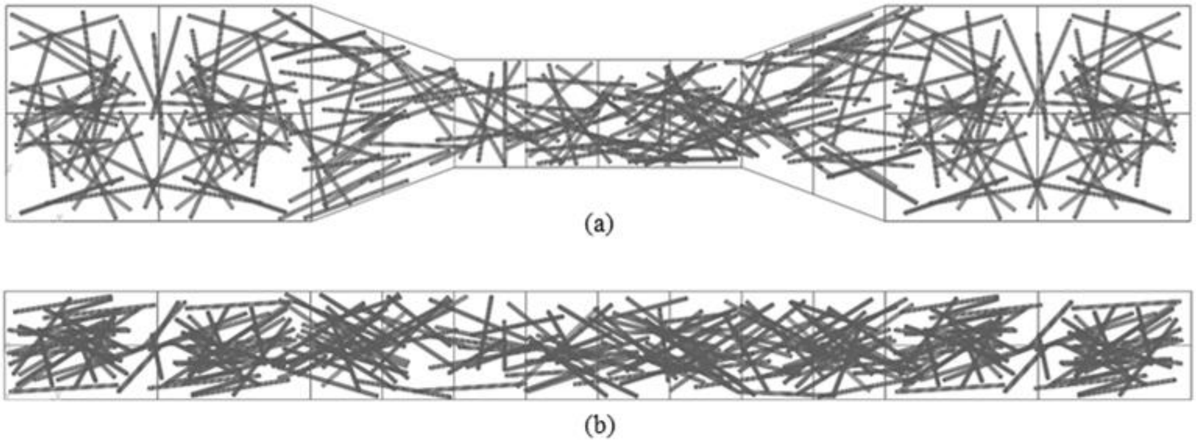

Figure 8.12 (a) Plan view of DB assembly (b) side view of DB assembly

8.4 Multi-Scale Approach

The short-fiber reinforced cementitious material used in this study is essentially heterogeneous and for computational efficiency requires multiscale treatment. Here two scales are being considered: (a) mesoscale, to characterize the interaction between the randomly distributed short fibers and the matrix material, and (b) macroscale, based on homogenized physical properties disclosed by the local analysis. The concept of numerical multiscale modeling to represent the effect of microscopic structure of a material at the macroscopic level originated from the pioneering efforts of Babuska [4], Aboudi [1], and others. This concept is in a state of flux and a number of basic schemes with multitudes of variations have been put forward [1]. It is now well recognized that in characterizing these materials, some kind of asymptotic or volume averaging technique is necessary. The more popular homogenized macroscale model essentially works with smeared local variations in the physical parameters arrived at by undertaking localized analysis at sub-macro levels [4]. On the other hand, the asymptotic expansion of $u(x,y,z,t)$ can be treated as macro-level response appended by first, second, and higher order terms of the scale factor, ε, as

$$u(x,y,z,t) = u_0(x,y,z,t) + \varepsilon u_1\left(x,y,z,\tfrac{x}{\varepsilon},\tfrac{y}{\varepsilon},\tfrac{z}{\varepsilon},t\right) + \varepsilon^2 u_2\left(x,y,z,\tfrac{x}{\varepsilon},\tfrac{y}{\varepsilon},\tfrac{z}{\varepsilon},\tfrac{x}{\varepsilon^2},\tfrac{y}{\varepsilon^2},\tfrac{z}{\varepsilon^2},t\right) + O\left(\varepsilon^3\right). \quad (8.6)$$

Here, the scale factor applied to physical coordinates, ε, is a small parameter representing the wave length of a periodic function. In the homogenization scheme, the macroscale properties are linked to the mesoscale response based on analysis performed on representative sample(s) of the material through Hill-Mandel type relationships applied through Cauchy stress and deformation gradients at the mesoscale to the Piola-Kirchoff stress and deformation gradients at the macroscale [26].

In the material of current study, heterogeneity is caused by the cementitious matrix material as well as short-fiber reinforcement. It is necessary to account for these in arriving at the constitutive properties to be used at the macroscale. The random distribution of fibers in terms of minimum distance between fibers, spatial orientations, as well as the total number of fibers present in a given volume makes this problem very complex. Due to the lack of any identifiable global periodicity, the traditional approach based on the identification of a Representative Volume Element (RVE) cannot be justified here and a different strategy needs to be formulated. The random distribution and orientation of fibers is determined from probabilistic considerations programmed in the MATLAB script developed for the purpose and the number of fibers determined from the volumetric ratio of interest. The first step was to establish the random fiber configuration for the problem domain under consideration (as in Figure 8.12). The problem domain is then partitioned into subdomains of suitable size(s). Each such subdomain is being termed as a Characteristic Volume Element (CVE). Due to the random nature of fiber distribution, a number of such CVEs are required to be considered in the investigative stage of the study. The selection of CVE is based on considerations like statistical representation of homogenized behavior, characteristic dimensions of the structural components, size of the fibers, and the ability to accurately detect the effects of localized damage characteristics. In order to economize computational effort without undue sacrifice of accuracy, smaller CVEs can be used in areas around the expected position of local damage with high stress gradients and larger ones in non-critical regions away from it. Moreover, in areas away from the region of particular interest, the minimal number of typical CVEs (say, one) can be considered. In some situations, a more efficient approach will be to stick with initial homogenized representation in non-critical regions; whereas the critical region is subjected to multi-scale treatment.

In the present study, homogenization has been based on CVE properties determined at the mesoscopic level, primarily to account for the two material phases: the matrix material and the fibers (including bond behavior between the two) as well as any accumulated damage caused by the loading process. The proposed scheme does allow inclusion of damage behavior of the matrix material at the mesoscale, because from a series of laboratory tests, it was found that for the domain dimensions considered, as long as the maximum aggregate size is less than 10 mm, the microstructure has little bearing on the response. The CVEs are identified and the constitutive relationships are obtained at the macroscale by the Hill-Mandel macrohomogeneity criterion. The influence of all the CVEs at a point of interest in the domain can be accounted for by probabilistic data fitting based on Ordinary Kriging [37].

A two-scale analysis scheme based on these considerations is shown in Figure 8.13. The scheme is essentially based on the solution of two nested boundary value problems, one at the mesoscale and the other at the macroscale. The scheme can be modified to include second-order behaviors like material and geometric nonlinearities. In order to develop a clear understanding of the homogenization scheme, a few example problems in the one-dimensional space were defined and the stated homogenization process was applied using finite element software. These examples included (1) an elastic bar with periodic material properties, (2) an elastic bar with non-periodic material properties, (3) an elastic-plastic bar with periodic material properties, and (4) an elastic-plastic bar with non-periodic material properties. The first three examples were completed to validate the approach. Only the fourth example will be presented here. Once the methodology is validated, it gives a clear path for applying this scheme to the three-dimensional problem of multi-scale CVE treatment of the reinforced Ashcrete DB specimen.

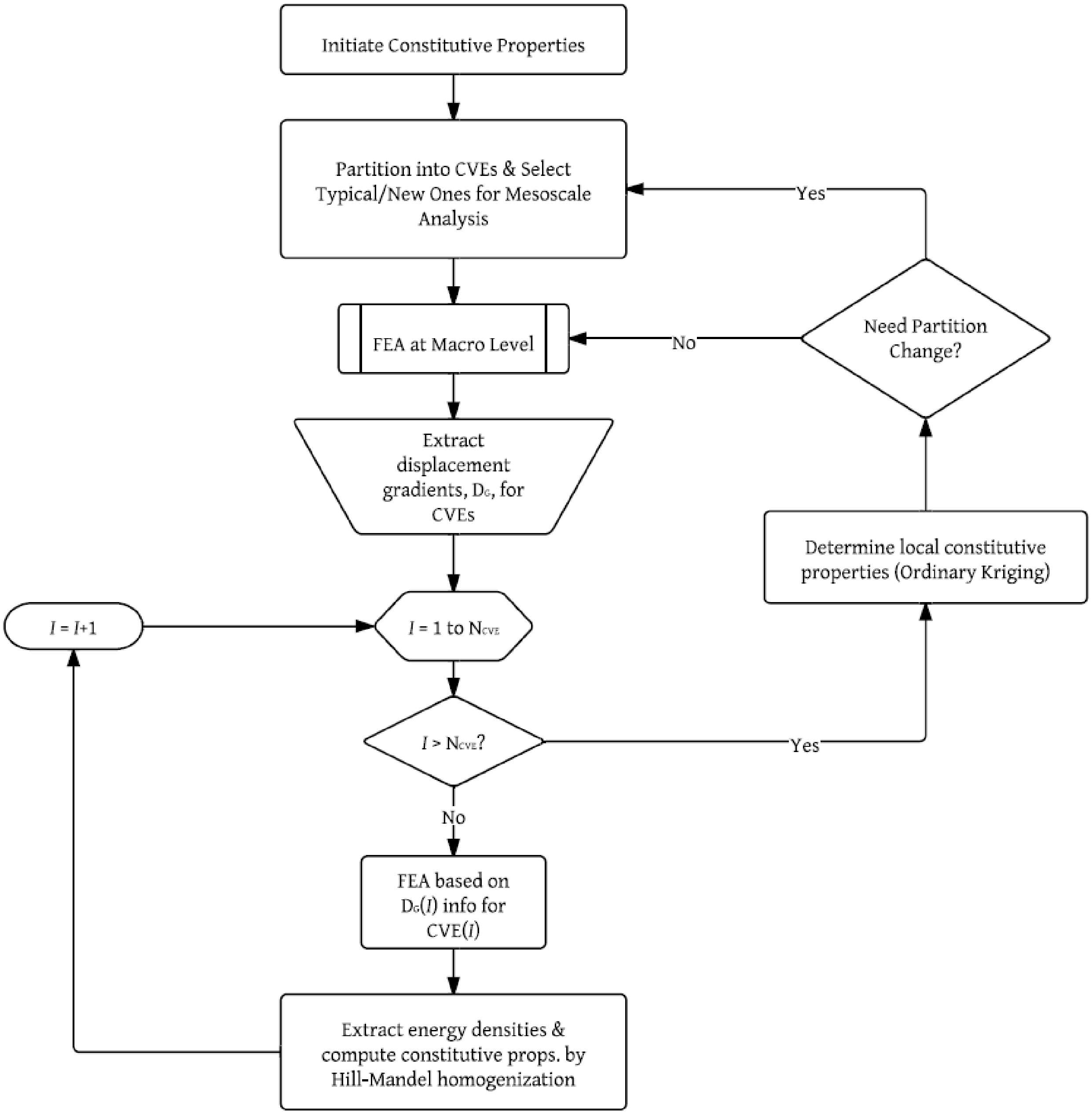

Figure 8.13 Multi-scale homogenization scheme for two-scale analysis

The one-dimensional example presented here considers an axial bar as shown in Figure 8.14. The support conditions are $u(0) = u(L) = 0$. The cross sectional area, A, is kept at a constant value of 0.1 throughout the length, $L = 10$ and $u_1 = u_2 = 0.05$ (in directions shown in Figure 8.14). Identical displacement boundary conditions (in opposite directions) are applied at $3L/8$ from each end. The elastic material properties for the entire bar have a constant value of $E = 10{,}000$ and $\nu = 0.3$. However, the plastic material properties vary for the tensile region of the bar, allowing for multi-scale treatment. Table 8.3 summarizes the elastic-plastic material properties of the CVEs. The material properties given are yield stress, σ_y, ultimate stress, σ_u, modulus of elasticity, *E*, yield strain, ε_y, ultimate strain, ε_u, and plastic strain, ε^{pl}. As shown, each CVE is comprised of four different materials. The variation in the stress vs. strain curves of the four different materials in CVE 1 take the form as shown in Figure 8.15. The materials in CVE 2 and 3 would have a similar behavior. The variation of yield stress over the length of the bar is shown in Figure 8.16.

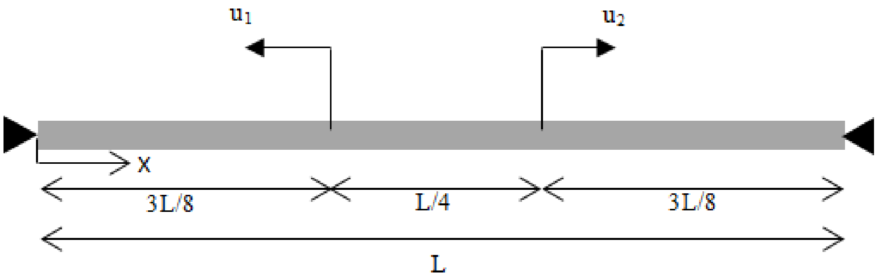

Figure 8.14 Schematic of one-dimensional validation example

Table 8.3 Elastic-plastic material properties for CVE parts

Material	σ_y	σ_u	*E*	ε_y	ε_u	ε^{pl}
CVE 1						
1	70	100	10,000	0.007	0.011286	0.0012857
2	60	100	10,000	0.006	0.012667	0.0026667
3	50	100	10,000	0.005	0.015000	0.0050000
4	40	100	10,000	0.004	0.019000	0.0090000
CVE 2						
5	90	100	10,000	0.009	0.010111	0.0001111
6	70	100	10,000	0.007	0.011286	0.0012857
7	50	100	10,000	0.005	0.015000	0.0050000
8	30	100	10,000	0.003	0.026333	0.0163333
CVE 3						
9	60	100	10,000	0.0060	0.012667	0.0026667
10	57	100	10,000	0.0057	0.013244	0.0032439
11	53	100	10,000	0.0053	0.014168	0.0041679
12	50	100	10,000	0.0050	0.015000	0.0050000

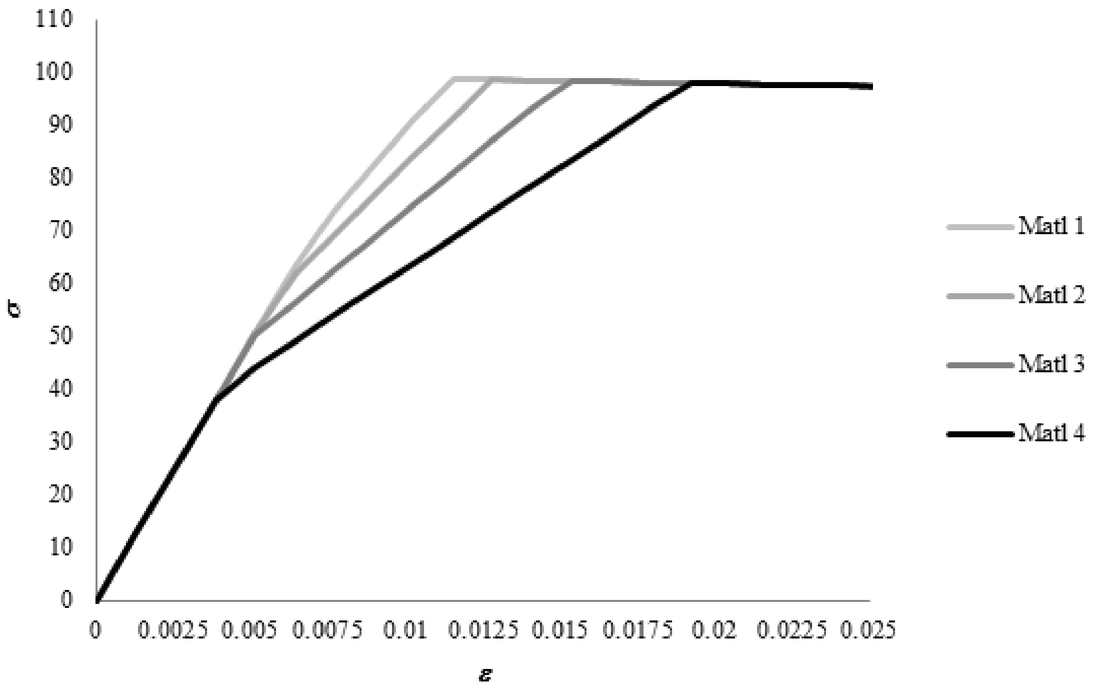

Figure 8.15 Stress vs. strain curves for materials 1-4

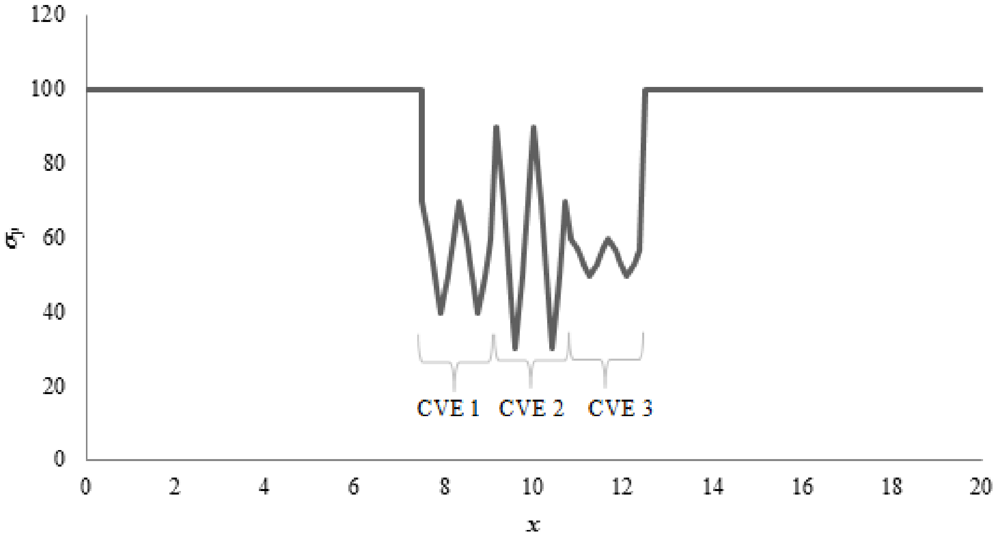

Figure 8.16 Variation of plastic material properties along bar length, *L*

Each CVE consists of 12 parts (therefore 12 linear elements), so the material sequence for CVE 1 would follow: 1, 2, 3, 4, 4, 3, 2, 1, 1, 2, 3, 4 (and similarly for CVE 2 and 3). Using the elastic-plastic material data from Table 8.3, stress-strain curves can be generated for each material similar to that of Figure 8.15. Following the scheme outlined in Figure 8.13, the first step was to determine the initial constitutive properties of the bar at the macroscale. In arriving at the initial homogenized constitutive properties shown in Figure 8.16, the finite element analysis was first based on averaged plasticity values for each CVE. The mesoscale model for each CVE was analyzed thereafter using a 12 element model and applying the deformations disclosed by the first analysis as boundary conditions. The Hill-Mandel macro homogeneity criterion was invoked thereafter to arrive at the improved plasticity values for the CVEs. These improved values were used in the first iterative cycle, a 5 element model (one element for the two elastic ends and one homogenized element for each CVE) and compared to a full meso-scale model (the "actual" solution), also a 38 element model. The full iterative homogenization process results as well as the full meso-scale solution are summarized in Figure 8.17 as the stress vs. strain response. As is shown by the results in Figure 8.17, after one iteration of the homogenization scheme, the improved homogenized constitutive properties give a response that is within 1.0% of the full meso-scale model.

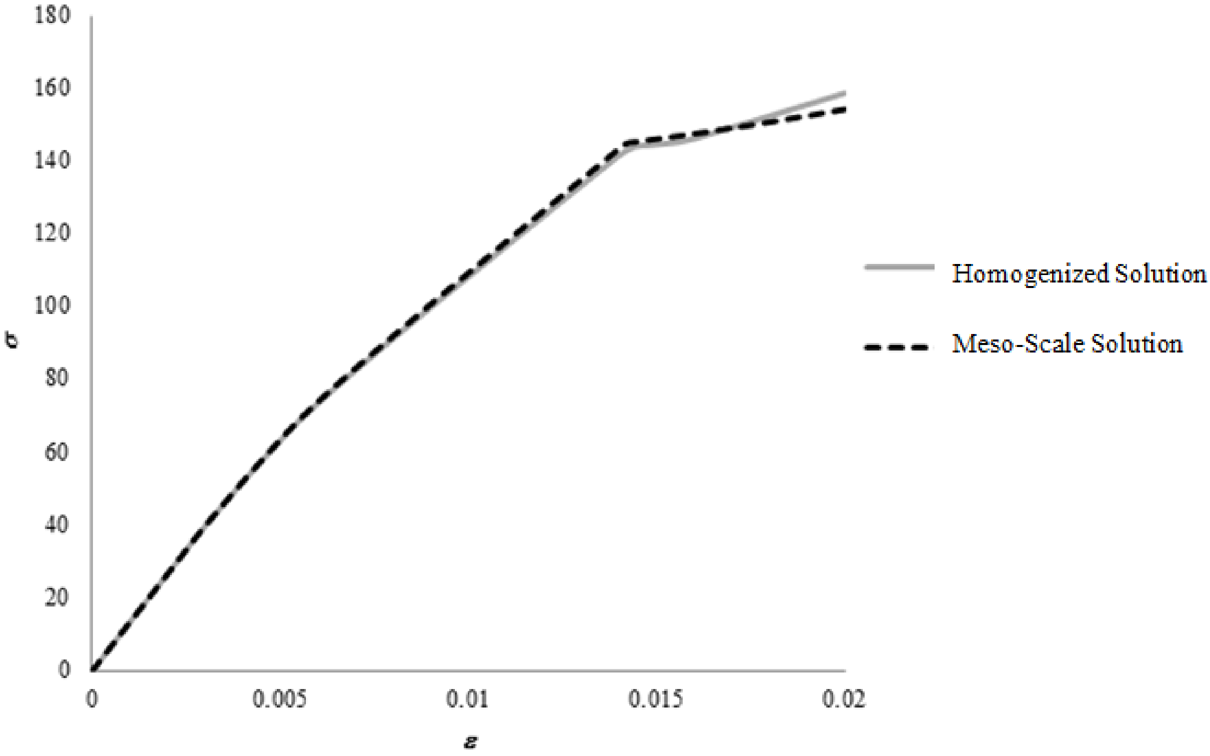

Figure 8.17 Stress vs. strain curves for CVE-homogenized axial bar compared to full meso-scale model

The previous example problem validates the multi-scale scheme proposed analytically to the extent of one-dimensional problems accounting for elasticity, plasticity, and local variations of material properties and geometry. Using the same scheme as outlined in Figure 8.13, this scheme can now be extended to a three-dimensional case.

Before a model can be validated experimentally, the issue of CVE size must be addressed. Since the reinforcing fibers are random in their dispersions and orientation, no periodic boundaries can be used. The hypothesis put forward is that the appropriate size of a CVE should be loosely based upon the length of a reinforcing fiber. The major contributory factor of reinforcement is through the transfer of stresses by means of the cohesive bond between matrix and fiber. This stress transfer is maximized when the entire fiber length is utilized. To test this theory, a large CVE of short-fiber reinforced Ashcrete was built in 3D and subjected to uniaxial tension. This CVE has two constant dimensions (say, depth and height) and one variable dimension (say, length). The purpose of varying length is to determine if the constitutive relations of each CVE of differing length are likewise different, thereby suggesting that there is an ideal CVE size, or if the CVE size is independent of constitutive properties. This strategy will become more apparent later.

First, a rectangular, prismatic CVE was created that was 1 in x 1 in x 2 in. The fibers were also rectangular prisms of dimensions 0.04 in x 0.04 in x 1.6 in. To assign 2% fibers by volume, 13 fibers were needed. Using the MATLAB program described in Figure 8.11, random disposition of the fibers inside the CVE were assigned. Then the CVE was partitioned into eight equal segments, each 0.25” in length. The assembly of the CVE, fibers, and partitions are shown below in Figure 8.18. To create each smaller CVE (of variable length), the remaining fibers and matrix on the opposite side of the partition were removed. Figure 8.19 shows the fiber configurations for 0.5 in, 0.75 in, and 1 in CVEs. The boundary conditions in this model were applied to the left and right faces of each subsequent CVE as oriented in Figure 8.19. The boundary conditions were displacement gradients extracted from an initial homogenous elastic model of just the matrix material as shown in Figure 8.18, and therefore each CVE had a slightly different boundary condition. The mesh consisted of a global seed size of 0.08 in with an internal edge seed of 0.02 around the fiber-matrix interfaces. Linear, tetrahedral elements were used for the matrix while linear, hexahedral elements were used for the fibers.

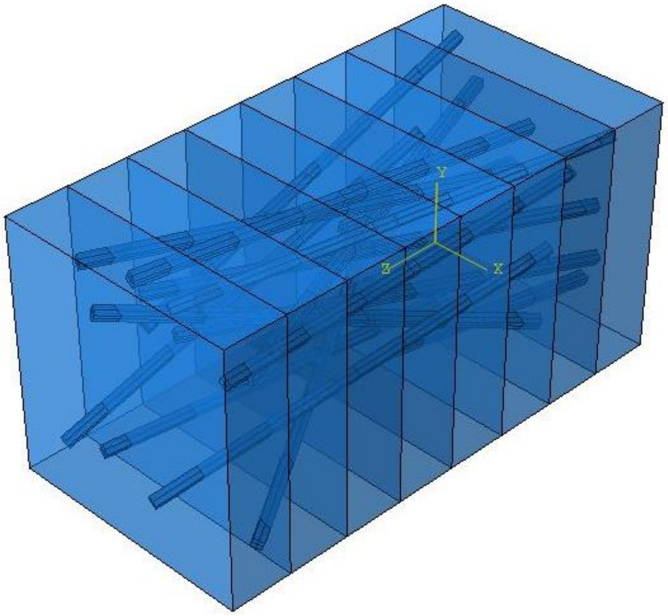

Figure 8.18 Assembly of CVE, fibers, and partitions

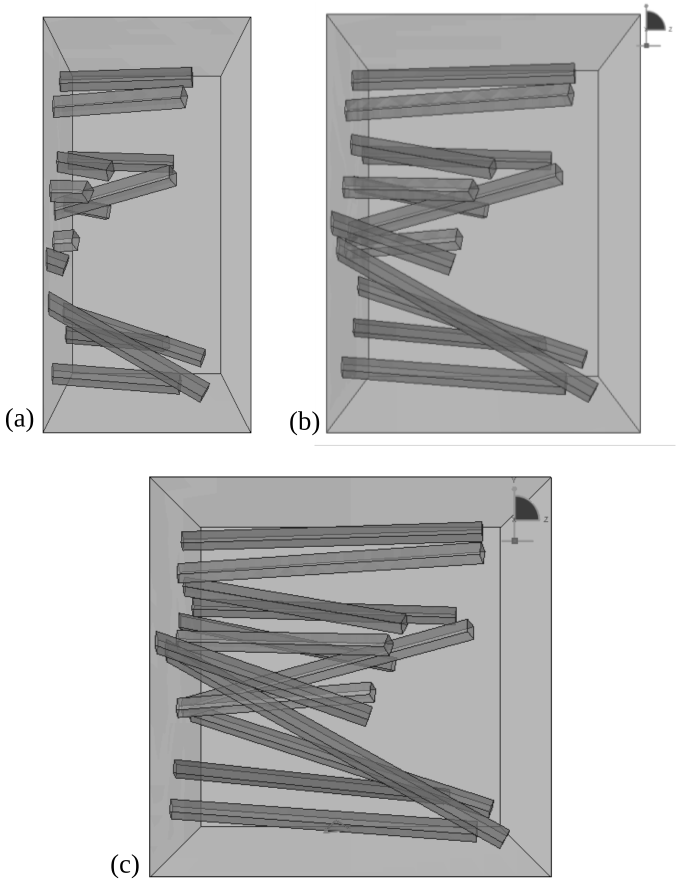

Figure 8.19 Assembly of CVEs of length (a) 0.5 in, (b) 0.75 in, and (c) 1.0 in

Next CVEs are subjected to mesoscale analysis to determine homogenized material properties for a macroscale model. The methods used in the literature for bridging the scales in this branch of multiscale modeling vary greatly. A commonly used method for bridging the scales is the Hill-Mandel principle of macrohomogeneity, which establishes the energy consistency between the macro and mesoscale. The general statement of this principle is that the macroscopic stress power equals the volume average of the microscopic stress power over the CVE [26]. To achieve this, the general procedure involves equating the strain energy densities between the scales. In doing so, a post-failure criterion from the mesoscale was able to define the homogeneous macroscale material behavior. First, the mesoscale analysis was decomposed into the elastic and plastic strain components, in the form

$$d\varepsilon_{ij} = d\varepsilon_{ij}^{e} + d\varepsilon_{ij}^{p}\,, \tag{8.7}$$

where ε_{ij} is the total strain, ε_{ij}^{e} is the elastic strain component, and ε_{ij}^{p} is the plastic strain component. By Hooke's Law,

$$d\varepsilon_{ij}^{e} = \frac{1}{2G}\left(d\sigma_{ij} - \frac{3\nu}{1+\nu}\delta_{ij}dp\right), \tag{8.8}$$

where G is the shear modulus, σ_{ij} is the stress, ν is Poisson's ratio, and p is the mean stress, and in terms of deviatoric stress, $s_{ij} = \sigma_{ij} - \delta_{ij}p$,

$$d\varepsilon_{ij}^{p} = s_{ij}d\lambda\,. \tag{8.9}$$

Once the incremental strain components are computed, the increment in plastic work per unit volume is arrived at by using

$$dW_p = \sigma_{ij} d\varepsilon_{ij}^p + \sigma_{ij} s_{ij} d\lambda , \tag{8.10}$$

and the increment in strain energy per unit volume is

$$dU = d\Pi = dU_V + dU_D = pd\Theta + \sigma d\varepsilon , \tag{8.11}$$

where U_V and U_D are the dilatational and distortional strain energies, respectively, and Θ ($= \varepsilon_{ij}$) is the volumetric strain. So from the mesoscale output, two output variables are tracked at predetermined seed points around the CVE: (1) elastic strain energy density, W^{el}, and (2) plastic dissipation energy density, W^{pl}. Eqs. (8.12) and (8.13) give the relationships between energy density, stress, and strain.

$$W^{el} = \int_0^t \sigma : \dot{\varepsilon}^{el} dt , \tag{8.12}$$

$$W^{pl} = \int_0^t \sigma : \dot{\varepsilon}^{pl} dt . \tag{8.13}$$

These variables were then plotted against the local principle strain values $(\varepsilon_{11}, \varepsilon_{22}, \varepsilon_{33})$ at each grid point. Figure 8.20 shows one such set of plots at one particular grid point for one particular strain component.

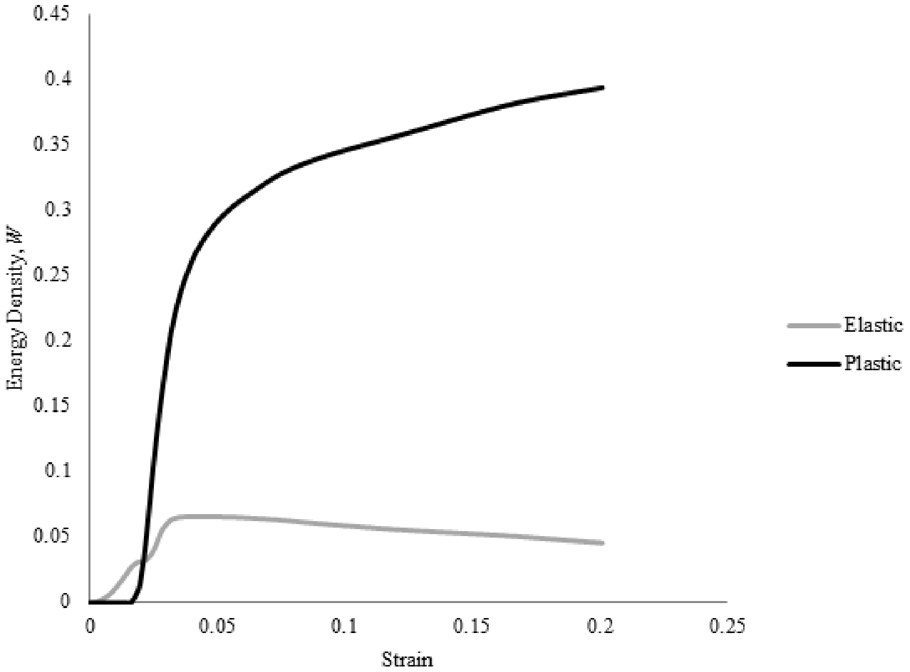

Figure 8.20 Elastic and plastic strain energy densities at grid point as a function of principal strain

The stress vs. strain constitutive relationships were determined by using the relationships in Eqs. (8.12) and (8.13). Since each seed point gives a different constitutive response with certain oscillatory behavior (from small developments of plastic strain, simulating cracking behavior), it is prudent to idealize the response to take the form

$$\sigma = \sigma_{\max} e^{-\alpha(\varepsilon-\varepsilon_i)}, \tag{8.14}$$

where $\sigma_{\max}$ is the peak tensile stress, ε_i is the strain at initial fracture, and α is an exponential parameter that describes how quickly the residual strength of the CVE degrades. Given this relationship, each seed point should yield a constitutive relationship that shows the general behavior shown in Figure 8.21. Using this generalized behavior, a simple comparison of these three constants $(\sigma_{\max}, \varepsilon_i, \alpha)$ allows for a broad statement regarding CVE size.

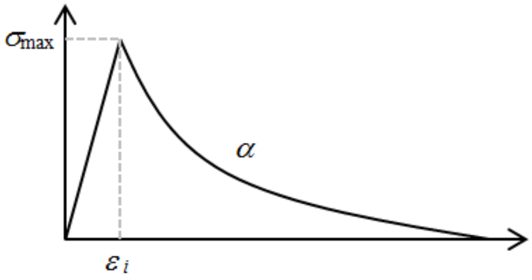

Figure 8.21 General form of constitutive relationship for CVEs in direct tension

To determine whether the length of a CVE was sufficient, the average values of $\sigma_{\max}, \varepsilon_i$ and α were evaluated over a CVE and compared to the CVEs of differing lengths. The average values are compared below in Table 8.4. As shown, the averages vary little when changing the total CVE length by as much as 12.5-25%. Shown next to the averages are the ranges of these values over the CVE. As expected, the seed points closest to fibers show the lowest α value, indicating a much lower degradation of material strength at that point. Since the α value controls the degradation of the strength of a material point, it can be concluded that the close proximity of the average α values over each individual CVE indicates a similar behavior. This is illustrated graphically in Figure 8.22.

Table 8.4 Generalized constitutive properties for CVEs of various lengths in direct tension

CVE Length	α (Range)	ε_i (Range)	σ_{max} (Range) (*psi*)
0.5 in	26.46 (10.31-45.83)	0.0019 (0.000203-0.01530)	746.18 (601.19-1128.48)
0.75 in	28.09 (8.74-47.09)	0.0025 (0.000195-0.000935)	723.79 (578.80-971.76)
1.0 in	22.78 (7.65-44.89)	0.0023 (0.000111-0.02581)	710.27 (544.18-922.63)

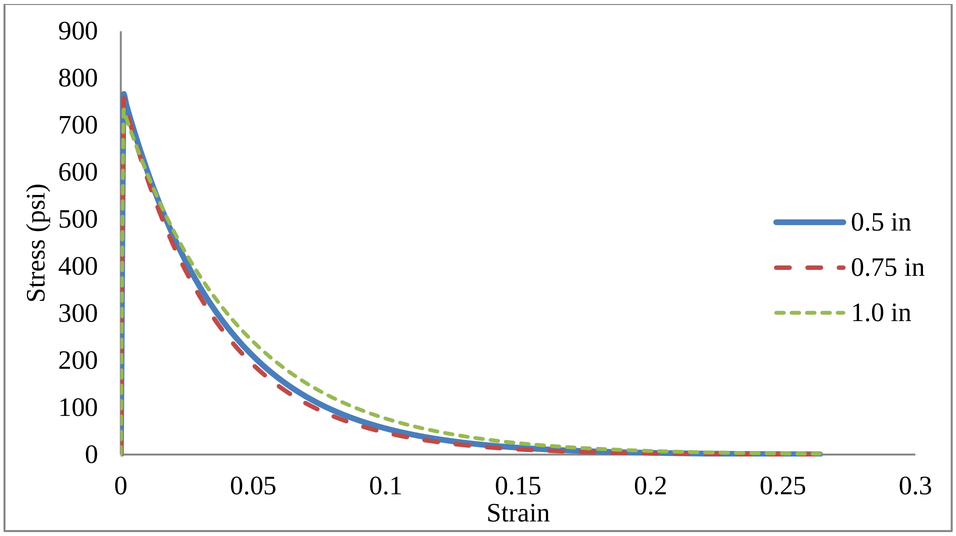

Figure 8.22 General constitutive behavior of CVEs of differing sizes

The final comparison is to determine if this model is representative of actual experimental behavior. To validate the multi-scale homogenization scheme proposed experimentally, it has been applied to the DT experiment conducted on a reinforced Ashcrete DB specimen at ERDC. The first step was to perform the simple analysis of a linear-elastic macroscale model, with 34,579 linear tetrahedral elements (hereafter referred to as the Macro 0 model), to determine the displacement values at the CVE boundaries. The Macro 0 model was partitioned into the CVEs with size considerations based on the consideration of statistically representative homogenized behavior, characteristic dimensions of the structural components, size of the fibers, and the ability to accurately detect the effects of localized damage characteristics. The Macro 0 model geometry is shown in Figure 8.23. Boundary conditions (BC) are located in the same location as in the experimental setup with proper rotational degrees of freedom to avoid introducing support moments. Since the experiment used a displacement-controlled UTM, the analysis is quasi-static with a displacement boundary condition (u_1) located at one end to mobilize the uniaxial tension in the specimen. To reiterate, the purpose of the Macro 0 model is to find appropriate displacement boundary conditions for CVE 1 (shown in Figure 8.23, with the analysis hereafter referred to as the Meso 1 model) that reflect the specimen geometry and its effect on the displacement fields throughout the analysis.

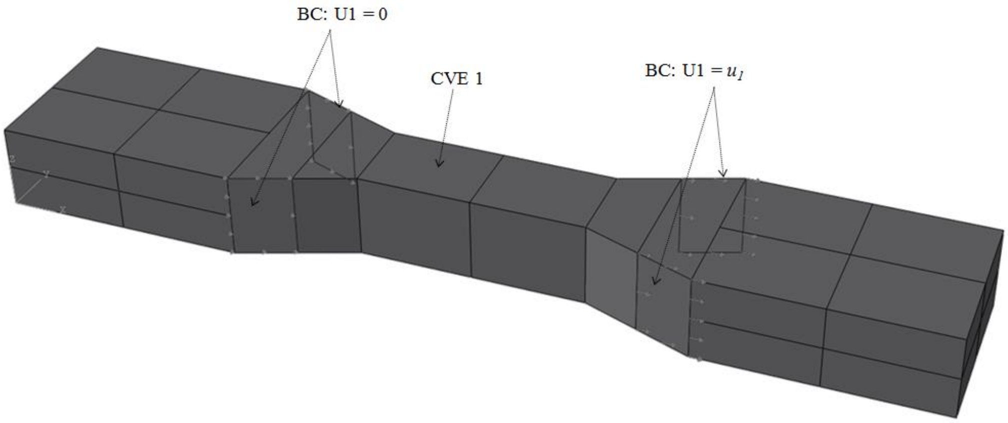

Figure 8.23 Macro 0 model assembly

Next, the principal components of the displacement vectors at the two boundary surfaces of CVE 1 were extracted from the Macro 0 model. This gave a total of six boundary conditions to apply to the Meso 1 model (two interior surfaces, three principal directions). To build the Meso 1 model, the assembly shown in Figure 8.12 was partitioned in the same locations as those shown in Figure 8.23. The final assembly of the Meso 1 model is shown in Figure 8.24(a)--(d). There were a total of 27 fibers in the CVE, nine of which were whole fibers completely enclosed within the CVE boundary, and 18 of which extended beyond the cut surfaces. These projecting fibers were trimmed off the cut boundary surfaces.

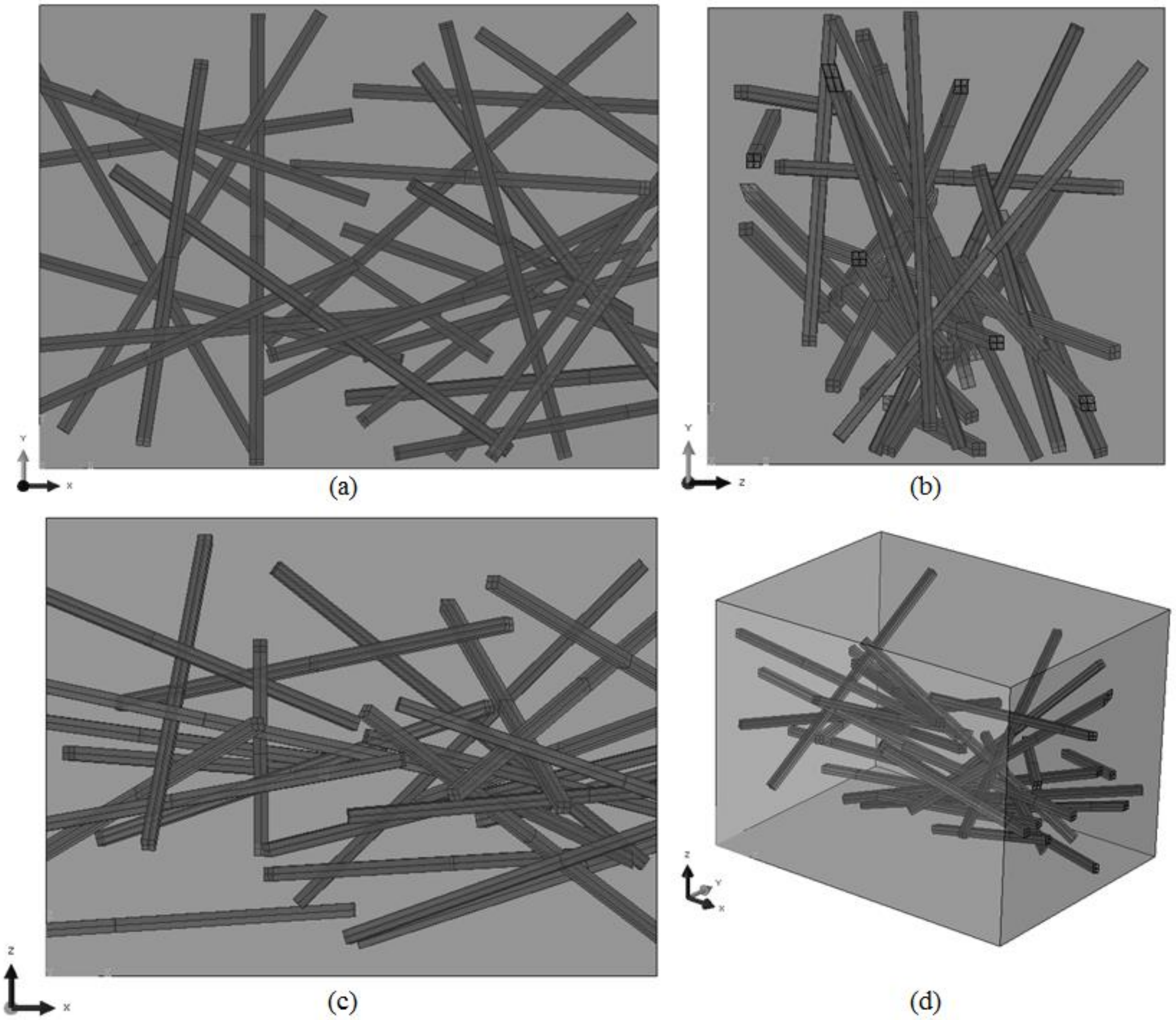

(a) (b) (c) (d)

Figure 8.24 Meso 1 assembly of CVE 1 in (a) x-y view, (b) z-y view, (c) x-z view, and (d) isometric view

As shown in Figure 8.13, the first step in the presented multi-scale scheme is to assume some linear elastic, homogeneous material property values for the macroscale, and analyze it. This allows for the determination of the displacement values at the shared CVE boundaries based on the macroscale geometrical configuration. However, since the meshes for macro CVE and meso CVE are of differing sizes, and unlike the one-dimensional examples, the displacements along the interfaces vary spatially, and some processing of the result is necessary. A simple nonlinear regression analysis was performed in order to model the spatial variation of displacement on any given boundary surface.

For the present purpose, a simple quadratic regression was considered to be adequate to approximate the spatial variation. Accordingly, the following quadratic polynomial is used to define the surface:

$$u(x,y) = C_1 + C_2x^2 + C_3y^2 + C_4xy + C_5x + C_6y\,, \tag{8.15}$$

where $u(x, y)$ is the displacement component as a function of the x-y position on the surface and C_i are the needed constants. In all the macroscale models, the boundary of each CVE is covered with a grid of evenly spaced points in a local x- and y-direction. At each of these, say, n grid points with coordinates (x_i, y_i) there is an observed displacement value, u_i .To solve for these constants, the following equation was used:

$$\begin{Bmatrix} C_1 \\ C_2 \\ C_3 \\ C_4 \\ C_5 \\ C_6 \end{Bmatrix} = \begin{bmatrix} 1 & x_1{}^2 & y_1{}^2 & x_1y_1 & x_1 & y_1 \\ 1 & x_2{}^2 & y_2{}^2 & x_2y_2 & x_2 & y_2 \\ \ldots\ldots & \ldots & \ldots & \ldots & \ldots & \ldots \\ 1 & x_n{}^2 & y_n{}^2 & x_ny_n & x_n & y_n \end{bmatrix}^{-1} \begin{Bmatrix} u_1 \\ u_2 \\ \ldots \\ u_{nn} \end{Bmatrix}, \tag{8.16}$$

where, with the form $\{C\} = [A]^{-1}\{u\}$, $[A]$ is an n by six matrix, and $\{u\}$ is a column matrix of dimension one by n. This set of equations is solved three times: once corresponding to each principal direction. This yields three boundary conditions for each CVE interior surface. Figure 8.25 shows the spatial variation of u_1 for the CVE located in the web of the DB specimen, on the interior surface.

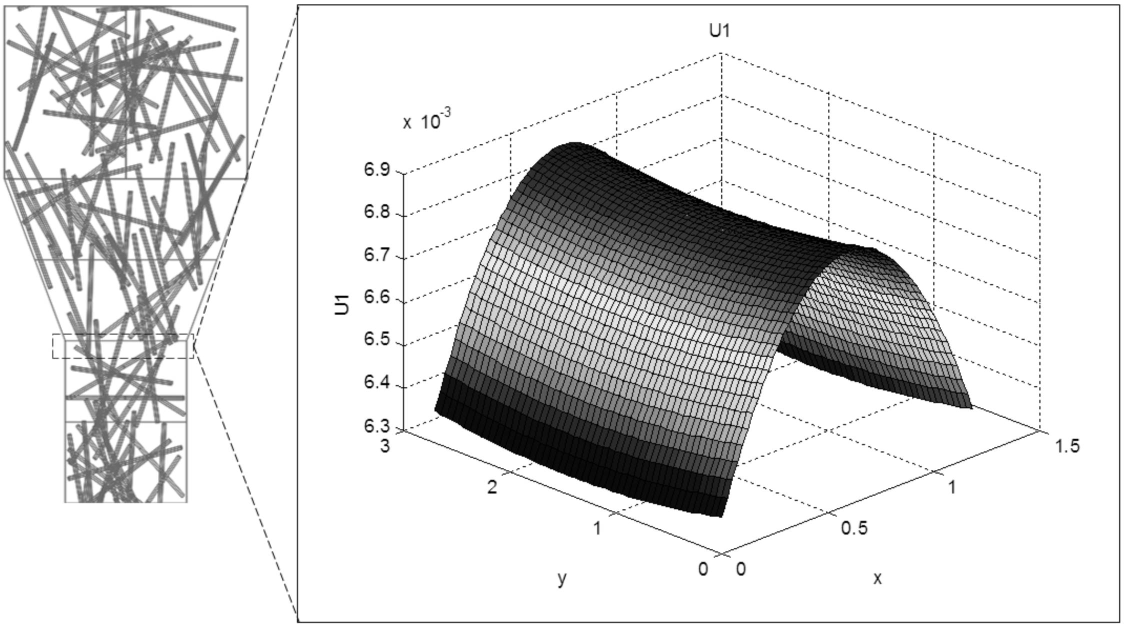

Figure 8.25 Quadratic regression of spatially varying displacement (u_1) on CVE boundary

The boundary conditions taken from the Macro 0 model and applied to the two end surfaces of the Meso 1 model all take the functional form of Eq. (8.7). Table 8.5 shows the constants, C_i, for these boundary conditions, given the interior CVE surface, and the principal displacement direction, *U*.

Table 8.5 Constants for surface-function regression for Meso 1 boundary conditions

	Boundary Condition					
	(Surface 1)			*(Surface 2)*		
Constant	U_1	U_2	U_3	U_1	U_2	U_3
C_1	6.383E-03	-1.061E-04	5.448E-04	1.500E-02	4.370E-04	4.988E-04
C_2	-1.424E-03	2.930E-06	4.146E-06	3.348E-08	1.031E-06	4.341E-07
C_3	1.944E-05	-8.198E-07	1.319E-07	-2.060E-08	-1.593E-07	-8.114E-08
C_4	-2.243E-06	-2.728E-06	-9.304E-07	5.411E-08	-3.883E-07	7.521E-07
C_5	1.706E-03	1.411E-04	-2.017E-05	4.615E-07	-8.005E-04	-9.882E-06
C_6	-5.614E-05	8.882E-06	-3.829E-04	-1.744E-06	4.279E-06	-3.433E-04

The Meso 1 model consisted of 873,899 linear tetrahedral elements and the full analysis took roughly 167 hours to complete. The results of the analysis show that, while a fully homogenized model would crack at the corner (surface highlighted in Figure 8.25), the presence of fibers has changed the crack location.

Strain energy density values were determined at 12 grid points around the CVE as shown in Figure 8.26. From these grid points, the Ordinary Kriging method outlined in Section 8.5 was used to determine the smoothed and interpolated constitutive properties of 16 cubic Sub-CVEs. The resulting interpolated properties are shown in Figure 8.27. The results shown indicate a wide array of constitutive properties depending on the proximity to reinforcing fibers and the associated orientations. For comparison with experimental data, three curves were chosen to show the highest, lowest, and average constitutive properties for the homogenized models and is shown in Figure 8.28. As shown, the general behavioral trends of the homogenized material properties align very well with the experiment values. The high model aligns the best in the latter part of the model, but overestimates the peak strength of the composite, while the low model is very close to the peak strength, but underestimates the softening behavior. The average model has fairly good agreement with the experiment in an average sense. It is to be expected that the peak values of each should not align perfectly given that no two experiments will yield the same result due to the randomness of the reinforcement.

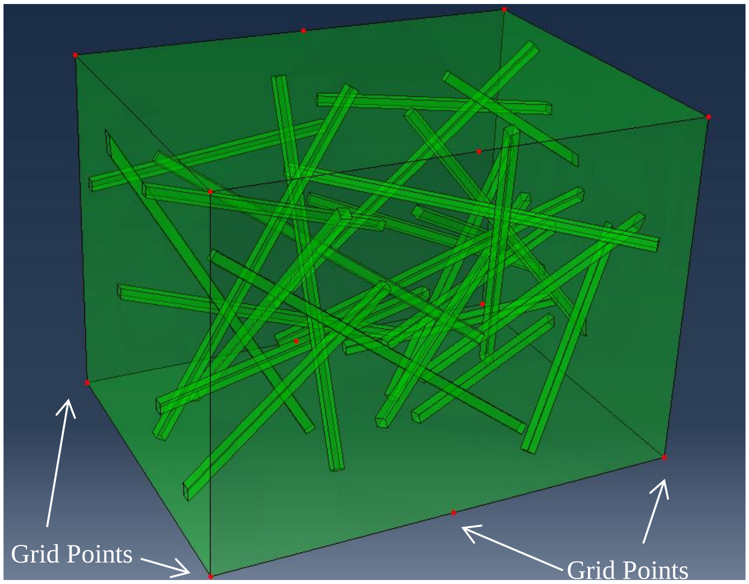

Figure 8.26 CVE 1 with grid points shown for extraction of strain energy density data

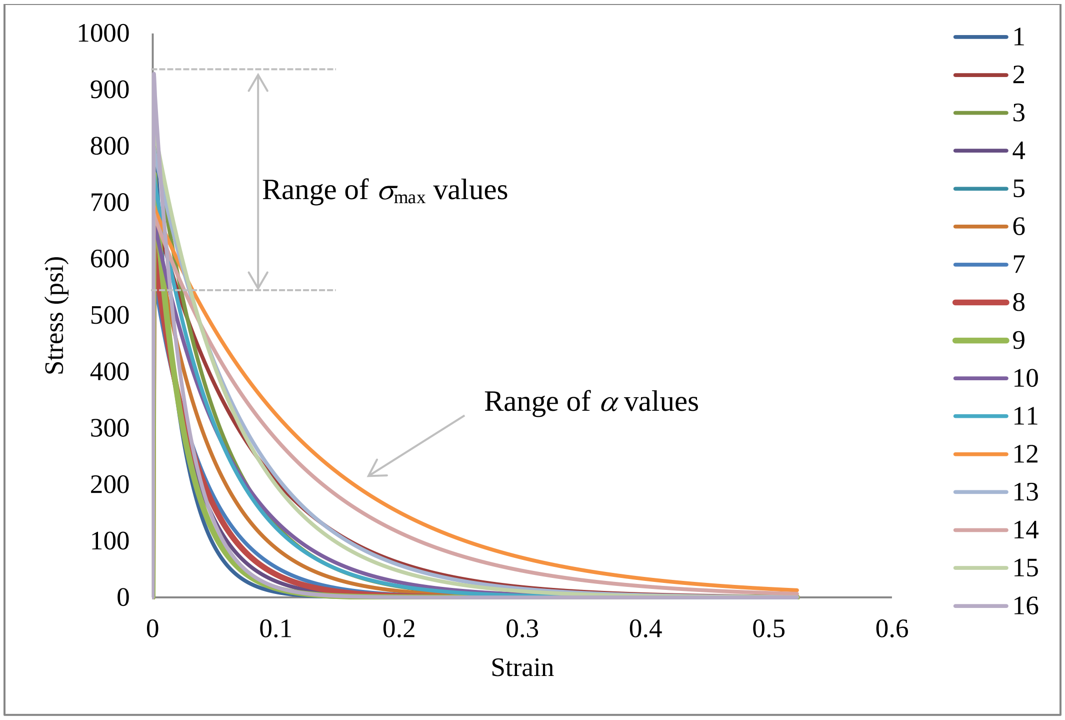

Figure 8.27 Constitutive properties for the 16 Sub-CVEs

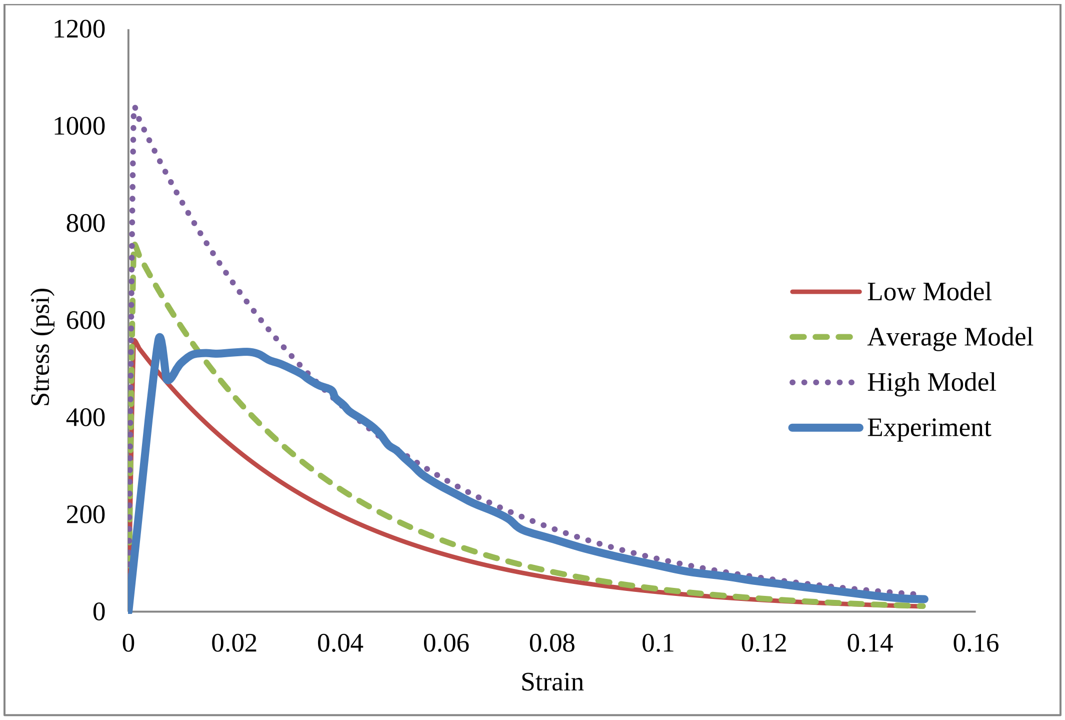

Figure 8.28 Constitutive properties for DT experiment compared to high and low range models and average homogenized model

8.5 Ordinary Kriging Homogenization

A point of interest for this study is the local variation of geometric and material properties caused by the heterogeneity of reinforcing fibers. As shown by the one-dimensional example results in Section 8.4, local errors can be caused by abrupt changes in the material properties. In order to reduce these errors, a smoothing technique is necessary to ensure some level of material continuity at the macroscale. The essential tool for most geostatistical data analysis is the variogram, used to examine the spatial continuity of the data [53]. The mathematical definition of variogram, $2\gamma(h)$, is given by

$$\gamma(h) = \tfrac{1}{2} E\left[\left\{u(x+\Delta x, y+\Delta y) - u(x, y)\right\}^2\right], \tag{8.17}$$

where $\gamma(h)$ is often referred to as the semi-variogram, $u(x, y)$ is the value of the variable of interest at location (x, y), and $E[\ ]$ is the statistical expectation operator. Note that the variogram, $2\gamma(h)$, is a function of the separation between points, h ($= \sqrt{\Delta x^2 + \Delta y^2}$), not a function of the specific location (x, y). The semi-variogram can also be expressed as

$$\gamma(h) = \frac{1}{2n} \sum_{i=1}^{n} \left[u(x_i + \Delta x, y_i + \Delta y) - u(x_i, y_i)\right]^2 , \tag{8.18}$$

where n is equal to the number of pairs of values for which the separation distance is equal to h. It is obvious that for $h = 0$, the value of the variogram is strictly equal to zero [41]. On the other hand, as h increases, the $\gamma(h)$ also increases up to a point beyond which it reaches a plateau. This value of separation distance at which the plateau is reached is called the range, a. In this study, with material and geometric anisotropy, variations may be noticed beyond this distance [10].

Ordinary Kriging (OK) is very convenient as a prediction technique due to its simplicity and reliability. This technique allows prediction of an unsampled location based on neighboring data values [30]:

$$u^*(x_0, y_0) = \sum_{i=1}^{n} \lambda_i u(x_i, y_i), \tag{8.19}$$

where λ_i are the weights assigned to the available data and neighbor data $u(x_i, y_i)$ in the proximity of the unsampled location (x_0, y_0). In OK the weights add up to unity to ensure that the estimate is unbiased:

$$\sum_{i=1}^{n} \lambda_i = 1. \tag{8.20}$$

The Kriging variance associated to an OK estimate is called the minimum variance unbiased estimator, since the constraint condition defined in Eq. (8.19) should be applied to minimize the variance of prediction errors. This can be represented as Eq. (8.20).

$$\textit{Minimize:} \;\; \sigma_{OK}^2 = \sigma^2 - 2\sum_{i=1}^{n} \lambda_i \sigma_{oi}^2 + \sum_{i=1}^{n}\sum_{j=1}^{n} \lambda_i \lambda_j \sigma_{ij}^2 \,, \tag{8.21}$$

$$\textit{with a constraint} \quad 1 - \sum_{i=1}^{n} \lambda_i = 0 \,,$$

where $\sigma_{ij}^2 = Cov(u_i, u_j)$. Using Lagrange multiplier, Eq. (8.20) may be expressed as

$$L(\lambda_1, \lambda_2, \ldots, \lambda_n; \mu) = \sigma^2 - 2\sum_{i=1}^{n} \lambda_i \sigma_{oi}^2 + \sum_{i=1}^{n}\sum_{j=1}^{n} \lambda_i \lambda_j \sigma_{ij}^2 + 2\mu\left[1 - \sum_{i=1}^{n} \lambda_i\right], \tag{8.22}$$

where *L*( ) is the Lagrange objective function, and μ is the Lagrange multiplier. Minimization of the objective function can be carried out by finding the partial derivatives with respect to λ_i and μ such that:

$$\frac{\partial L}{\partial \lambda_i} = -2\sigma_{oi}^2 + 2\sum_{i=1}^{n} \lambda_i \sigma_{il}^2 - 2\mu = 0, \quad l = 1,2,\ldots,n \quad , \tag{8.23a}$$

$$\frac{\partial L}{\partial \mu} = 2\left[1 - \sum_{i=1}^{n} \lambda_i\right] = 0 \quad . \tag{8.23b}$$

Eqs. (8.22a) and (8.22b) can be rearranged as Eq. (8.23), yielding the final form of the matrix equation in Eq. (8.24), based on OK estimates. The weight factors are determined by solving the linear matrix form in Eq. (8.24) where σ_{ol}^2 represents the estimation variance between the expected value $u(x_0, y_0)$ at the unsampled location (x_0, y_0) and known values $u(x_i)$ at the sampled location (x_i, y_i) [53].

$$\sum_{i=1}^{n} \lambda_i \sigma_{il}^2 - \mu = \sigma_{ol}^2, \quad l = 1,2,\ldots,n$$

$$\sum_{i=1}^{n} \lambda_i = 1 \quad . \tag{8.24}$$

$$\begin{Bmatrix} \sigma_{o1}^2 \\ \sigma_{o2}^2 \\ \ldots \\ \sigma_{on}^2 \\ 1 \end{Bmatrix} = \begin{bmatrix} \sigma_{11}^2 & \sigma_{12}^2 & \ldots & \sigma_{1n}^2 & -1 \\ \sigma_{21}^2 & \sigma_{22}^2 & \ldots & \sigma_{2n}^2 & -1 \\ \ldots & \ldots & \ldots & \ldots & \ldots \\ \sigma_{n1}^2 & \sigma_{n2}^2 & \ldots & \sigma_{nn}^2 & -1 \\ 1 & 1 & \ldots & 1 & 0 \end{bmatrix} \begin{Bmatrix} \lambda_1 \\ \lambda_2 \\ \ldots \\ \lambda_n \\ \mu \end{Bmatrix} . \tag{8.25}$$

A program was written in MATLAB to perform OK interpolation of the strain energy curves at observed locations in the mesoscale CVEs. These interpolated curves were the basis of the homogenization process to bridge the mesoscale and macroscale models in Section 8.4.

8.6 Multi-Scale Treatment of Fiber-Reinforced Panel under Blast

The next and final portion of this study is to apply the multi-scale approach outlined and demonstrated in Section 8.4 to a fiber-reinforced armor panel under blast load. It has been found through experiments that reinforcing fibers do not play any substantial role in local impact resistance of brittle armors. The damage in that scenario is too localized. However, it has been found that in the case of a uniform blast pressure, the damage is global and reinforcing fibers assist in absorbing significant amounts of blast energy through deformation, yielding, and debonding. The amount of fragmentation caused along large fracture lines is also mitigated, thereby protecting warfighters from fragments that can become projectiles themselves.

There are several crucial differences between the three-dimensional example in Section 8.4 and this proposed task. First is the issue of material modeling. The improved material model outlined in Chapter 4 and implemented in Chapter 7 can handle blast loading quite easily, and does not require the use of SPH due to the lack of fragmenting. The second critical difference is the issue of loading rate. The examples outlined in Section 8.4 are static models simulating a quasi-static test. To handle this, experiments have been undertaken at ERDC [16] to determine the rate effects of the fiber-matrix bond. It was determined that the bond resistance experienced little change with a loading rate up to 10,000 in/min (the fastest loading rate possible with available equipment).

The blast problem considered is applied to an arch panel made of reinforced Ashcrete and the homogenized material properties used are shown as the average in Figure 8.28. The actual test panel used in the experiment used a fiber-reinforced polymer (FRP) casing and foam support blocks that are used to cast the arch panel, but do not provide any significant structural support. Therefore, the model simulates only the arch panel. The panel was tested in a shock tube by the Blast Effects Group at BakerRisk, San Antonio, TX. The primary measurements made were of centerline deflection and reaction force at the top and bottom supports (seen as the left and right supports in the figure below). Figure 8.29 shows a schematic of the arch panel dimensions and boundary conditions. Two-way symmetry was used to reduce the computation time. The loading condition was a 10 psi (0.0689 MPa) uniform pressure load applied to the arch surface. The peak pressure occurred at 0.76 msec and lasted for 200 msec.

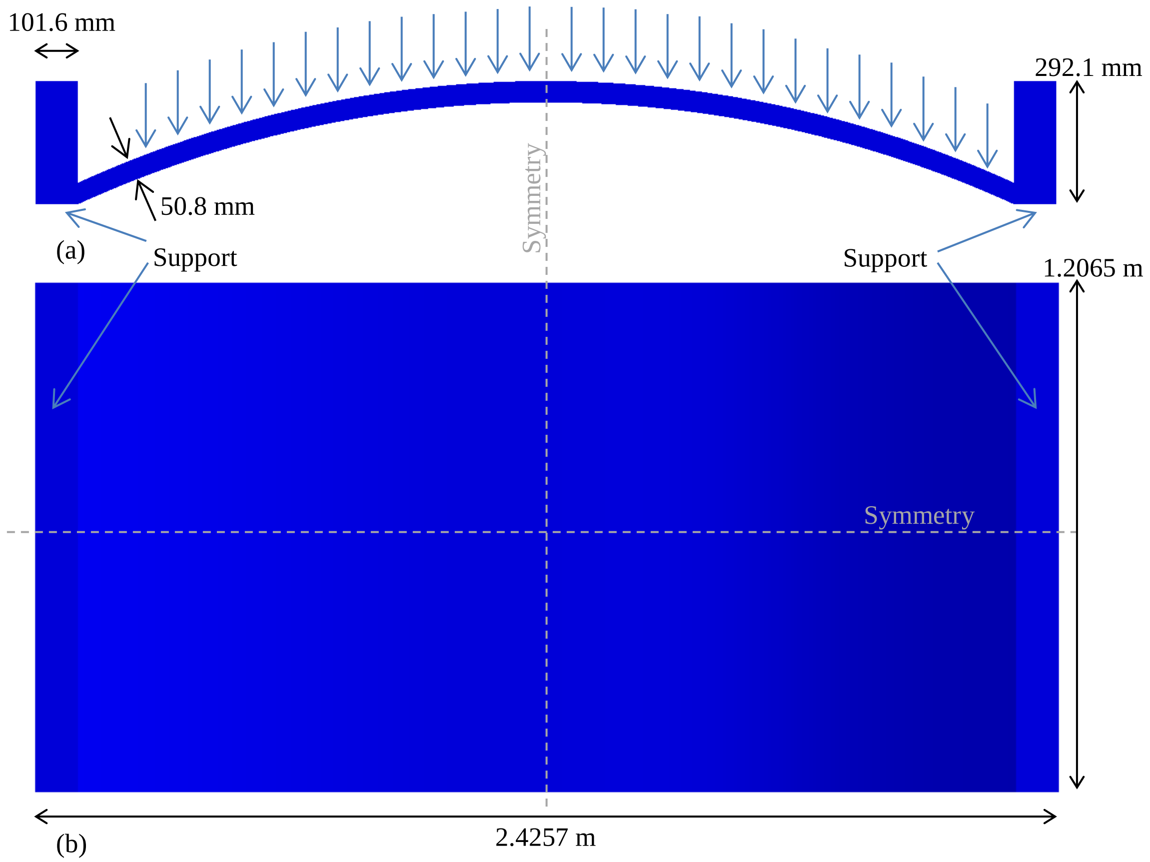

Figure 8.29 Blast arch panel schematic (a) side view (b) plan view

The results of the experiment show very clear data in terms of the reaction forces, but the centerline deflection was measured using a laser gauge which can only measure the outside of the wall (which is encased in FRP). It is for this reason that the deflections measured are expected to be significantly higher than that of the UHSC arch panel inside of it. Figure 8.30 shows two images from the high-speed video taken at the centerline of the panel on the back face. The left image shows the panel prior to the shock wave and the right image is at 13 msec (time at greatest centerline deflection). As shown, very little difference can be seen from the two frames. Model prediction of deflection for the bare Ashcrete arch was 0.94 mm; whereas the value recorded during the test was 10.65 mm, a value badly affected by many sources of error, including the deformation and vibration of low-strength encasing of the tested arch. More reliable values could not be obtained as the expensive test could not be repeated.

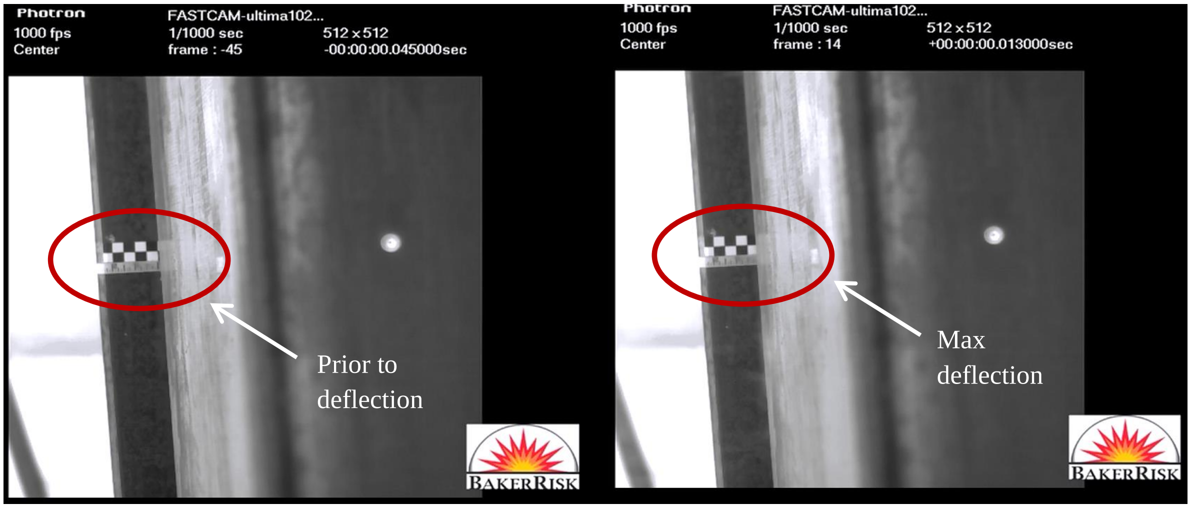

Figure 8.30 High-speed video frames from UHSC-1 arch blast panel (centerline view)

The data that is easiest to validate with high confidence is the reaction force at the supports. Figure 8.31 shows the experimental data for the reaction forces at the top and bottom supports plotted against the model. As illustrated, the model shows the secondary vibrations in the reaction force that is purely due to the reflection of the shock wave from free surfaces within the panel. Once the data is processed using locally weighted scatterplot smoothing, it sits on top of the experimental results fairly well. This would indicate however that designs based on model data would need to smooth out any reaction force data.

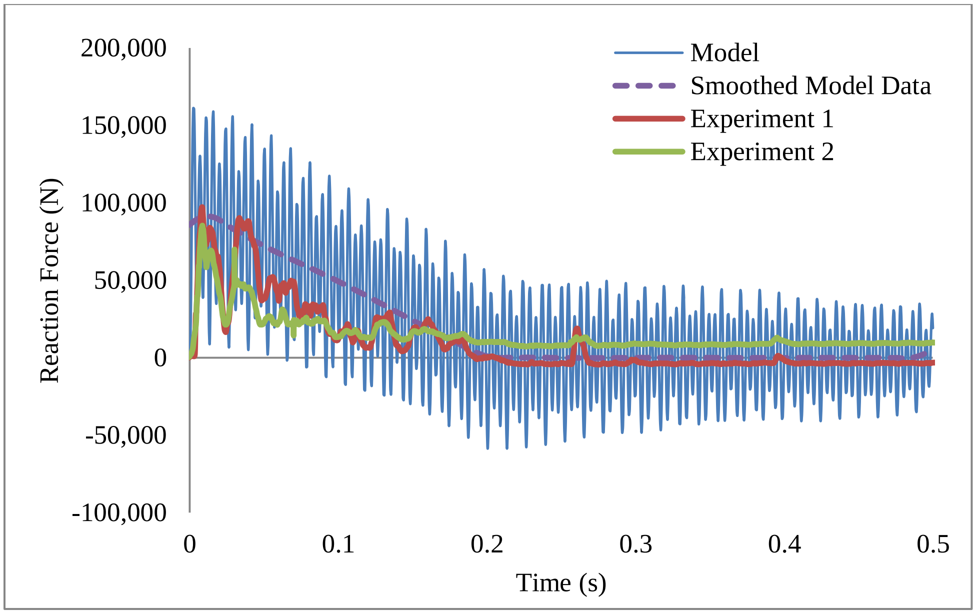

Figure 8.31 Reaction force at supports of arch panel for both experiments and model

The final use for the model would be in measures to predict damage. This given loading scenario was not high enough to fracture this arch in any locations, but the beginnings of damage can be seen in Figure 8.32. The joint where the arch meets the top and bottom blocks has begun to accumulate damage on a small scale, but larger peak pressures would rapidly increase this damage.

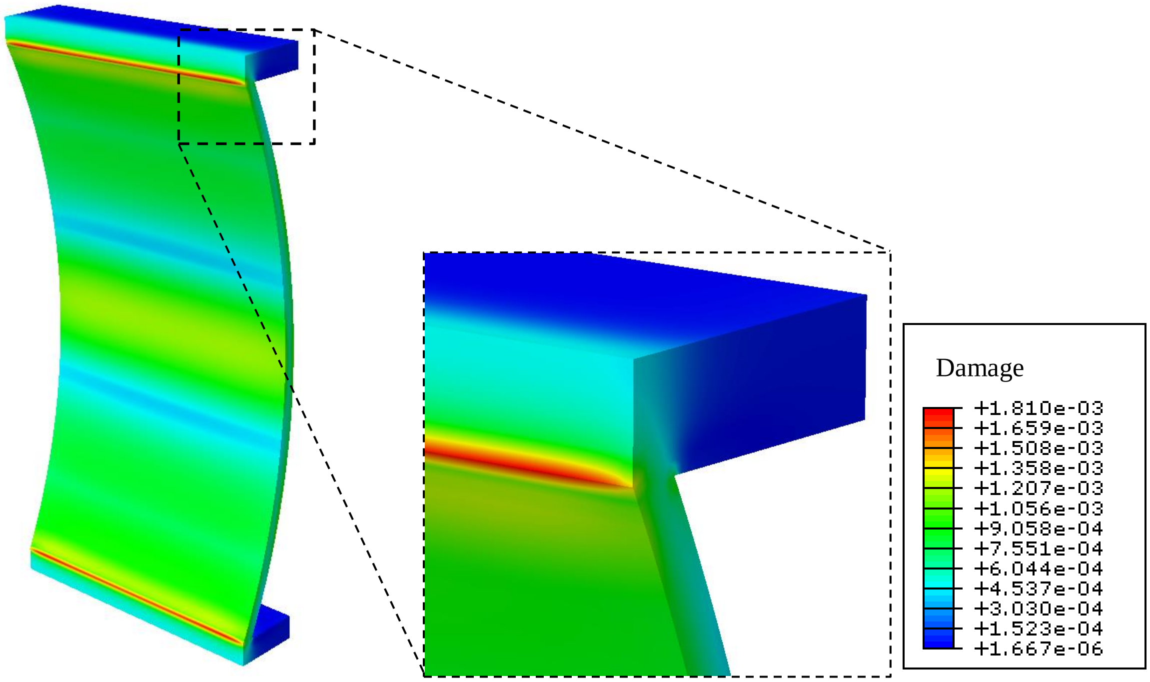

Figure 8.32 Back face of arch panel (left) and zoomed-in view of corner damage initiation (right)

Chapter 9

Summary & Conclusions

The physics of impact and blast loads on brittle structures has been described in detail as they pertain to the ongoing work by the U.S. Army to develop protective armors for war environments. For this task, numerical simulation by means of the finite element method was chosen as a suitable alternative to costly and time consuming experiments to improve the performance of such inherently brittle materials, the experiments being undertaken, primarily, to validate the simulation model. A critical review of the most prominent and widely used constitutive models for simulating concrete (and other brittle materials) to high-rate, high-pressure loads has been completed. These models were evaluated and weaknesses were identified. The underlying theme identified is that most of the existing prominent models used are dependent only on the first and second invariants of the deviatoric stress tensor and not on the third. This implies that the failure surface is symmetric in the deviatoric plane (Π-plane) and, therefore, the material is simulated to be just as strong in tension as it is in compression. This may only be a passable assumption in brittle materials when the target is sufficiently deep (tending to be semi-infinite) and tensile stresses are not induced widely. If, on the other hand, a thin panel target is impacted, the stress wave reflects off the free surfaces rapidly and creates a tensile wave that causes extensive local fracture and fragmentation before the projectile is even sufficiently deep within the target.

An improved material model has been described influenced by the initial findings of the AFC model (which laid the foundation for a non-symmetric failure surface that is third invariant dependent). A large number of material-characterizing experiments were undertaken under the auspices of the ERDC and used to successfully optimize the material parameters in the three-invariants based model for two UHSC materials: UHSC-1 and Ashcrete. Both continuum mechanics based methods (Lagrangian finite element analysis) and discrete element based models (smoothed particle hydrodynamics) have been investigated as modeling tools for simulating high-rate ballistic impact and blast.

A number of impact experiments were conducted for UHSC-1 and Ashcrete. Both FEA and SPH analyses were conducted on ballistic limit tests of UHSC-1 and fragment simulation tests of Ashcrete (for both single and stacked panel configuration). The results of these models suggest that for UHSC-1 at impact velocities near the ballistic limit of the panel, FEA models are more accurate at predicting the exit velocity of the projectile. However, the SPH models are superior in predicting fracture patterns and fragmentation. The results of the Ashcrete models suggest that at high impact velocities (>1000 m/s), SPH models are slightly better at predicting exit velocities as well as fracture patterns and fragmentation in a single thin panel case, and significantly better in a stacked panel case. In all cases, FEA models are computationally less expensive, both in data handling and time. The average increase in computation time to do an SPH model was 4.5 times that for a comparable FEA model of identical situations (and DOFs).

A study of the effects of randomly distributed and oriented reinforcing short fibers on blast resistance has also been discussed. Due to the randomness of the fibers and their large size with respect to panel depth, a multi-scale homogenization scheme needs to be used. The traditional multi-scale RVE homogenization approach was deemed inappropriate due to this lack of periodicity. An alternative CVE-based approach has been proposed with both one- and three-dimensional examples shown to validate it. The extension of this multi-scale scheme to a dynamic, three-dimensional blast problem has been validated against a blast experiment on an arch panel with satisfactory results.

Further studies are required to be undertaken in the area of multiscale modeling to extend or modify the approach presented to improve efficiency and accuracy. More extensive studies are also required to be undertaken in the area of blast response of other types of cementitious armors and their support systems. Another important area requiring attention is the combined blast and ballistic impact effects, single or multiple. Finally, the highly complex problem of prediction of the behavior of explosive-laden structures is an area of special interest.

REFERENCES

[1] Aboudi, J. (1982). A continuum theory of fiber-reinforced elastic-viscoplastic composites. *International Journal of Engineering Science*, 605-21.

[2] Adams, B. (2006). *Masters Thesis: Simulation of ballistic impacts on armored civil vehicles.* Retrieved May 4, 2012, from Scribd: http://www.scribd.com/doc/39279490/47/Rankine-Hugoniot-relation

[3] Adley, M., Frank, A., Danielson, K., Akers, S., & O'Daniel, J. (2010). *The Advanced Fundamental Concrete (AFC) Model: TR-10-X.* Vicksburg, MS: U.S. Army Engineer Research and Development Center.

[4] Babuska, I. (1975). Homogenization and its application - Mathematical and computational problems (partial differential equation solutions for diffusion and composite material analysis). *Numerical Solution of Partial Differential Equation - III* (pp. 89-116). College Park, MD: SYNSPADE, New York: Academic Press.

[5] Baker, W. (1983). *Explosions in Air.* San Antonio, TX: Winfred Baker Engineering.

[6] Belytschko, T., Krongauz, Y., Organ, D., Fleming, M. & Krysl, P. (1996). Meshless methods: an overview and recent developments. *Computer Methods in Applied Mechanics and Engineering*, Vol. 139, 3-47.

[7] Camanho, P., & Davila, C. (2002). Mixed-mode decohesion finite elements for the simulation of delamination in composite materials. *NASA/TM-2002-211737*, 1-37.

[8] Chen, W., & Han, D. (1988). *Plasticity for Structural Engineers.* New York: Springer-Verlag.

[9] Chen, W. (1982). *Plasticity in Reinforced Concrete.* McGraw-Hill Book Company.

[10] Chen, Y., & Jiao, X. (2001). Semivariogram fitting with linear programming. *Computers & Geosciences*, 71-76.

[11] Fossum, A., & Brannon, R. (2006). On a Viscoplastic Model for Rocks with Mechanism-Dependent Characteristic Times. *Acta Geotechnica*, 1:89-106.

[12] Frank, A., & Adley, M. (2007). On the Importance of a Three-Invariant Model for Simulating the Perforation of Concrete Slabs. *Proceedings of the 78th Shock and Vibration Symposium.* Philadelphia, PA.

[13] Gathers, G. R. (1994). *Selected Topics in Shock Wave Physics and Equation of State Modeling.* Livermore, CA: World Scientific Publishing Co.

[14] Gringold, R., & Monaghan, J. (1977). Smoothed particle hydrodynamics: Theory and application to non-spherical stars. *Monthly Notices Royal Astronomy Society*, 375-389.

[15] Heard, W., Basu, P., Nordendale, N., & Hoemann, J. (2011). Material Characterization of Fiber Reinforced Concrete for Improved Blast Performance. *Proceedings of the 2011 Structures Congress.* Las Vegas, NV: ASCE.

[16] Heard, W., Basu, P., Slawson, T., & Nordendale, N. (2011). Characterization and performance optimization of a cementitious composite for quasi-static and dynamic loads. *11th International Conference on the Mechanical Behavior of Materials (ICM11)* (pp. 3020-25). Lake Como, Italy: Procedia Engineering.

[17] Holmquist, T., & Johnson, G. (2005). Characterization and evaluation of silicon carbide for high-velocity impact. *Journal of Applied Physics*.

[18] Holmquist, T., Johnson, G., & Cook, W. (1993). A Computational Constitutive Model for Concrete Subjected to Large Strains, High Strain Rates, and High Pressures. *Proceedings of the 14th International Symposium on Ballistics*, (pp. 591-600). Quebec City, Canada.

[19] Huh, H., & Kang, W. (2002). Crash-Worthiness Assessment of Thin-Walled Structures with the High-Strength Steel Sheet". *International Journal of Vehicle Design*.

[20] Johnson, G. (1994). Linking of Lagrangian particle methods to standard finite element methods for high velocity impact computations. *Nuclear Engineering and Design*, 265-274.

[21] Johnson, G., & Cook, W. (1983). A Constitutive Model and Data for Metals Subjected to Large Strains, High Strain Rates and High Temperature. *Proceedings of the 7th International Symposium on Ballistics*, (pp. 541-547). The Gague, Netherlands.

[22] Johnson, G., & Cook, W. (1985). Fracture Characteristics of Three Metals Subjected to Various Strain, Strain Rates, Temperature and Pressures. *Engineering Fracture Mechanics*, 31-48.

[23] Johnson, G., & Holmquist, T. (1993). An Improved Computational Constitutive Model for Brittle Materials. *High Pressure Science and Technology*, 981-84.

[24] Johnson, G., Petersen, E., & Stryk, R. (1993). Incorporation of an SPH option in the EPIC code for a wide range of high velocity impact computations. *International Journal of Impact Engineering*, 385-394.

[25] Johnson, G., Stryk, R., & Beissel, S. (1996). SPH for high velocity impact computations. *Computational Methods in Applied Mechanics and Engineering*, 347-373.

[26] Junior, M., de Souza Neto, E., & Munoz-Rojas, P. (2011). *Advanced Computational Materials Modeling: From Classical to Multi-Scale Techniques.* John Wiley & Sons.

[27] Kwak, H., & Filippou, F. (1990). *Finite Element Analysis of Reinforced Concrete Structures Under Monotonic Loads.* Department of Civil Engineering, University of California, Berkeley.

[28] Lastiwka, M., Quinlan, N. & Basa, M. (2005). Adaptive particle distribution for Smoothed Particle Hydrodynamics. *International Journal for Numerical Methods in Fluids*, Vol. 47, 1403-1409.

[29] Li, V. (1992). Performance driven design of fiber reinforced cementitious composites. *Fibre Reinforced Cement and Concrete*, 12-30.

[30] Lloyd, C., & Atkinson, P. (2001). Assessing uncertainty in estimates with ordinary and indicator kriging. *Computers & Geosciences*, 929-37.

[31] Lucy, L. (1977). A numberical approach to the testing of fusion process. *The Astron*, 1013-1024.

[32] Mehra, V., CD, S., Mishra, V., & Chaturvedi, S. (2012). Tensile Instability and Artificial Stresses in Impact Problems in SPH. *Journal of Physics*, 1-5.

[33] Monaghan, J. (1992). Smoothed particle hydrodynamics. *Annual Review of Astronomy and Astrophysics*, Vol. 30, 543-574.

[34] Nelson, D., Heard, W., Roth, M., & Slawson, T. (2008). Development of a novel, lightweight, protective structure to resist impulsive, dynamic loads. *U.S. Army Science Conference.* Orlando, FL.

[35] Ngo, T., Mendis, P., Gupta, A., & Ramsay, J. (2007). Blast Loading and Blast Effects on Structures - An Overview. *EJSE Special Issue: Loading on Structures*, 76-91.

[36] Ngo, D. & Scordelis, A.C. (1967). Finite element analysis of reinforced concrete beams. *Journal of ACI*, Vol. 64, No. 3, 152-163.

[37] Nordendale, N., Heard, W., & Basu, P. (2011). Multi scale behavior of short-fiber reinforced cementitious material under ballistic impact. *11th International Conference on the Mechanical Behavior of Materials (ICM11)* (pp. 248-53). Lake Como, Italy: Procedia Engineering.

[38] Nordendale, N., Heard, W., Ahn, J., & Basu, P. (2012). Mixed-dimensional and Multi-scale Modeling in Computational Mechanics. *Proceedings of the 2012 Engineering Mechanics Institute Conference.* Notre Dame, TN.

[39] Nordendale, N., Heard, W., Hickman, M., Zhang, B., & Basu, P. (2013). Cementitious Material Models for Simulating Projectile Impact Effects. *Journal of Computational Materials Science*.

[40] O'Neil, E., Cummins, T., Durst, B., Kinnebrew, P., Boone, R., & Torres, R. (2004). Development of very-high-strength and high-performance concrete materials for improvedment of barriers against blast and projectile penetration. *U.S. Army Science Conference.* Orlando, FL.

[41] Pardo-Iguzquiza, E., & Dowd, P. (2001). VARIOGRAM2D: a computer program for estimating the semivariogram and its uncertainty. *Computers & Geoscience*, 549-61.

[42] Quan, X., Birnbaum, N., Cowler, M., Gerber, B., Clegg, R., & Hayhurst, C. (2003). Numerical Simulation of Structural Deformation under Shock and Impact Loads Using a Coupled Multi-Solver Approach. *5th Asia-Pacific Conference on Shock and Impact Loads on Structures.* Hunan, China.

[43] Reddy, J. (2005). *An Introduction to the Finite Element Method.* New York, NY, USA: McGraw-Hill.

[44] Schwer, L. (2007). Optional Strain-Rate Forms for the Johnson Cook Constitutive Model and the Role of the Parameter Epsilon_01. *6th European LS-DYNA Users' Conference* (pp. 1-17). Gothenburg, Sweden: ERAB.

[45] Shkolnik, I. (2008). Influence of high strain rates on stress-strain relationship, strength and elastic modulus of concrete. *Cement & Concrete Composites*, 1000-1012.

[46] Simulia. (2011). *Abaqus Example Problems Manual.* Providence, RI: Dassault Systemes.

[47] Simulia. (2012). *Abaqus Analysis User's Manual.* Providence, RI: Dassault Systemes.

[48] Sherburn, J., Heard, W., Park, H. & Chen, W. (2011). Modeling of the Split Hopkinson Pressure Bar: Application to Cortuf. *82nd Shock and Vibration Symposium*, Baltimore, MD.

[49] Tai, Y., & Tang, C. (2006). Numerical simulation: The dynamic behavior of reinforced concrete plates under normal impact. *Journal of Theoretical and Applied Fracture Mechanics*, 117-127.

[50] Vignjevic, R., Campbell, J., Jaric, J. & Powell, S. (2009). Derivation of SPH Equations in a Moving Referential Coordinate System. *Computational Methods in Applied Mechanical Engineering*. doi: 10.1016/j.cma.2009.02.027.

[51] Wang, G. (2013). Hybrid Lattice Particle Modeling of Dynamic Fragmentation of Materials. *Journal of Nanomechanics and Micromechanics*.

[52] Williams, E., Graham, S., Reed, P., & Rushing, T. (2009). *Laboratory Characterization of Cor-Tuf Concrete With and Without Steel Fibers: TR-09-22.* Vicksburg, MS: U.S. Army Engineer Research and Development Center.

[53] Woo, K., Jo, J., Basu, P., & Ahn, J. (2008). Stress intensity factory by p-adaptive mesh refinement based on ordinary kriging interpolation. *International Journal of Finite Elements in Analysis & Design*, 227-34.

[54] Yan, D., & Lin, G. (2006). Dynamic properties of concrete in direct tension. *Cement & Concrete Research*, 1371-1378.

[55] Zocher, M., Maudlin, P., Chen, S., & Flower-Maudlin, E. (2000). An Evaluation of Several Hardening Models Using Taylor Cylinder Impact Data. *European Congress on Computational Methods in Applied Sciences and Engineering* (pp. 1-20). Barcelona, Spain: Los Alamos National Laboratory.

[56] Zukas, J. (2004). *Introduction to Hydrocodes.* Elsevier.

[57] Zukas, J. A., Nicholas, T., Swift, H. F., Greszczuk, L. B., & Curran, D. R. (1982). *Impact Dynamics.* New York, NY: John Wiley & Sons.